# TRANSPORT PROPERTIES AND SURFACE KINETICS OF $Ba_{0.8+x}Gd_{0.8}La_{0.2+x}Co_2O_{6-d}$

**by**

**Rafael Alberto Prato Modestino**

Thesis for the degree of
**Master of Science**


Department of Chemistry
Faculty of Mathematics and Natural Sciences
University of Oslo

**May 2016**

# Preface

This thesis fulfils the requirements for the Master of Science degree in Chemistry at the Department of Chemistry, University of Oslo. The experimental work was conducted at the group for Solid State Electrochemistry (FASE) in the time period from August 2014 to May 2016.

I would like to thank my supervisor, professor Reidar Haugsrud, and my co-supervisors, Dr. Ragnar Strandbakke and Dr. Einar Vøllestad, who have been immensely helpful throughout the entire process. I am thankful to the whole research group for both their help and input in scientific matters, and the pleasant office environment created by all.

Most of all I would like to thank my family for their unending support.

University of Oslo, May 2016

Rafael Alberto Prato Modestino

# Summary

The main topics of this thesis are the surface kinetics and bulk diffusion of oxygen in $Ba_{1-x}Gd_{0.8}La_{0.2+x}Co_2O_{6-\delta}$ (BGLC). Previous work has identified BGLC as very promising electrode material for SOFC's and electrolyzers. With conductivities in the range of ~1000 $S/cm$ and polarization resistances in the order of $10^{-2}$ $\Omega cm^2$ around operating temperatures (i.e. 500-700 $^oC$). BGLC is in line to surpass current state of the art materials. Yet in order to introduce a new electrode, thorough characterization needs to be performed on its physicochemical properties.

BGLC has been identified as double perovkite (double on the c-axis) by x-ray diffractometry (XRD), and synchotron measurements, in the form of $AA'B_2O_{6-\delta}$. Cobalt occupies the $B$ sites at the cell's corners, with octahedral coordination of oxygen atoms, while barium and the lanthanides occupy the center of each square cell. Such a structure is highly defective; the heterovalency between barium and the lanthanides introduces oxygen vacancies in the material. The perfect structure is defined at $BaGd_{0.8}La_{0.2}Co_2O_6$ in order to establish a defect model. It is suggested that cobalt ions of differing valence (+2, +3 and +4) are evenly distributed through the material, and that the oxygen sites are ordered in layers surrounding the different cations. From this starting point, effects of temperature and atmosphere on the structure and properties of BGLC is studied.

High temperature in-situ XRD in the temperature range from 25 to 800 $^oC$ shows little change in the structure. As opposed to other perovskites (ex.: $GdBaCo_2O_{6-\delta}$), BGLC remains stable through operating temperatures. Lanthanum can be used to dope the barium sites without compromising stability, leading to more compositions. Synchotron data shows the majority of oxygen vacancies aggregated in the lanthanide layer ($O1$ site), a reduced amount in the cobalt layer ($O2$ site), and no vacancies present in the barium layer ($O3$ site). Such a flexible structure can be reduced or oxidized easily. Changes in temperature using a thermal balance revealed the oxygen non-stoichiometry as function of temperature down to [O] ~4.9. The same experiments were performed isothermally

with changing $pO_2$. The defect model proposed is able to model the data closely for BGLC and related double perovskites. These oxygen vacancies allow for ionic diffusion through the material. The transport regimes were divided in two: surface exchange of oxygen, and bulk diffusion (self-, chemical, and tracer).

Thermogravimetry (TG), isotope exchange gas phase analysis (GPA) and time-of-flight secondary ion mass spectroscopy (ToF-SIMS) were employed to measure the diffusion coefficients ($D$) and surface coefficient ($k$) of BGLC at various temperatures between 350 to 800 $^oC$. $D_{chem}$ was measured to $10^{-6}$ – $10^{-7}$ $cm^2/s$ at relatively low temperatures of 600 – 500 $^oC$ with an equally low activation energy of ~0.74 eV. This leads to an oxide ion conductivity of $10^{-2}$–$10^{-3} S/cm$ at operating conditions. The values were found to be competitive with state-of-the-art materials in literature. The pre-exponential values and activation energies are in close agreement to related double perovskites such as $GdBaCo_2O_{6-\delta}$ and $PrBaCo_2O_{6-\delta}$.

The oxygen surface exchange was studied using GPA, where a mass spectrometer tracks the concentration of species in the gas phase of a reaction chamber. Various reaction sequences are proposed for the oxygen exchange process of adsorption-dissociation-association-desorption. The desorption/adsorption steps were found to be rate limiting for this material. The surface exchange coefficient, $k$, is characterized by $6.0 * 10^{-2} Exp(-\frac{66570}{RT})$, a high value for $k^0$ and low $E_a$ for perovskites, but on par with novel double-perovskites.

An imporant of feature of BGLC is the relatively high proton content (~1 mol%) under wet atmosphere. The hydration properties are included and modeled in the defect structure. The different basicity in the oxygen sites defined (O1, O2 and O3) is used to elucidate the hydration of the material. O3, the always-filled oxygen site is considered the main site for protonation due to its basicity (relative to the other oxygen sites). The adjacent vacancies in O2, a unique feature to BGLC, then allow for hydration. TGA hydration data resulted in an extracted entropy and enthalpy of hydration of ~ -120 J/molK and -46 kJ/mol respectively for all compositions of BGLC.

Thourough agreement between the techniques used allow the characterization of the material properties, and the development of BGLC as future cathode material.

# Contents

# 1. Introduction

As we move away from fossil fuels and explore different alternatives for energy production, hydrogen technologies have come into play. Fuel cells, much like batteries, are devices that convert chemical energy into electricity. This offers an alternative to combustion engines where mechanical energy is produced, and has become a viable alternative for certain applications. The cells work by consuming a fuel through an electrochemical reaction and generates an electric current. To achieve this process, 3 main components will be discussed: a cathode, an anode, and an electrolyte. When all the parts are solid, as is the case concerned in this thesis, it is deemed a Solid Oxide Fuel Cell (SOFC). In such a cell the electrodes handle protons (anode) and oxygen ions (cathode). The electrolyte can then be designed to conduct either species. Oxide ion conductors operate at high temperatures (>700 $^{o}C$) while proton conductors are able to function at intermediate temperatures of around 600 $^{o}C$.

It is here where we arrive at the present limitation of SOFCs. The high temperatures needed to activate the ionic transport in solid state conductors to useful levels cripple the technology's potential for many applications. For practical and economic reasons, key performance parameters need to be improved in order to tip the scales in fuel cell's favor versus other industrial processes. SOFC's are some of the most energy efficient devises available, yet costs remain prohibitive. Several aspects of the cell are constantly studied and improved to break these limitations, this thesis will focus on optimizing the cathode.

A key component, the cathode is responsible for the electrochemical reduction of oxygen and formation of water, the cell's only byproduct. A material chosen for this application must (among other things) be: a good electronic conductor, be chemically compatible with the electrolyte in terms of reactivity and thermal expansion, be stable at high temperatures and vapor/$CO_2$ pressures, and ideally be a good ionic conductor. Designing such a material is not a trivial task, as some of these properties can sometimes be

mutually exclusive, so we arrive at complex structures with dopants and substitutions. Exploring these properties and studying a candidate material, BGLC, is the primary objective of this work. With faster conduction, lower operating temperatures are allowed. Thus making the optimization of these materials a fundamental step in developing competitive fuel cells.

## Objective of this thesis

The aims of this thesis are to study BGLC, refine its structure and composition, characterize its properties, and develop experimental techniques needed. The transport properties (to be defined later) of a material as promising as BGLC pose an experimental challenge at the time of measurement. Fast conduction of all species of interest, highly flexible oxygen sublattice, reactions with water and $CO_2$, etc. will come into play throughout the characterization of the material. This will push the limits of certain techniques and call for the development of others in order to obtain a clear picture of the material at hand.

Through the use of various synthesis methods and characterization techniques, we aim to place BGLC in the context of other fast mixed conductors; and cement its status as a promising candidate for SOFC cathodes.

# 2. Theoretical background

## 2.1. Cell structure

The material's structure is a central part of this study. BGLC follows a perovskite crystal structure, possesing the general form $ABO_3$. Perovskites may have different anions (ex. Halides[1]) but in the context of SOFC's, only oxides will be considered. In this arrengement, $A$ is the larger cation, occupying the center of the unit cell, $B$ is the smaller cation, on the corners, and the anion occupies the middle of the edges. Ideally, a perovskite will be a cube with close packed atoms, where the distance between oxygen atoms and the cations, $A$ and $B$, will be $a/\sqrt{2}$ and $a/2$ respectively.[2] Equation 2.1 describes this relation:

$$r_A + r_O = \sqrt{2}(r_B + r_O) \tag{2.1}$$

Yet the structure will still hold with slight deviations from ideality. As a general rule, the tolerance factor, $t$, will help predict the possibility of a material adopting the perovskite structure. When $t$ is between 0.75 and 1 (as defined by equation 2.2), the sturcture can still be expected[3].

$$t = \frac{(r_A + r_O)}{\sqrt{2}(r_B + r_O)} \tag{2.2}$$

This felxibility in the cell is key; it is the reason why perovskites can fulfill such a wide variety of applications, and show potential as electrode material's in FCs.[4] Past the cubic perovskite, compunds may stretch either axis and reduce their simmetry, commonly to orthorhombic or tetragonal unit cells. Even further distortions can be achieved by doping the metal sites (anion doping is possible, but exceeds the scope of this thesis). The

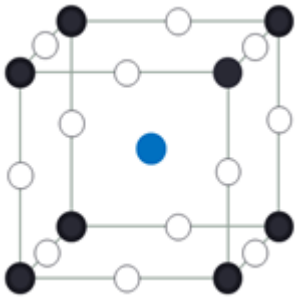

Figure 2.1.: Diagram of a cubic perovskite unit cell. Black spheres represent the $B$ cations, blue the $A$ cation and white oxygen.

general formula $(AA')_1(BB')_1O_3$ can be exploited to produce a wide range of materials with interesting properties and applications. Here the metal will have fractional stoichiometry to preserve the unit cell. It is due to this structural flexibility that perovskites are at the center of many applications, from catalysis to photovoltaics.[5]

The unit cell, cubic or not, can be doubled along the axes to produce extended formulas and structures. In our case, we start from a doubling of the c-axis to achieve a double-perovskite resulting in the genral formula $(AA')_2(BB')_2O_6$. Note the doubling in oxygen content. In this case, the metals will not have fractional occupancies of the lattice sites, but the unit cell itself is doubled to accommodate twice as many elements.[6] With the choice of four elements to make up the cell, the material's composition can be finely tuned to fit the application based on the necessary properties and structure-property relations. Ionic radius permitting, the possibilities are staggering.

There is another constraint to considered here when chosing the cations, valences. Using metals of different valencies relative to each other will place a greater strain on the structure as it is by defects, and will likely lead to oxygen non-stoichiommetry.[7] When the added valence of the cations does not total +12, if the structure is to be preserved, a number of oxygen sites must be vacant (or interstitial sites must be filled) to achieve electroneutrality in the cell. So we arrive at the final formula, $(AA')_2(BB')_2O_{6-\delta}$. Thus showing the potential oxygen vacancies in the material.

Dopants on the cation sites can also be introduced and affect the structure and its properties, such is the case for our material. Given BGLC's complex composition $(Ba_{1-x}Gd_{0.8}La_{0.2+x}Co_2O_{6-\delta})$, it is non-stoichiometric in oxygen. A completely filled cell nominally contains 6 oxygen ions, yet pressure and temperature affect the oxidation

states of the cations, and the different valences on the A sites (+2 and +3) limit the oxygen content, resulting in an oxygen deficient cell. The overall oxygen content for BGLC can be described as $O_{6-\delta}$ per unit cell.

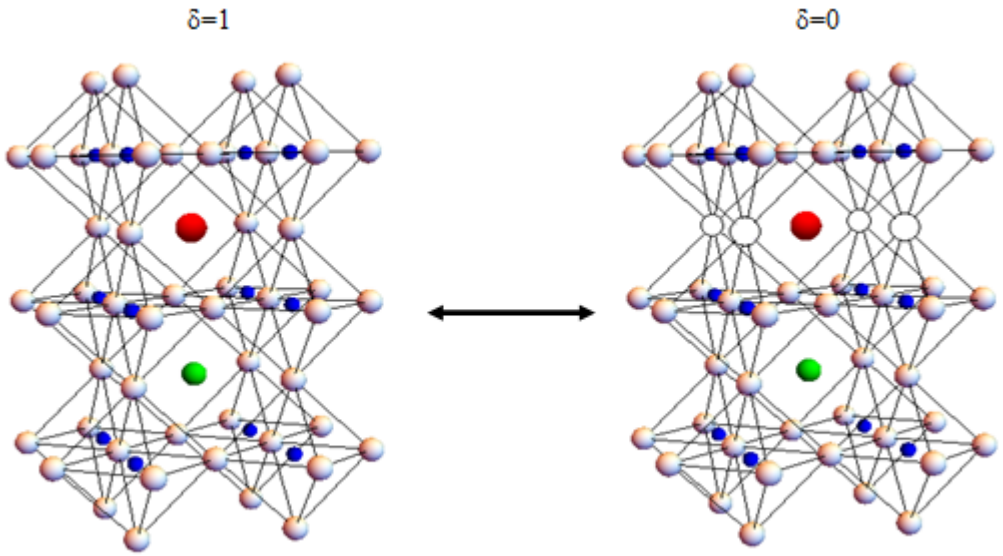


Figure 2.2.: Sketch of a possible BGLC unit cell. The blue spheres represent cobalt, white oxygen, red gadolinium and green barium (with the respective lanthanum doping). On the left is the cell with all oxygen sites filled; while on the right they are vacant around the lanthanide plane, a possible configuration of the material .

In turn, the changing oxygen content influences many of the material's properties. The lattice parameters change, possibly also giving rise to a phase transition which directly affects the transport properties. The formation of oxygen vacancies may be a key factor in the transport of protons through the material, as protons rely on the formation of $OH$ ions to migrate into the solid. Overall, this makes the quantification of oxygen content in the compound a necessity to further understand its behavior.

From this point on a notation is used to describe the many compositions of BGLC depending on the lanthanum content. This notation is described in table 2.1.

Table 2.1.: Description of composition of BGLC.

| Composition | Sample name |
|---|---|
| $BaGd_{0.8}La_{0.2}Co_2O_{6-\delta}$ | 10-8-2 |
| $Ba_{0.9}Gd_{0.8}La_{0.3}Co_2O_{6-\delta}$ | 9-8-3 |
| $Ba_{0.8}Gd_{0.8}La_{0.4}Co_2O_{6-\delta}$ | 8-8-4 |
| $Ba_{0.7}Gd_{0.8}La_{0.5}Co_2O_{6-\delta}$ | 7-8-5 |
| $Ba_{0.6}Gd_{0.8}La_{0.6}Co_2O_{6-\delta}$ | 6-8-6 |
| $Ba_{0.5}Gd_{0.8}La_{0.7}Co_2O_{6-\delta}$ | 5-8-7 |

## 2.2. Defect chemistry

The materials described in this thesis are crystalline. Crystal structures consist of 3-dimensional lattices comprised of atoms arranged in a certain manner where the smallest repeating unit is called the unit cell. The cell encapsulates the material's stoichiometry and is responsible for a lot of its intrinsic properties. Defect chemistry pertains to the deviations in real materials from this ideality. Such deviations occur in every real material at temperatures above 0 $K$. Studying how defects are created and travel through the material is key to understanding its transport properties. Defects, as we will see, can be classified according to their dimensions.

### 2.2.1. Point defects and the Kröger-Vink notation

When the defect in question refers to a single lattice site, it is 0-dimensional. This is commonly referred as, a point defect. In order to properly describe defects and their effects, we use the standard Kröger-Vink (K-V) notation for point defects.

Point defects can be vacancies, interstitial, or substitutional atoms. The complexity of the perovskite structure, coupled with the differences in size and valence of the cations, gives BGLC a highly flexible structure, potentially full of defects. An impurity in the structure either occupies an interstitial site, or substitutes another element. At the same time, vacancies occur where any one element can be absent from the lattice. Point defects, in any form, must conserve electroneutrality. Charge can be balanced by other atoms, or by electrons and holes affecting the oxidation state of the lattice. A complete picture of the structural and electronic defects describes the defect structure of the material.

The K-V notation serves to easily identify the species, lattice site, and effective charge of the defect. In the notation $A_s^c$, A refers to the species in question, usually an element or a vacancy ($V$). $s$ refers to the site which the species is occupying, it can be an existing site or an interstitial ($i$). Finally, $c$ is the effective charge that the species imparts on the structure. The effective charge is the valence state of the new species minus the valence state of the regularly occupied site. Electrons and holes are denoted $e^{'}$ and $h^{\cdot}$ respectively.

### 2.2.2. Extended Kröger-Vink notation

The use of the K-V notation enables the successful development of defect models that describe most defective structures. Nonetheless, some materials stretch the limits of K-V notation in its ability to describe them. Certain undoped and unsubstitued compounds are still inherently defective and cannot achieve a "perfect" lattice. Unorthodox solutions exist to model these materials by describing them as "100%" doped versions of other crystals. While mathematically correct, these solutions are less than ideal, and in some cases even present unsatisfactory results. A workaround presents itself by establishing that a structure can be inherently defective. In this scenario, point defects are part of the structure at all times, including at the reference state. From there, the defect structure is built. An unconventional consequence of this consession is the introduction of fractional effective charges.

As an example: the cubic δ-phase of $Bi_2O_3$ shows 3 oxygen atoms spread over 4 available sites; hence, the effective charge of an oxygen site becomes $\frac{3}{2}^{\prime}$ and a structural vacancy is present. The electroneutrality for this defect structure becomes[8]

$$\frac{1}{2}\left[O_{\frac{3}{4}O}^{\frac{1}{2}^{\prime}}\right] = \frac{3}{2}\left[V_{\frac{3}{4}O}^{\frac{3}{2}^{\cdot}}\right] \tag{2.3}$$

### 2.2.3. Defects in BGLC

The defect model for BGLC will be developed throughout the thesis as the structure and its properties are investigated in detail. Still, at first sight there are a number of defects in BGLC that can already be considered. Lanthanum may substitute both gadolinium and barium in the structure. This creates strain in the lattice due to size

differences, and introduces a variety of defects to conserve electroneutrality due to the different valences of Ba and La. One of the immediate consequences of this is oxygen non-stoichiometry. The amount of oxygen per unit cell varies with lanthanum doping content, as well as temperature and oxygen partial pressure. Changes in temperature and pressure affect the oxygen stoichiometry by oxidizing/reducing cobalt. The transport properties explored in this thesis are strongly impacted by these defects. As the material is to be used in PCFC's, protonic defects play a large role. Hydrogen can incorporate into the lattice as a hydroxide defect.[7] Either due to hydration or hydrogenation.[9]

$$H_2O_{(g)} + O_O^X + V_O^{\cdot\cdot} \rightleftharpoons 2OH_O^{\cdot} \tag{2.4}$$

$$H_2O_{(g)} + 2O_O^X + 2h^{\cdot} \rightleftharpoons 2OH_O^{\cdot} + \frac{1}{2}O_{2(g)} \tag{2.5}$$

Perhaps the most important defect reactions for this thesis are those relating to oxygen flux. These reactions describe the exchange of oxygen between the atmosphere and the lattice by filling up vacancies and interstitials respectively.

$$\frac{1}{2}O_{2(g)} + V_O^{\cdot\cdot} \rightleftharpoons O_O^X + 2h^{\cdot} \tag{2.6}$$

$$\frac{1}{2}O_{2(g)} \rightleftharpoons O_i^{''} + 2h^{\cdot} \tag{2.7}$$

These equations plus the structural definitions lead to an initial list of defects to consider for BGLC

The many structural defects that define BGLC allow for a flexible oxygen sublattice that opens the possibility for ionic transport through the materials. In the presence of a chemical potential gradient (i.e. different $pO_2$ across the sample) oxygen will adsorb on the surface, fill vacancies, and diffuse from site to site to quench the gradient. Or the reverse process in case of a higher oxygen content inside the sample against that of the surface. Similarly, when exposed to water vapor, an otherwise dry sample will incorprate some concentration of water in the bulk in the form of $[OH_O^{\cdot}]$.

Table 2.2.: List of some possible defects for BGLC

| Defect | |
|---|---|
| $\left[O_O^X\right]$ | Oxygen site |
| $[V_O^{\cdot\cdot}]$ | Oxygen vacancy |
| $[h^{\cdot}]$ | Electron holes |
| $[OH_O^{\cdot}]$ | Hydroxide |
| $[La_{Ba}^{\cdot}]$ | Lanthanum on barium sites |
| $\left[La_{Gd}^X\right]$ | Lanthanum on gadolinium sites |
| $\left[Ba_{Gd}^{'}\right]$ and $[Gd_{Ba}^{\cdot}]$ | Gd or Ba as dopants |

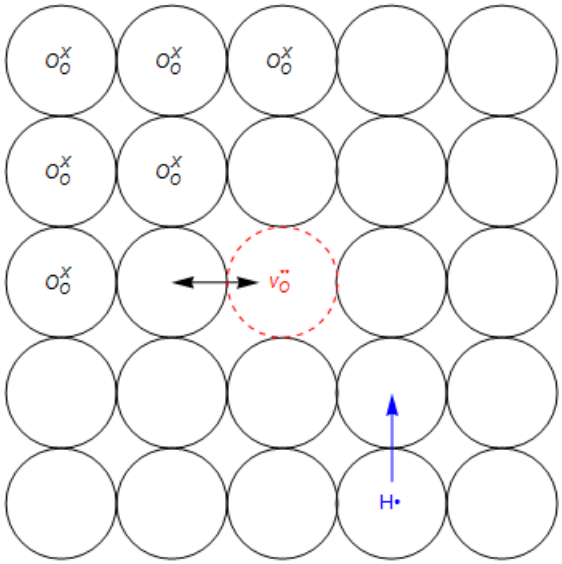


Figure 2.3.: Diagram of an oxygen sublattice showing oxygen site/vacancy hopping as well as protons hopping between adjacent oxygen sites.

Depending on the reference state chosen, some or all of these defects will have to be explored. Cobalt defects will play an important role in the material's properties as it can adopt 3 difference valence states (2+, 3+ and 4+), creating defects relative to the reference valence. Correct identification and treatment of defects will play a key role in modelling structure-property relations needed to understand, and expand on, BGLC.

### 2.2.4. Defect thermodynamics

The choice of defect structure will set a number of thermodynamic relations and will be explored later in the thesis. At this point only the protonation thermodynamics can be specified.

The equilibrium constants for the two protonation mechanisms (equations 2.4 and 2.5) are:

$$K_{hydrat} = \frac{[OH_O^{\cdot}]^2}{pH_2O\,[O_O^X]\,[V_O^{\cdot\cdot}]} \tag{2.8}$$

$$K_{hydro} = \frac{[OH_O^{\cdot}]^2\,pO_2^{1/2}}{pH_2O\,[O_O^X]^2\,[h^{\cdot}]^2} \tag{2.9}$$

Both equilibrium constants can be expressed as functions of temperatures through the entropy ($S_i$) and enthalpy ($H_i$) of either process.

$$K_i = \exp\left(\frac{\triangle S_i}{R}\right)\exp\left(-\frac{\triangle H_i}{RT}\right) \tag{2.10}$$

From the equilibrium expressions it can be infered that hydration proceeds proportionally with oxygen vacancies. On the other hand, hydrogenation depends on annihilation of electron holes. BGLC exhibits both high vacancy and holes concentration and may then experience both protonation mechanisms

## 2.3. Surface exchange

Two main transport regimes are examined here: inside the sample, and at the sample's surface. Inside, we have diffusion of the ions through the material. On the surface, the gas-to-solid exchange takes place. Gas molecules are adsorbed, dissociate and incorporate into the material. This process can be traced through the use of isotopes, or by introducing a concentration gradient and following the evolution of the diffusing species.

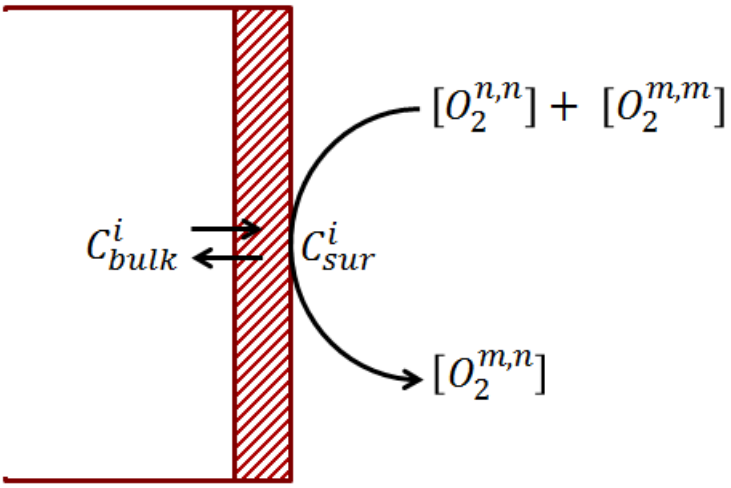


Figure 2.4.: Sketch of gas-to-surface oxygen exchange on a solid sample. The surface rates and the bulk diffusion properties will dictate the bulk, surface, and gas concentrations of different oxygen species.

### 2.3.1. Kinetic considerations

The first step of the entire process of oxygen transport through BGLC is the adsorption of the gas. Dissociative adsorption, as it is believed to be the case here, can be explored through the Langmuir isotherm for the coverage of the gaseous species. Depending on the oxygen partial pressure and the temperature, the oxygen surface coverage ($\theta_O$) can be approximated by:

$$\theta_O = \frac{(K_{O_2} pO_2)^{1/2}}{1 + (K_{O_2} pO_2)^{1/2}} \tag{2.11}$$

At the temperatures and pressures that concern this thesis it is reasonable to assume low surface coverage ($1 - \theta \approx 1$). The incorporation of oxygen into the material can be disected into 2 elementary steps:

$$O_{2,g} \rightleftharpoons O''_{2,ads} + 2h^{\cdot} \tag{2.12}$$

$$O''_{2,ads} + 2V_O^{\cdot\cdot} \rightleftharpoons 2O_O^X + 2h^{\cdot} \tag{2.13}$$

The rates for adsorption and oxidation (reactions 2.12 and 2.13) come out to:

$$r_{ads} = r^+_{ads} - r^-_{ads} = k_1 pO_2 - k_{-1}\left[O''_{2,ads}\right][h^{\cdot}]^2 \tag{2.14}$$

$$r_{ox} = r^+_{ox} - r^-_{ox} = k_1\left[O_O^X\right]^2[h^{\cdot}]^2 - k_{-1}\left[O''_{2,ads}\right][V_O^{\cdot\cdot}]^2 \tag{2.15}$$

When the system is at or near equilibrium (as is the case for some experiments in this work) the overall reaction rate is 0. With $r^+ - r^- = 0$, the equilibrium reaction rate can be taken as the square root of the product of the individual rates, a useful measure to determine certain dependencies in the measured rates.[10] Shown below:

$$R_{ads,0} = \sqrt{r^+_{ads} r^-_{ads}} = \sqrt{k_{1,ads}k_{-1,ads}\left[O''_{2,ads}\right]}pO_2^{1/2}[h^{\cdot}] \tag{2.16}$$

$$R_{ox,0} = \sqrt{r^+_{ox} r^-_{ox}} = \sqrt{k_{1,ox}k_{-1,ox}\left[O''_{2,ads}\right]}\left[O_O^X\right][h^{\cdot}][V_O^{\cdot\cdot}] \tag{2.17}$$

If oxydation proceeds much faster than adsorption, then adsorption becomes the rate determining step and oxydation can be taken to be at quasi equilibrium. In that case, $r_{ox} = 0$ and

$$\frac{r^+_{ox}}{r^-_{ox}} = K_{ox} = \frac{\left[O_O^X\right]^2[h^{\cdot}]^2}{\left[O''_{2,ads}\right][V_O^{\cdot\cdot}]^2} \tag{2.18}$$

Solving for $\left[O''_{2,ads}\right]$ and substituting into the adsorption rate equation, the overall equilibrium rate $R_0$ is given by

$$R_0 = \sqrt{r^+_{ads} r^-_{ads}} = \sqrt{\frac{k_{1,ads} k_{-1,ads}}{K_{ox}}} p O_2^{1/2} \left[h^{\cdot}\right]^2 \left[O_O^X\right] \left[V_O^{\cdot\cdot}\right]^{-1} \tag{2.19}$$

This rate constant is developed in the sections that follow.

### 2.3.2. Combinatorial analysis

Under the assumption that the two oxygen isotopes are chemically equivalent, the gas exchange process results in randomly recombined oxygen molecules. The equilibrium concentration of the three oxygen species ($O^{32}{}_2$, $O^{36}{}_2$ and $O^{34}{}_2$) depends on the composition of the feed gas and the sample. The probability of forming any of the molecules follows a combinatorial analysis.[11]

$$P^{32} = \left(\frac{n_{16}}{n_{16} + n_{18}}\right)^2 \quad P^{36} = \left(\frac{n_{18}}{n_{16} + n_{18}}\right)^2 \quad P^{34} = \frac{2 n_{16} n_{18}}{\left(n_{16} + n_{18}\right)^2} \tag{2.20}$$

$n_i$ represents the total amount of each isotope in the gas, and $P_i$ the probability of forming the gas molecules. The equilibrium concentration of any gas molecule can be obtained from the probability times the total concentration, $n$.

$$c^i_{eq} = P^i n \tag{2.21}$$

In the case where gas diffusion is significantly faster than surface exchange, the composition at the surface can be assumed to be the same as the gas. In this scenario, the rate of adsorption and desorption of gas molecules can be modelled as follows:[12]

$$r^+_i = P^i R S \frac{c^i(t)}{c^i_{eq}} \tag{2.22}$$

$$r^-_i = P^i R S \tag{2.23}$$

$$\frac{dc^i}{dt} = r_i^- - r_i^+ = \frac{RS}{n}\left(c_{eq}^i - c^i(t)\right) \tag{2.24}$$

Where $c^i(t)$ is the number of moles of any one species at time $t$, $R$ is the gas-to-surface exchange rate of the molecular species (in $molO_2/cm^2s$) and $S$ is the surface area of the sample. The integrated rate equation is shown in 2.25 with $c_0$ being the concentration of the species at $t = 0$.

$$c(t) = c_{eq} + (c_0 - c_{eq}) \exp\left(-\frac{RSt}{n}\right) \tag{2.25}$$

### 2.3.3. Homo-molecular exchange

Equation 2.25, the integrated form of the gas exchange, works under a series of assumptions. Amongst them, the rate of exchange, $R$, is a constant and the probability of forming any gas molecule, $P^i$, doesn't change with time; meaning that the total isotopic composition of the system remains the same through the reaction. These conditions refer to homo-molecular exchange. To reproduce these conditions, the oxygen inside the sample and the gas feed to the reaction chamber must contain identical amounts of $O^{16}$ and $O^{18}$. The exchange can then proceed with constant $P^i$ to preset equilibrium concentrations, and be modelled successfully following the previous analysis.

### 2.3.4. Hetero-molecular exchange

If the isotopic ratio in the gas phase changes with time, the concentration profiles do not follow the exponential bahvior described by equation 2.25. In this situation, the exchange consists of two processes: the gas exchange (adsorption-dissociation-recombination-desorption) and diffusion (chemical- or self-) inside the sample. There are two limiting conditions: If surface exchange is the much faster process, the isotopic concentration in the surface mirrors that of the gas. This means that the gas phase concentration depends on the ability of the material to diffuse oxygen. On the other hand, if diffusion is faster, the concentration at the surface mirrors the concentration in the sample's bulk. And the gas phase concentration profiles are dictated by the exchange process.

In either case, the behavior can be approximated by assuming that $R$ stays constant and that a modified version of equation 2.25 can be used. The boundary concentrations, $c_{eq}$ and $c_0$, become $c_{eq}(t)$ and $c_0(t)$ where they can be obtained from the instantaneous probability of forming a species $P^i$ and the instantaneous gas concentration. Thus, using a finite series with a fixed step-size, the hetero-molecular exchange can be modelled with:

$$c(t)^i = c^i_{eq} + \left(c^i_0 - c^i_{eq}\right) \exp\left(-\frac{RSt}{n}\right) \tag{2.26}$$

$$c^i_0 = c(t)^{i-1} \tag{2.27}$$

$$c^i_{eq} = P^{j,i} c_{total} \tag{2.28}$$

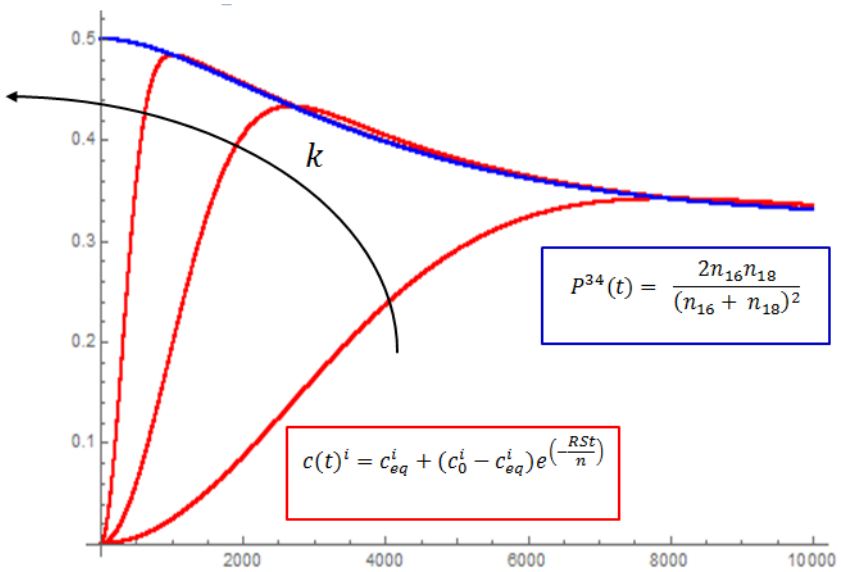


Figure 2.5.: Example $O_2^{34}$ mole fraction profile in the gas phase from heteromolecular oxygen exchange. The red line is the oxygen concentration measured by the MS, the blue line is the calculated probability of forming the mixed-oxygen species at the current time.

Figure 2.5 shows the discussed model, where the probability of forming $O_2^{32}$ reflects the isotope exchange with the bulk. The speed at which the molecule's gas phase concentration achieves instantaneous equilibrium increases with $k/D$, the ratio of surface to bulk

kinetics. This provides qualitative information about the transport in the material and the different regimes.

### 2.3.5. The surface reactions

The discussions of the previous sections in modelling and measuring the surface exchange process envelop a number of distinct mechanisms. Dissociative adsorption at the surface of the material creates 2 oxide atoms. These atoms can then recombine at the surface and desorb, or occupy vacant sites and diffuse into the bulk. The overall mechanisms can be studied through the use of different oxygen isotopes. If $^{18}O$ is introduced to a system annealed in $^{16}O$ (or any other mixture of oxygen) the evolving gases yield information about the rate of exchange of the gas-to-surface process. Proposed reactions for the isotopic exchange are outlined below.[13][14][15]

The initial case refers to a process were only atoms from the gas phase are exchanged:

$$^{18}O_{2,(g)} + ^{16}O_{2,(g)} \rightleftharpoons 2\,^{18}O^{16}O_{(g)} \tag{2.29}$$

The reaction described by equation 2.29 happens at the surface of the material once the gas molecules have undergone dissociative adsorption on vacant surface sites. For the sake of simplicity, the sites have been excluded for the equation, as they appear on both sides of the reaction.

The next case applies to one oxygen atom from the lattice exchanging with the gas phase:

$$^{18}O_{2,(g)} + ^{16}O^{X}_{O,(s)} \rightleftharpoons {}^{18}O^{16}O_{(g)} + ^{18}O^{X}_{O,(s)} \tag{2.30}$$

$$^{16}O_{2,(g)} + ^{18}O^{X}_{O,(s)} \rightleftharpoons {}^{18}O^{16}O_{(g)} + ^{16}O^{X}_{O,(s)} \tag{2.31}$$

Reactions 2.30 and 2.31 differ only on the isotope being consumed, as such, their kinetics are the same under the assumption that the 2 oxygen isotopes behave similarly at these conditions. Lastly, if both gaseous atoms are exchanged with lattice oxygen, we have:

$$^{18}O_{2,(g)} + 2^{16}O^{X}_{O,(s)} \rightleftharpoons^{16} O_{2,(g)} + 2^{18}O^{X}_{O,(s)} \tag{2.32}$$

This will be the predominant reaction if the oxydation step described in section 2.3.1 is indeed at a quasi-equilibrium and significantly faster than adsorption/desorption. If oxidation is the slower process, then reaction 2.29 will dominate. A combination of all 3 mechanisms can occur, muddling precise calculation of kinetic and equilibrium constants.

## 2.4. Diffusion

### 2.4.1. Self diffusion

To start discussing diffusion inside our material, we look at diffusivity and the random walk. Diffusivity, given by $D$, describes the ease of flux for a particle in a medium. The most basic case is defined by the random walk in the absence of a potential gradient. For the case of a crystal lattice we must note: the jump distance from site to site ($a$), the jump frequency ($\omega$), the number of available defect lattice sites ($N_d$) and a structure specific constant $\alpha$ (equal to 1 for vacancy diffusion).

$$D_r = \alpha a^2 \omega N_d \tag{2.33}$$

For protonic deffects every oxygen atom is a hopping site, in this case $N_d$ tends to 1 as all sites are available for occupancy. When refering to oxygen diffusion $N_d$ involves the formation of vacancies and becomes a temperature dependent term.

### 2.4.2. Thermodynamics of diffusivity

The formation of defects in a system is determined by the Gibbs energy of formation, and subsequently by the entropy and enthalpy.

$$N_d = \exp\left(-\frac{\triangle G_d}{RT}\right) = \exp\left(\frac{\triangle S_d}{R}\right)\exp\left(-\frac{\triangle H_d}{RT}\right) \tag{2.34}$$

The enthalpy of formation for oxygen vacancies in BGLC is positive, resulting in an increasing vacancy concentration with temperature. The other temperature dependent term in equation 2.33 is the frequency of sufficiently energetic jumps. The energy barrier relates to the strain arising from the displacement of neighboring atoms to create space for the jump. A small fraction of the vibrations (a Boltzmann distribution) posseses enough energy to overcome this barrier between jumps. Thus, the jump frequency can be described by:

$$\omega = v \exp\left(-\frac{\triangle G_m}{RT}\right) = v \exp\left(\frac{\triangle S_m}{R}\right) \exp\left(-\frac{\triangle H_m}{RT}\right) \tag{2.35}$$

$G_m$, $S_m$ and $H_m$ are the thermodynamic paramters associated with movement of the diffusing species. Amongst these parameters, most experimental measurements are focused on the enthalpies of movement and defect formation, wrapped in an activation energy. Such results are usually described with:

$$D = D_0 \exp\left(-\frac{Q}{RT}\right) \tag{2.36}$$

From equations 2.33 to 2.36 a more detailed view of the diffusion coefficient is obtained.

$$D_r = \alpha a_0^2 v \exp\left(\frac{\triangle S_d + \triangle S_m}{R}\right) \exp\left(-\frac{\triangle H_d + \triangle H_m}{RT}\right) \tag{2.37}$$

Hence $D_0$ and $Q$ are given by

$$D_0 = \alpha a_0^2 v \exp\left(\frac{\triangle S_d + \triangle S_m}{R}\right) \tag{2.38}$$

$$Q = \triangle H_d + \triangle H_m \tag{2.39}$$

Then in a typical arrhenius plot described by equation 2.7. We get an activation energy, $Q$, and a pre-exponential factor, $D_0$. Many factors may affect these equations, particularly in heavily doped materials, such deviations will be considered as necessary.

### 2.4.3. Tracer diffusion

The tracer diffusion coefficient, $D_O^*$, is the phenomenological constant obtained from isotope exchange experiments without a chemical gradient as the driving force. $^{16}O/^{18}O$ isotope exchange experiments are central to this thesis. The heavier isotope, while similar, still disrupts the entirely random nature of self-diffusion. Tracer diffusion is then realted to self-diffusion by a correlating factor $f^*$.[16]

$$D^* = D_r f^* \tag{2.40}$$

Interstitial diffusion (proton hopping) has $f^* = 1$, for vacancy mechanisms it ranges from 0.5 to 0.75.[17]

### 2.4.4. Fick's law

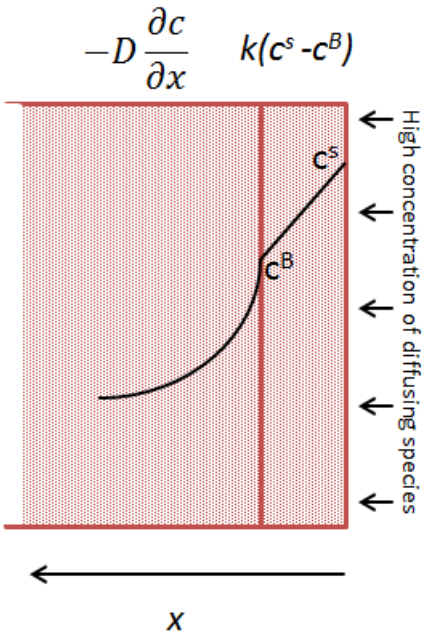


Figure 2.6.: Sketch of concentration profiles through a sample as dictated by equation 2.44 when a sample is exposed to a solution with a high concentration of the diffusing species.

Diffusion as treated in this thesis is described by Fick's laws. For steady state diffusion where there is no net flux we have:

$$J = -D\nabla c \tag{2.41}$$

Where $J$ is the flux in atoms per $s^{-1}m^{-2}$ , $D$ is the diffusion coefficient in $cm^2/s$, $c$ is the concentration of the diffusing species. When refering to 1-dimmensional diffusion, as we will from now on, equation 2.11 simplifies to:

$$J = D\left(-\frac{dc}{dx}\right) \tag{2.42}$$

With $x$ being the dimmension of the direction in which diffusion occurs. When there is no steady state and flux is time dependent, equation 2.12 is differentiated again with $\partial/\partial t$ to yield Fick's second law:

$$\frac{\partial c}{\partial t} = D\frac{\partial^2 c}{\partial x^2} \tag{2.43}$$

This equation holds true for 1-dimmensional transport, where the diffusion coefficient is constant through the bulk. Crank detailed the solutions to equation 2.43 for a host of cases.[18] If the bulk flux is proportional to the concentration gradient, and flux through the surface is proportional to the surface exchange coefficient $k$ (a mass transfer constant), then:

$$-D\frac{\partial c}{\partial x} = k(c^s - c^b) \tag{2.44}$$

The superscripts $s$ and $b$ denote the concentration at the surface and bulk respectively. Equation 2.44 is the general form of Fick's law that will be used to model the systems presented in this thesis to obtain coefficients $D$ and $k$.

## 2.5. Solutions to the diffusion equation

There is a significant mathematical background in the solutions for the diffusion equation necessary for this thesis' experiments. The full derivation of each solution can be found

in the cited literature. As such, the focus of this section will be the description of the conditions for which they can be applied, and their limits, with only a brief overview of the derivations.

### 2.5.1. Transient thermogravimetry

In the transient thermogravimetric experiments (more detail on the setup in section 4.2.6) a sintered, dense, pellet is used. The BGLC pellet is annealed at the chosen temperature and $pO_2$ to achieve the equilibrium stoichiometry. Afterwards, a step-change in $pO_2$ is applied and the mass changes of the sample are recorded. This change in $pO2$ creates a chemical potential and triggers chemical diffusion. Depending on the thickness, the surface coefficient can play a significant role in the relaxation curve obtained. With the discussed geometry and assuming a small thickness resulting in unidirectional diffusion through the pellet's faces:[18][19]

$$\frac{m(t)-m(0)}{m(\infty)-m(0)} = 1 - \sum_{n=1}^{\infty} \frac{2L_b^2 \exp\left(-\frac{b_n^2 Dt}{l^2}\right)}{b_n^2\left(b_n^2 + L_b^2 + L_b\right)} \tag{2.45}$$

Where m refers to the mass of a sample at the specified time, l is the diffusion length (the half thickness of the sample). $D$ and $k$ are the diffusion and surface coefficient respectively. The coefficients $L_b$ and $b_n$ are defined by:

$$b_n \tan b_n = L_b = \frac{lk}{D} \tag{2.46}$$

$b_n$ are only the positive roots of the transcendental equation. Equations 2.45 and 2.46 describe the general form of transient transport of these species in a sample of the specified geometry; but depending on the critical thickness of the material, the system can be simplified for limiting cases. When the sample's thickness is significantly smaller than the critical thickness ($l \ll l_c$) then $L_b$ is $\ll 1$ and equation 2.45 becomes:

$$\frac{m(t)-m(0)}{m(\infty)-m(0)} = 1 - \exp\left(-\frac{kt}{l}\right) \tag{2.47}$$

Here, surface exchange dominates the transport and D is lost. In the opposite case, for thick samples ($l \gg l_c$), $L_b$ is $\gg 1$ and bulk diffusion dominates over surface exchange and a different equation is obtained

$$\frac{m(t)-m(0)}{m(\infty)-m(0)} = 1 - \sum_{n=0}^{\infty} \frac{8}{(2n+1)^2 \pi^2} \exp\left(-\frac{(2n+1)^2 \pi^2 Dt}{4l^2}\right) \tag{2.48}$$

Equations 2.45 to 2.48 can be fitted to experimental data from mass relaxation experiments to obtain the pertinent coefficients.

### 2.5.2. Gas Phase Analysis (GPA)

The GPA experiments yielding tracer diffusion data were performed as follows. A Powdered sample of BGLC was placed in the GPA setup (see section 4.2.4) and annealed at the target temperature and $pO_2$ to attain equilibrium using pure $O_2^{32}$. After equilibrium, the gas was vacuumed out and fresh $O_2^{36}$ was flushed in to the same $pO_2$. A mass spectrometer is used to measure the changing gas concentrations. The change in isotopic composition of gaseous oxygen allows us to track the tracer diffusion inside the sample.

In this case, the powder sample can be approximated as spheres. The closed volume of the reaction chamber means that the concentration of the diffusing element ($O^{18}$) in the gas is decreasing, affecting the diffusion process. Finally, surface processes cannot be excluded so the surface equilibration rate will have to be considered. As discussed by Edwards et. al, the diffusion equation for a sphere in a solution of limited volume with finite surface equilibration can be solved to:[20][21]

$$\frac{M_t}{M_\infty} = 1 - \frac{2(1+\lambda)}{3\lambda} \sum_{a=1}^{\infty} \frac{q_a^2 \exp\left(-q_a^2 \frac{Dt}{a^2}\right)}{q_a^4 \frac{Q}{81} + q_a^2 \left(\frac{1}{9} - \frac{Q}{27} - \frac{2Q}{9\lambda}\right) + \frac{1}{\lambda} + \frac{1}{\lambda^2}} \tag{2.49}$$

Where:

$$Q = \frac{DS}{k} \tag{2.50}$$

$$N = \frac{3}{Q} - 1 \tag{2.51}$$

$$\lambda = \frac{1-f}{f} \tag{2.52}$$

$$E = \frac{1}{\lambda} - \frac{Q}{9} q_a^2 \tag{2.53}$$

$$E = \frac{1}{\lambda} + \frac{QN}{9} q_a^2 \tag{2.54}$$

and $q_a$ are the possitive roots of the transcendental equation:

$$\tan q_a = q_a \frac{E}{F} \tag{2.55}$$

$a$ is the sphere's radius. $f$ is the fractional uptake, the fraction of the total $O^{18}$ moles that are inside the sample at the equilibrium time. $S$ is the surface to volume ratio, for a sphere $S = 3/a$. $D$ and $k$ are the diffusion and surface coefficients respectively. For most calculations in this thesis no more than 20 values of $q_a$ are used. The impact on the fitting decreases with each subsequent term to negligible values at high instances of $q_a$.[22]

With this many factors, certain combination of parameters can invalidate the equation: fractional uptakes outside of 0.5 to 1, $k/D$ ratios of less than ~400 (rarely encountered for this family of materials), and particle sizes of less ~20 μm.

### 2.5.3. Time of Flight Secondary Ion Mass Spectrometry (ToF SIMS)

Samples for the SIMS experiments were prepared in the GPA setup. Dense, sintered pellets were placed in the reaction chamber and annealed to the target temperature and $pO_2$ using pure $O_2^{32}$. Once equilibrium is achieved, the gas is vacuumed and out and, very quickly, fresh $O_2^{36}$ gas is fed to the same $pO_2$. The sample is left to exchange for

very short times (< 10 min) and quenched to room temperature. The pellets are then taken to the ToF SIMS to measure the $O^{18}$ concentration profile inside the material.

Crank's solution for diffusion in a semi-infinite medium can be applied in this case:[18][23]

$$\frac{C(x,t) - C_{bg}}{C_g - C_{bg}} = erfc\left(\frac{x}{2\sqrt{Dt}}\right) - \exp\left(\frac{kx}{D} + \frac{k^2 t}{D}\right) erfc\left(\frac{x}{2\sqrt{Dt}} + k\sqrt{\frac{t}{D}}\right) \tag{2.56}$$

where $C(x,t)$ is the $O^{18}$ isotope fraction in the sample for the annealing time $t$. $C_{bg}$ is the $O^{18}$ isotopic background level and $C_g$ is the $O^{18}$ content of the gas used. $x$ is the diffusing depth.

# 3. Literature review

When discussing the structure, defect model, transport properties, and surface kinetics of BGLC, it is best to do so against the backdrop of similar materials found in literature. Significant work has been done in studying and characterizing other (double) perovskites and analog materials for SOFC's or oxygen separation membranes. In this section, we will go through the significant principles in each area as well as a collection of state-of-the-art results.

## 3.1. Solid Oxide Fuel Cells: Cathode materials

The performance of a SOFC relies on the characteristics of all the components, from anode to cathode; yet the scope of this thesis is limited to the material as the cathode, and its impact on the cell as a whole. With careful design of the composition, conductivity, ionic or electronic, stability, and surface transport can be improved. As mentioned in previous sections, the cathode is responsible for the reduction of oxygen, transport of electrons and oxygen, or protons, and must be structurally compatible with the electrolyte and interconnect. Such a wide range of characteristics requires specialized materials.

In order to diminish the necessity for a triple phase boundary (between the gas, the electrode, and the electrolyte) in which the electrochemical reactions can occur, materials with good mixed conduction (oxide ions and electrons) are chosen. Complex structures such as $GdBaCo_2O_{6-\delta}$ (GBCO) or $La_{1-x}Sr_xCo_{1-y}Fe_yO_{3-d}$ (LSCF) have been used for their high ionic conductivity, due to defects, on top of their electronic conductivity. Such a setup allows for different reaction paths, shown in figure 3.1 are 3 examples for oxygen reduction mechanism with a mixed conductor as the cathode. In reality, the process can occur simultaneously through all these pathways. Thus, high ionic conductivity can aid speed up the electrochemical processes in SOFC's.

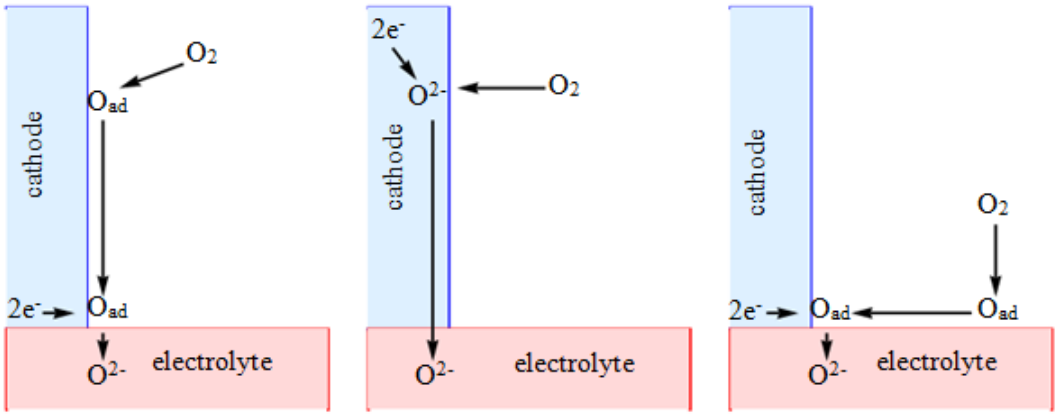


Figure 3.1.: Illustrated oxygen reduction mechanisms extending past the Triple-Phase-Boundary (TPB). Left: Oxygen is adsorbed on the cathode and undergoes reduction at the TPB. Center: Oxygen is reduced into the cathode and diffuses through the cathode and into the electrolyte. Right: Oxygen is adsorbed on the electrolyte and undergoes reduction at the TPB.

High temperatures needed for SOFCs (>600 ºC) and PCFCs (>400 ºC) are part of the current limitations in their applicability, the reason for such temperatures is the high activation energy and slow kinetics of the transport processes through solid materials. This makes the need for better materials even more apparent. As such, meticulous design of the cell's components takes the forefront in solid fuel cells research.

Perovskites ($ABO_3$) have been used extensively to fulfil these functions. For these applications, B-site cations are commonly multivalent transition metals that allow for a flexible oxygen lattice, catalyctic activity, and electronic conduction. A-site cations are then alkali earth and rare earth metals with the right site ratios (within the Goldschmidt tolerance factor), necessary basicity, and a valence, or mix of valences, that introduce vacancies to the oxygen sublattice. On this last point, double perovskites with the form $AA'BO_3$ are introduced. A mix of lanthanides (3+) and alkali earth (2+) on the 2 A-sites creates the partially vacant oxygen sublattice necessary for fast ionic conduction. This compounds the effect of the B-site cations redox capabilities to increase defect concentrations. Doping of the sites creates a material capable of many chemical reactions; but stability must also be considered when designing the cathode, as it must withstand high temperatures and pressures.

As was previously mentioned, lanthanide-alkali earth-transition metal perovskites are chosen here to design a cathode. From this general composition, some of the common

choices are described below.

### 3.1.1. Perovskites as mixed electronic ionic conductors (MIECs)

The general formula for the MIECs considered here is: $Ln_{1-x}A_xM_{1-y}M'_yO_{3-d}$. Ln = lanthanide, A = alkali earth, M and M' = transition metals. This formula describes the family of materials of which BGLC is a part of. Before we arrive at our material, we look through the exisisting compositions, their performances, and try to create a road map towards better performing perovskites.

When discussing high temperature SOFCs, $La_{1-x}Sr_xMnO_{3-d}$ (LSM), $La_{1-x}Sr_xFeO_{3-d}$ (LSF) and $La_{1-x}Sr_xCoO_{3-d}$ (LSC) have been studied for years.[24][25] An initial look at these materials yields promising results. LSM exhibits high electronic conductivity on the order of 200-300 S/cm around ~900 $^oC$ but poor ionic conductivity, $10^{-7}$ S/cm at these conditions. LSF on the other hand performs better at lower temperatures ($\sigma_e \sim$ 350 S/cm around 550 $^oC$) but its conductivity decays at high temperatures. It also shows increased oxygen transport, placing it as one of the materials of choice for SOFCs. With cobalt as the B-cation, LSC conducts up to 1600 S/cm at high temperatures, yet it has a high thermal expansion coefficient, mismatching that of common electrolyte materials (zirconium and cerium based oxides). The high performance sacrifices compatibility, thus lowering its potential for SOFC applications.[26][25][27]

From these 'base' compositions, B-site doping can be used to lossen the original restrictions. Partial substitution of cobalt ions by iron, forming LSCF is a way around the thermal expansion mismatch. It also brings the electronic conductivity down by an order of magnitude when compared to LSC, but increases the oxide ion conductivity to ~$10^{-1}$ S/cm. When barium replaces lanthanum as an A-site cation, forming BSCF, conductivity suffers. Many more compositions have been studied. Table 1, adapted from Jiang et. al. shows some literature values for common compositions.[24]

There is significant disagreement in reported values for the same materials across different labs. The large variety of factors influencing these properties makes it hard to create a set of structure-property relations leading to precise design of cathode materials. Because of this, and the array of metals available as dopants for the perovskite structure, it is difficult to predict properties outside well studied families of compositions. There is a drastic gap in knowledge from thoroughly studied materials such as LSM to more

| Composition | Thermal expansion coefficient ($x10^{-6}K^{-1}$) | Conductivity $\sigma(S/cm)$ | References |
|---|---|---|---|
| $LaMnO_3$ | 12.5 | 83 (800 ºC) | [28] |
| $La_{0.6}Sr_{0.4}MnO_3$ | 12.7 | 320 (800 ºC) | [28] |
| $Pr_{0.5}Sr_{0.5}MnO_3$ | 12.9 | 250 (700 ºC) | [29] |
| $Nd_{0.7}Sr_{0.3}MnO_3$ | 10.3 | 269 (800 ºC) | [30] |
| $Gd_{0.5}Sr_{0.5}MnO_3$ | 6.84 | 229 (800 ºC) | [31] |
| $Gd_{0.8}Sr_{0.2}Co_{0.9}Mn_{0.1}O_3$ | 24 | 271 (800 ºC) | [32] |
| $La_{0.84}Sr_{0.16}Co_{0.2}Mn_{0.8}O_3$ | 11.69 | 47 (800 ºC) | [33] |

Table 3.1.: Compilation of properties for commonly studied pervoskites for cathode materials adapted from literature.[24]

complex composition such as BSCF. Hence in this study of BGLC, we focus on the properties of the isolated material, as it is he first step before further operation tests. Yet there is reasonable agreement in magnitudes and trends as seen in table 1. Most commonly, promising materials exhibit conductivity values on the order of up to a few hundred S/cm. Ionic conductivity in MIECs hovers around $10^{-2}$ S/cm.

## 3.2. Layered perovskites for fast ionic transport

The use of MIECs such as those shown in the previous sections opens up the active region past the TPB to a certain electrode thickness. To continue improving the characteristic active depth, the oxygen surface exchange and diffusion must be optimized. To this end more complex structures are introduced. Certain combinations of 2 A-site cations may lead to an ordered cell where the 2 metals alternate layers. If the difference in size between the host and the dopant is large enough, materials will preferentially show a degree of order in the cell. See figure 3.2.

Following the same general formula as before, a small lanthanide and a large alkali-earth metal are used. Barium stands as the primary choice for the alkali-earth metal given it's the largest of its group (excluding Radium for its radioactivity). Manganates, cobaltates and ferrates have been synthesized as layered perovskites. An added benefit of the tiered structure is the possibility for vacancy ordering. Vacancies can gather around the lanthanide plane, creating channels with unidirectional diffusion. The high oxygen

diffusion coefficient seen in these materials is explained through this phenomenon. The heterovalency of the dopant (with respect to the lanthanide) creates an oxygen deficient cell, while the vacancy accumulation creates channels for fast diffusion.

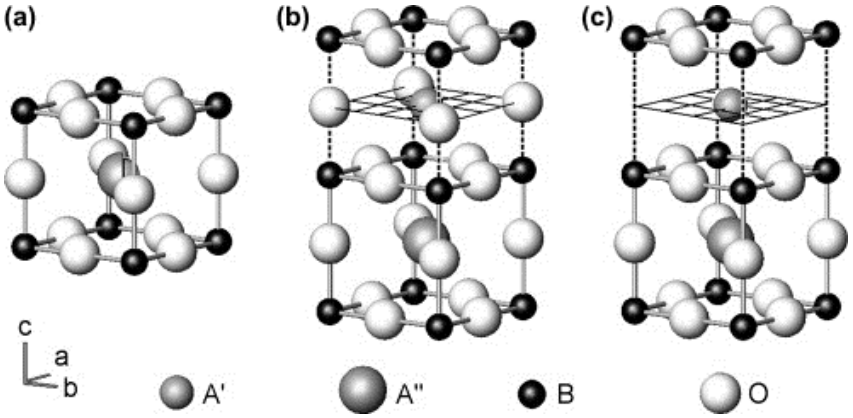


Figure 3.2.: Ordering of lanthanide $A\prime^{3+}$ and alkali-earth $A''^{2+}$ ions in the A-site sublattice of half-doped perovskites. (a) A simple cubic perovskite $A\prime_{0.5}A''_{0.5}BO_3$ (B is transition metal) with random occupation of A-sites is transformed into (b) a layered crystal $A\prime A''B_2O_6$ by doubling the unit cell, provided the difference in ionic radii of A´ and A″ ions is sufficiently large. (c) Oxygen atoms can be partially or completely removed from lanthanide planes, providing a variability of the oxygen content in $A\prime A''B_2O_{6-x}$, where 0 < x < 1.[34]

Taskin et al. investigated the chemical diffusion and surface exchange of $Gd_{0.5}Ba_{0.5}MnO_{3-x}$ and $GdBaMn_2O_{5+x}$, the disordered and ordered species respectively. The oxygen stoichiometry was significantly more flexible in the ordered version, as the oxygen vacancies were trapped by the dopant in the disordered cell. Even more drastic was the difference seen in the rate of diffusion through the 2 materials (figure 3.3).[34]

Their study of the general formula $LnBaCo_2O_{5+x}$ with a host of different lanthanides that exhibited the ordered cell led to initial conclusion of a proportionality between the diffusivity and lanthanide ionic radius. The highest diffusivity is seen in the samples with neodymium among the tried cations.

Maignan et al. investigated the structure of the ordered perovskites as reported in table 1. It can be seen that this selection of lanthanides in $LnBaCo_2O_{5+x}$ forms a cell with a doubled c-axis. For the larger cations (Pr and Nd) the material behaved as a semimetal even at low temperatures and thus, doesn't have a metal-insulator transition. The compounds with the smaller lanthanides showed this transition aroun 300 K, well

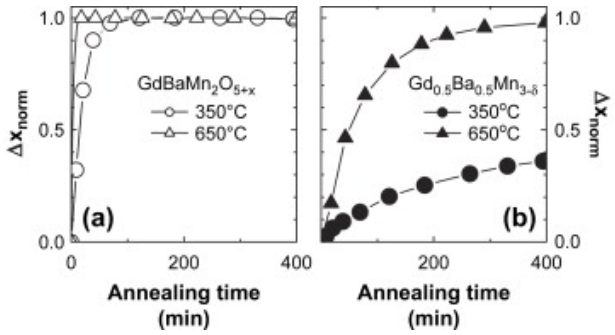


Figure 3.3.: Normalized change in the oxygen content $\Delta$xnorm = (x − x0)/(xeq − x0) (x0 is the initial oxygen content and xeq is the equilibrium one) with time during annealing in the oxygen gas flow at 350 and 650 °C in compounds with ordered (a) and disordered (b) A-site sublattice.[35]

Table 3.2.: Structural Parameters (Lattice Parameters and Volume Are Given in the Primitive Cell apxapxap to Compare the Values) and Physical Parameters from Resistivity and Susceptibility Curves for $LnBaCo_2O_{5+x}$ Phases with Ln 5 Pr, Nd, Sm, Eu, Gd, Tb, Dy, and Ho.[36]

| Parameter | Pr | Nd | Sm | Eu | Gd | Tb |
|---|---|---|---|---|---|---|
| a ($\AA$)) ($a_p$) | 3.9019(1) | 3.8969(1) | 3.8862(1) | 3.8834(1) | 3.8834(1) | 3.8667(1) |
| b ($\AA$)) ($a_p$) | 3.9061(1) | 3.9015(2) | 3.9085(1) | 3.9159(2) | 2.9106(1) | 3.9076(1) |
| c ($\AA$) ($a_p$) | 7.6306(1) | 7.6115(1) | 7.5661(1) | 7.5661(1) | 7.5338(1) | 7.5164(1) |
| V ($\AA^3$) | 116.30 | 115.72 | 114.92 | 114.67 | 114.15 | 113.57 |
| $T_{MI}(K)$ | - | - | 320 | 360 | 350 | 330 |
| $P_{400K}(\Omega cm)$ | $4 * 10^{-4}$ | $9 * 10^{-4}$ | $9 * 10^{-4}$ | $9 * 10^{-4}$ | $1 * 10^{-3}$ | $1.5 * 10^{-3}$ |

below the desired operating temperatures. The resistivities in table 1 measured at 400 K confirm the expected trend for higher conductivities with dopant size. Their results from electron diffraction and HREM point towards the oxygen vacancy ordering in the $LnO_x$ layers of the perovskite.[36]

One of the most promising of the layered perovskites at present is $PrBaCo_2O_{5+x}$.[37] In line with the size proportionality mentioned by Taskin et al., PBCO exhibits oxygen transport kinetics at least as fast as other layered pervoskites with smaller lanthanides.

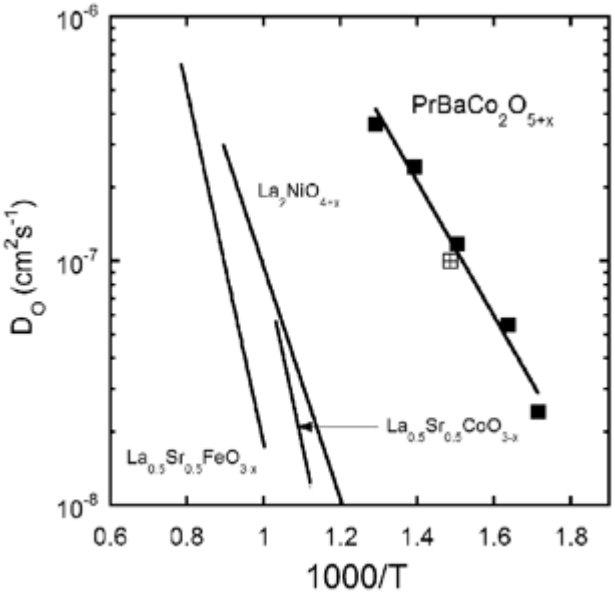


Figure 3.4.: Comparison of the values of $D_O$ measured by ECR for ceramic samples. The filled squares are the ECR measurements and the crossed square is the IEDP result. The lines correspond to data taken from the literature.21,27–32.[37]

In figure 3.4 the self-diffusion coefficient of oxygen in PBCO can be seen to be several orders of magnitude higher than other common MIECs. A lot of the recent literature is focused on optimizing the performance of this material ($LnBaCo_2O_{5+x}$), and the two most common candidates in terms of ionic conduction are PBCO and GBCO. The wide range of values reported for the same composition across different research groups makes it difficult to separate them. Activation energies range from around 1 to 0.5 eV for the tracer diffusion coefficient and between 0.9 to 0.7 eV for the surface coefficient.

Burriel et al. employed Isotope Exchange Depth Profile (IEDP) to measure the transport coefficients in PBCO and arrived at the results shown in figure 3.5. The activation energy

for both processes is slightly lower for GBCO as per the results from Tarancon et al, while the magnitudes of both coefficients is higher for PBCO after 400 ºC. Burriel argues that the high values from Kim et al. are a misrepresentation of the coefficients due to porous samples.[38]

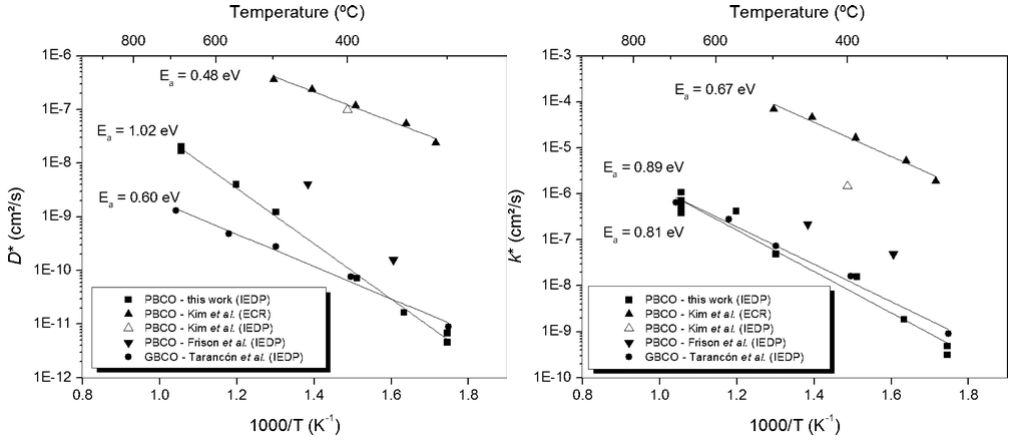


Figure 3.5.: a) Arrhenius plot of the oxygen tracer diffusion coefficients obtained for PBCO and comparison with literature data. b) Arrhenius plot of the surface exchange coefficients obtained for PBCO and comparison with literature data.[38]

## 3.3. Gadolinium Barium Cobalt Oxide (GBCO)

In its initial composition, BGLC 10-8-2, is GBCO with 20% lanthanum doping on the barium sites. For the rest of the compositions the lanthanum content increases, replacing gadolinium. So it is natural to have a detailed examination of GBCO to aid in the understanding of our material.

The crystal structure of GBCO has been described through a variety of methods. Ishizawa et al. looked at the structural evolution of the material. Two structural transitions were found. The first one is a reversible transition between a $3a_p x 3a_p x 2a_p$ cell ($\gamma$ phase) and a $1a_p x 1a_p x 2a_p$ cell ($\beta$ phase) at ~380K. Where ap is a perovskite-type unit cell parameter, thus the standard double perovskite mentioned earlier would be $1a_p x 1a_p x 2a_p$. The $\gamma$- $\beta$ transition reflects the charge order-disorder of the cobalt 2+ and 3+ ions. This collapse was shown to conserve the oxygen stoichiometry. At ~700K GBCO exhibits an irreversible structural transition, going from the $\beta$-phase to a tetragonal (p4/mmm) $1a_p x 1a_p x 2a_p$ cell ($\alpha$ phase). This time, the transition is associated with

partial detachment of oxygen, showing a large reduction of the oxygen content. Figure 5 summarizes the transition.[39]

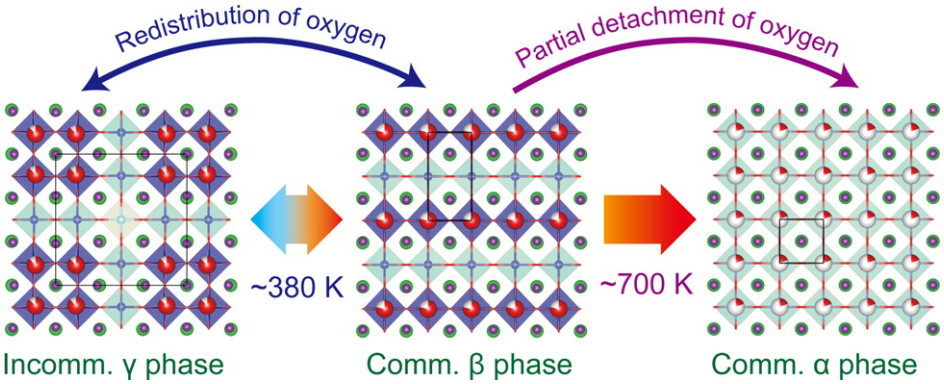


Figure 3.6.: GBCO structural transitions.[39]

The GBCO α-phase is characterized as having 3 different oxygen sites labelled O1, O2 and O3 around barium, cobalt and gadolinium respectively, as seen in figure 1. The alternating planes are seen as $[CoO_2] - [BaO] - [CoO_2] - [GdO_\delta]$... For the purposes of oxygen transport, Ishizawa et al. divide the structure in $[BaCo_2O_5]$ and $[GdO_\delta]$ layers; thus emphasizing the preferential vacancies around the lanthanide.[39]

Tarancon et al. explored the conductivity of GBCO across these transitions. Three regions of the conductivity are identified and correlated to the structural transformations, see figure 3.7. At low temperatures the conductivity increases with an activation energy of 0.8 eV, this value decreases after the first phase transition to 0.02 eV. When GBCO becomes tetragonal (1x1x2) the conductivity exhibits metallic behavior.[40]

Tsvetkov et al. studied the oxygen nonstoichiometry and developed a defect model for the material based on a cubic perovskite reference state. The model treated Barium as a dopant on $GdCoO_3$ and introduced an associated defect for vacancies around the Barium atoms, $(V_O^{\cdot\cdot} - Ba'_{Gd})^{\cdot}$. Cobalt in the ground state was adjudged to be 3+. The experiments were carried out at temperatures between 900 and 1050 $^{o}C$. In this range the formation of the associated vacancy was greatly favored, resulting in little concentration of free vacancies before GdBaCo2O5 stoichiometry is achieved.[41] These results contradict most literature on the topic and were reconsidered in a later paper.[42] The common placement of the vacancies has been shown to be on the lanthanide layer,[43] which facilitates oxygen transport,[39] and leads to the low activation energies for diffusion in these materials.

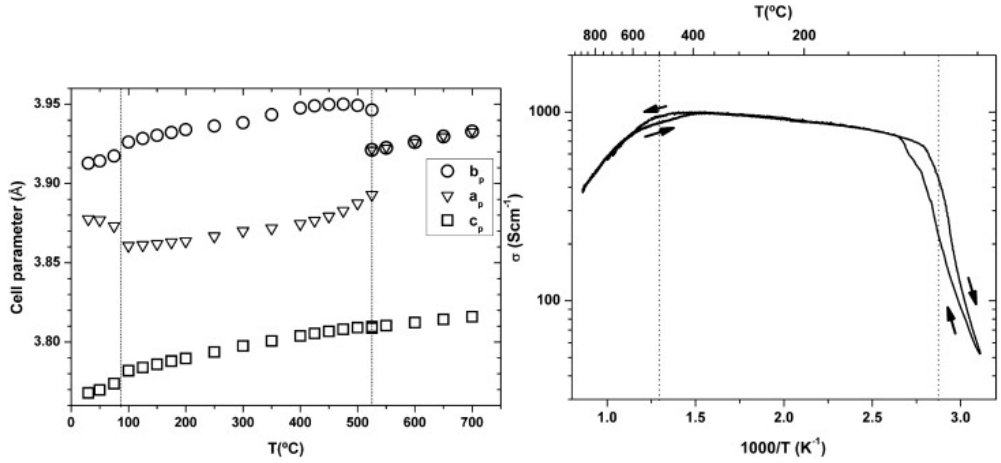


Figure 3.7.: Left: Thermal evolution of the cubic lattice parameters. Dashed lines mark the position of the low- and high- temperature structural transitions. Right: In-plane overall conductivity as a function of temperature for a four-probe set of measurements on a $GdBaCo_2O_{5+x}$ pellet in air. Arrows indicate the heating and cooling cycles. Dashed lines indicate the structural phase transition temperatures.[40]

## 3.4. BGLC so far

The only study on BGLC was published by Strandbakke et al. in 2015 and it is the foundation of this thesis. The hydration properties, stoichiometry, and performance as an electrode were tested against a host of similar materials. BGLC possessed the lowest polarization resistance in the study for the temperature range sampled (500 to 700 ºC). Achieving remarkably low resistances of 0.05 and 10 Ωcm2 from 650 to 350 ºC, see figure 3.8.[44]

Furthermore, BGLC exhibited the lowest oxygen content. At room temperature the oxygen stoichiometry was found to be ~5.55 and decreased to ~5 after 1000 ºC. It is a remarkable range when compared to the other materials, but very similar to that of GBCO. In fact, the prescence of Gd instead of Pr introduces a significant amount of vacancies. Iron doping on cobalt also reduced the amount of vacancies for both, Gd and Pr containing samples.

Figure 3.9 shows an important feature of BGLC. It was shown to be the only double perovskite of its kind to hydrate significantly at these conditions. In terms of lattice sites there are not many differences between PBCO/GBCO and the expected struc-

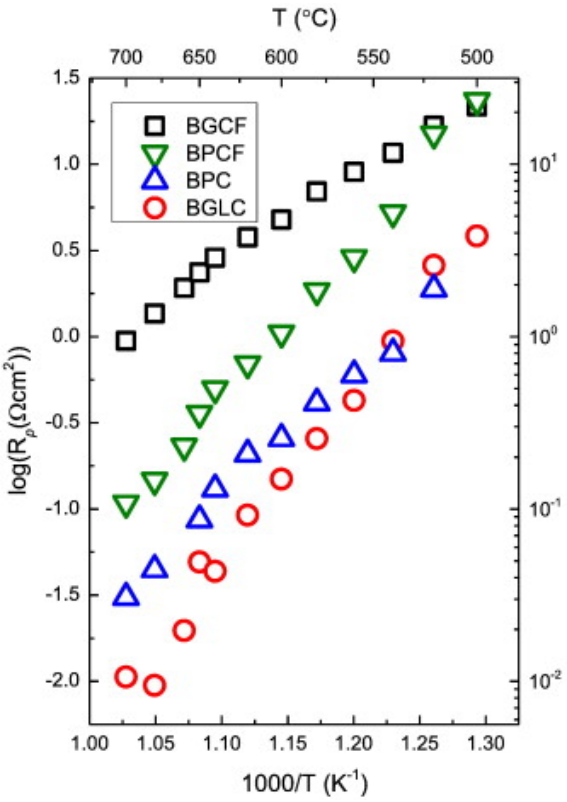


Figure 3.8.: Total apparent polarisation resistances of BGLC, BGCF, BPC, and BPCF at 500-700 °C in $pO_2 = 1$ and $pH_2O = 0.027$.[44]

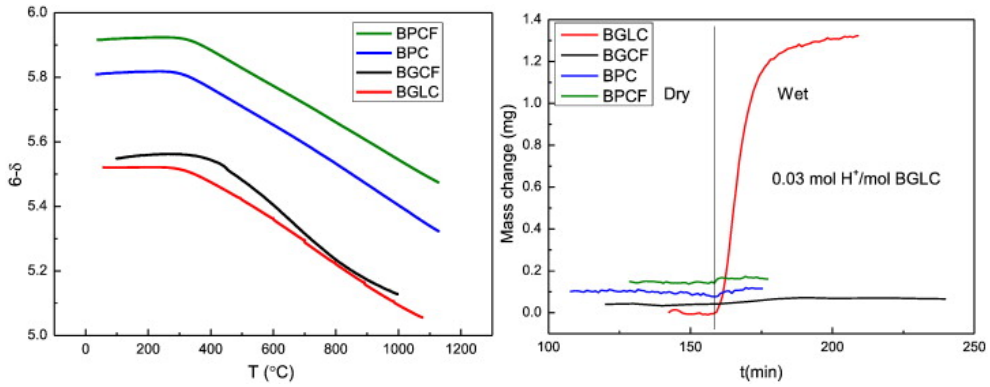


Figure 3.9.: Left: Oxygen non-stoichiometry, 6-$\delta$, vs T in $BaRE_{1-x}La_xCo_{2-y}Fe_yO_{6-\delta}$ in air. Right: Mass changes for 2.5 g of powders after isothermal switch at 400 °C from $pH_2O = 3*10^{-5}$ to $pH_2O = 0.02atm$ at $pO_2 = 4*10^{-4}atm$.[44]

ture of BGLC, yet these results point towards a significant change in their activity towards water. The standard entropy and enthalpy of hydration were calculated to be $-140\,J/(molK)$ and $-50\,kJ/mol$ respectively.

# 4. Experimental methods

The methods employed in this thesis comprise a series of tools to synthesize and thoroughly characterize desired aspects of the material. All compositions of BGLC were synthesized following a sol-gel method. The phase composition of the powders was analyzed by XRD and SEM. After confirming phase-purity, pellets were sintered at high temperature to achieve higher densities (>95%) in order to be able to successfully use ToF-SIMS in our samples. Isotope exchange GPA was used to probe the transport properties of the material and extract surface reaction parameters. Thermogravimetric analysis (transient and otherwise) served to quantify the oxygen content as a function of temperature and $pO_2$, and the oxygen chemical diffusion coefficient. ToF-SIMS allowed us to calculate the tracer diffusion coefficient, thus completing the overview of the desired materials' properties.

## 4.1. Preparation of samples

### 4.1.1. Synthesis

BGLC was synthesized using a sol-gel method with citric acid as a complexing agent. Given the complexity of the desired formula, wet-chemical methods are used to promote a uniform composition.

Oxides and salts of the metals were used in the process. $BaCO_3$, $Gd(NO_3)_3 \bullet 6H_2O$, $La(NO_3)_3 \bullet 6H_2O$ and $Co(NO_3)_2 \bullet 6H_2O$ (carbonates of the metals were also used) were dissolved in a citric acid solution, $C_6H_8O_7 \bullet H_2O$. The citric acid solution was prepared to a 1:1 molar ratio with the cations. The solution was heated to boiling and the salts were dissolved under heavy stirring. Ammonia, $NH_3$, was added in a drop-wise manner to maintain the $pH$ between 1 and 2. Rapid addition of ammonia prompts the formation of hydroxyl ligands that complex cobalt ions, forming a pink cloudy solution which must

be avoided. After complete dissolution, the heat was increased to approximately 300 ˚C to rapidly evaporate the solvent. The evaporation process takes 2-4 hours depending on the volume. Afterwards, the gel is formed. Heating was continued to decompose the gel, at which point, the mixture auto-combusts. The resulting ash was placed in a furnace at 400 ˚C for 5 hours to ensure complete combustion of the gel network. When complete combustion is achieved, the ash was transferred to an alumina crucible and placed in a furnace for the final step of the synthesis. The temperature was ramped 180 ˚C/h to a final temperature, ranging from 900 ˚C to 1100 ˚C. The temperature was kept for 24 hours and later ramped down at the same heating rate. Figure 4.1 shows a sample heating curve.

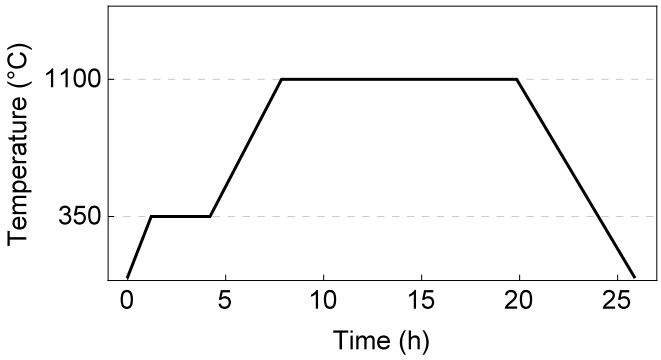


Figure 4.1.: Sample heating ramp for the BGLC synthesis after solvent evaporation.

### 4.1.2. Sintering

In order to increase the density of the materials, sintering is employed. High temperatures (below the melting point, $T_m$) are employed to sinter the grains together. The high free-energy of individual particles is removed by going from a concave to a convex geometry; thus, densifying the samples.

The as-synthesized powders were grinded in a mortar for 1 hour before milling in a planetary ball mill. 15-20 drops of a polymer binder per gram of powder are added to the sample. The powders were uni-axially pressed into pellets of different diameters, from 9 to 25mm. The hydraulic press used was a Specac GS15011 with 3 presses of 4-5 tons each. The green body pellets were sintered at 1180 ˚C for 12 hours with a heating/cooling rate of 180 ˚C/h. Previous tests showed that BGLC melts at higher temperatures, limiting the sintering process. It is important to maintain a relatively

slow cooling rate to avoid "quenching" the samples and locking a pseudo-stable phase. After sintering, shrinkage of the pellets is observed.

## 4.2. Sample characterization

### 4.2.1. X-Ray Diffraction (XRD)

In order to study the composition and phases of the samples x-ray powder diffraction was used. Difractograms were obtained for samples before and after sintering in case the green bodies showed phase-impurities. In the case of powders, small samples in the order of 20 mg were suspended in isopropanol and dripped onto the suitable sample holders. The sample is complete after repeating the process several times and allowing the isopropanol to evaporate, leaving an uniform film on the substrate. In the case of the sintered pellets, they were placed on deeper holders and kept level across the surface.

A Bruker D8 3-circle diffractometer with area detector and nitrogen cryostat was employed. The x-rays were scanned at angles ranging from 20 $^\circ$ to 80 $^\circ$, the area of interest.

For the in-situ temperature-dependent experiments, the powders were all submitted to the same heat treatment, heated to 1100 $^\circ$C at 180 $^\circ$C/h and ramped down at the same rate. This was done to ensure that the phases in the material reached equilibrium and no pseudo-stable phase was locked in at room temperature. After the pre-treatment, the powders were placed in special alumina crucibles for the XRD measurements. The instrument was then programmed to heat to 800 $^o$C in intervals of 50 or 100 $^o$C, dwelling at each stage.

### 4.2.2. Scanning Electron Microscopy

Following XRD analysis, SEM was used to study the microstructure, surface morphology and phase composition. A high-energy electron beam scans the sample's surface and excites the atoms, generating a variety of responses. Emitted secondary electrons (SE), backscattered electrons (BSE), Auger electrons, x-rays, among others, can be used to map the sample's properties. For these experiments, a FEI Quanta 200 FEG-ESEM electron microscope was used.

### 4.2.3. Energy Dispersive X-ray spectroscopy (EDX)

As an attachment to the electron microscope, energy dispersive x-ray spectroscopy (EDX) was employed. EDX allows us to semi-quantitatively identify the elemental composition of a region of the sample. The electron beam from the SEM excites the atoms on the surface of the sample. The high energy is then dissipated by emitting (among other things) x-rays. The x-ray spectrum can then be analyzed to back-calculate different elements amount on the sample's surface. Peak overlap from many elements reduces the accuracy of EDX analysis, yet it is still a useful technique for our characterization purposes.

### 4.2.4. Isotope exachange Gas Phase Analysis (GPA)

GPA was used to probe a variety of properties of the sample. Information on the oxygen stoichiometry, gas surface exchange kinetics, and tracer diffusion were obtained from the experiments. Figure 4.2 shows the experimental setup. The system consists of a quartz reaction tube and a rolling tube-furnace. The gas mix inside the reaction tube can be controlled by a vacuum pump and a series of gas inlets. Opposite from the sample, a leak valve controls a small gas outlet to a mass spectrometer that monitors the gas composition.

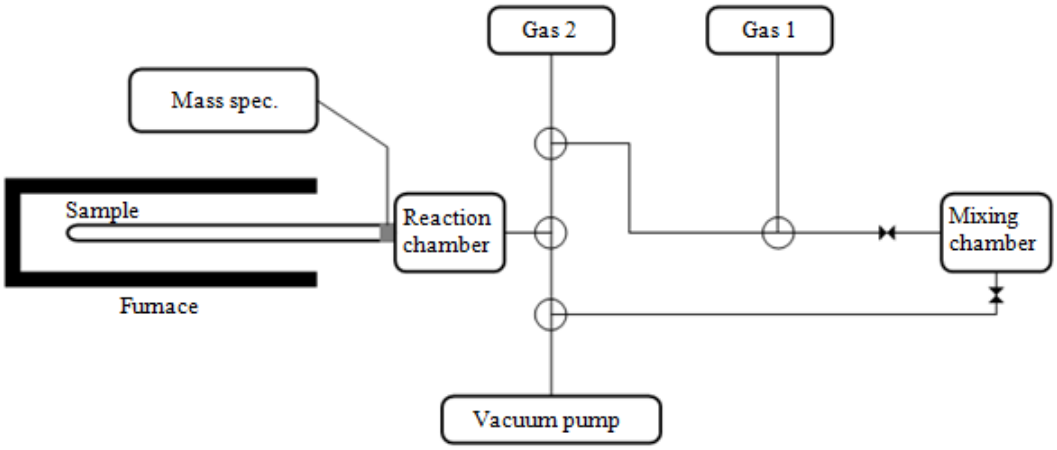


Figure 4.2.: Diagram of the GPA setup.

Powders and pellets were placed in a quartz boat and inserted in the reaction tube. The samples were heated to 900 $^{\circ}$C under low vacuum to remove any water from the

system. After drying, the chamber was filled with oxygen to the desired pressure (0.07 bar to 0.2 bar) and cooled to the temperature of interest (350 ˚C to 800 ˚C). After the oxygen content in the sample reaches equilibrium with the gas, the chamber is again evacuated and refilled with an oxygen isotopic mix to the same pressure as annealing step. The evacuation-refill cycle is repeated until the sample contains the desired isotopic composition of oxygen. When the target has been achieved, a fresh gas mix of $O_2^{32}$ and $O_2^{36}$ with the same isotopic ratio and pressure was used to monitor gas exchange and recombination. These experiments were carried out at the various temperatures as well as oxygen pressures in order to probe the effects.

An attachment to the experimental setup was added to introduce water to the reaction chamber and monitor hydration, and its effect on oxygen transport. The hydration of oxygen vacancies is important to more closely mirror the conditions at which such a material might be employed in a SOFC.

### 4.2.5. Time-of-Flight Secondary Ion Mass Spectroscopy (ToF-SIMS)

ToF-SIMS offers a unique quantitative analysis of the sample's self-diffusion of oxygen and surface kinetics through profiling the composition as a function of depth. A primary ion beam is focused on the sample's surface and secondary ions are ejected from material are collected and analyzed. The ion beam scans the surface creating a crater in the sample as the secondary ions fly to the mass analyzer. Using their charge-to-mass ratio they can be identified. A number of factors limit the technique. For polycrystalline materials (such as the ones used in this thesis) gran size becomes a factor as too large grains might offset measurements due to distinct effects or composition at the boundary. Most importantly for this study, is the crater's depth. For fast diffusers, ions of interest might diffuse past the target depth of 10 um into a regime where the accuracy of the instrument is compromised. The deeper the ion beam scans, the more likely it is for the secondary ions to come from the crater's walls, creating uncertainty in the data.

The first step to the ToF-SIMS measurements is to prepare a sample's oxygen isotopic composition in the GPA setup. BGLC pellets have to be sintered to high relative densities (above 90 %) in order to ensure that any oxygen incorporation in the material is the result of self-diffusion, and not gas flow through the pores. The dense samples are placed in the GPA's reaction chamber and pre-annealed in $O_2^{32}$ at the target temperature and $pO_2$ to achieve a stable stoichiometry. Afterwards, the gas is evacuated and the same

pressure of $O_2^{36}$ is refilled. The sample is then left to exchange oxygen for a short period of time, estimated using:

$$l = \sqrt{Dt} \tag{4.1}$$

Where l is the diffusion depth, $D$ the tracer diffusion coefficient, and t the time. ToF-SIMS limitations only allow for a shallow depth analysis of up to 10 μm (as discussed earlier), with an optimal target of around 5 μm.

### 4.2.6. Thermogravimetric Analysis (TGA)

Thermogravimetry was employed to study a series of properties of the material; hydration, non-stoichiometry and chemical diffusion being the main objectives of the experiments. In the experimental setup, a pellet is hung with platinum wire inside a tube furnace. Attached to it, is an electromagnet and a counter weight that allows relative weight change to be recorded in the software. The entire system is enclosed except for 2 openings, an inlet from a gas mixer, and an outlet on top. The gas-mixer (see section 4.2.7) creates the desired atmosphere from a mix of Oxygen, Argon, Hydrogen, Air and Helium. Once the target atmosphere is achieved, a thermocouple and a digital controller serve to regulate the temperature. Such a setup makes it possible to record weight changes in the sample across any temperature and gas composition.

Two types of experiments were carried out with this setup: isobaric (in terms of $pO_2$) and isothermal. Isobaric experiments consisted of annealing a sample at an initial temperature (25 or 700 $^{o}$C) until equilibrium is achieved. At that point, the temperature is slowly ramped to the other end allowing for equlibrium at fixed steps. The isobaric temperature ramp shows the oxygen stoichiometry of the material as a function of temperature. On the other hand, the isothermal experiments are less concerned with equilibrium and more about the transient behaivior. Annealing is done at a target temperature and $pO_2$ (usually atmospheric). After equilibrium, a step change in $pO_2$ is introduced with the use of the gas mixers, and the mass relaxation curve is evaluated. Isothermal transient-TGA experiments yield information about the oxygen diffusion in the sample.

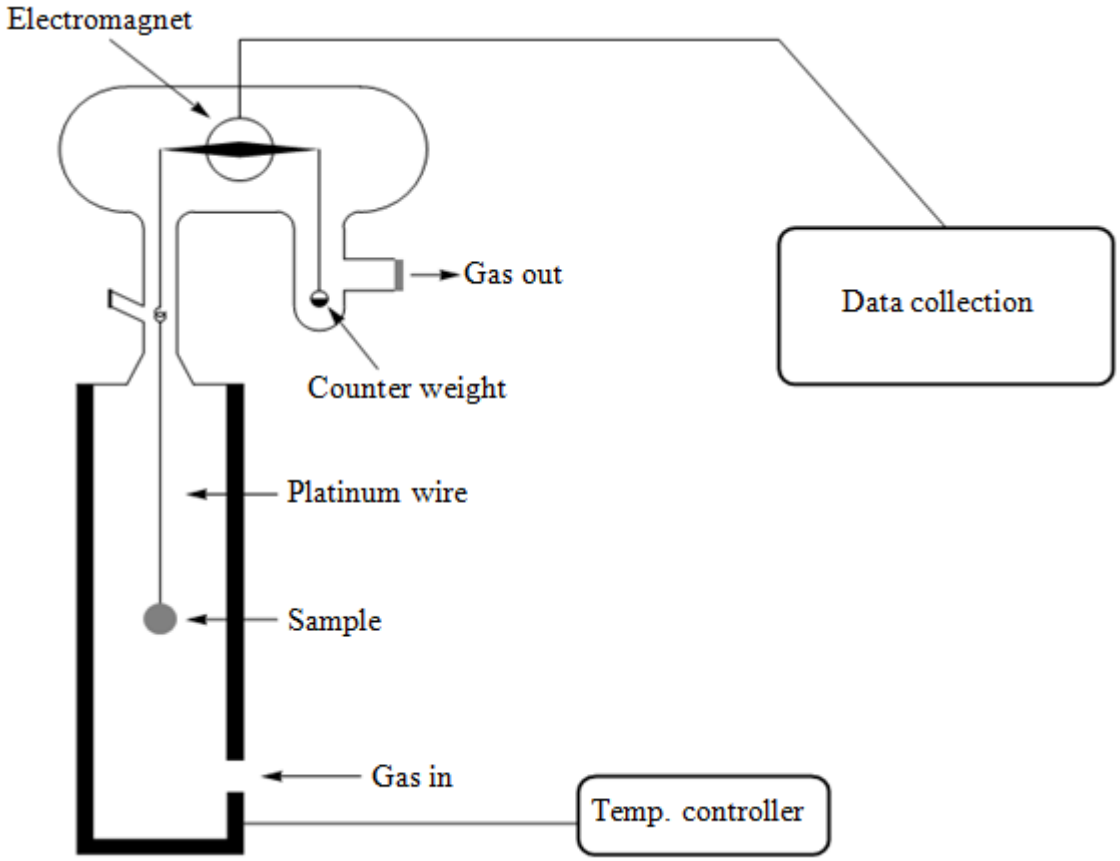


Figure 4.3.: Diagram of the TGA setup.

### 4.2.7. Gas mixers

In order to obtain the desired atmosphere in the furnace for the TG measurements, we used an in-house system of gas mixers. The gas mixer as shown in figure 4.4 is a series of gas lines and flow meters that allows us to create any combination of 2 gases at a slight overpressure (from ambient). Gas 1, in our case oxygen, enters the first flow meter, where the flow can be controlled using a glass floater. At the same time gas 2, the dilution gas, enters the second flow meter which has a heavier, tantalum, floater. The gases then exit and mix into a third flow meter. A fourth flowmeter acts as a second dilution stage. The same process is repeated again until meters 5 and 6. At each dilution stage an outlet is connected to bubblers filled with mineral oil to regulate overpressure and prevent back-mixing.

After Mix 3 exits the meters, it can flow through 4 different paths. Wetting stages, a drying stage and a bypass channel. The wetting stages are filled with $H_2O$ and $D_2O$ respectively, saturating the passing gas to a water (or $D_2O$) content of ~3%. The drying stage is a phosphorous pentoxide buffer; the hygroscopic salt absorbs the moisture in the gas. Lastly, the bypass stage just lets the gas through. The outlets lead into a final pair of gas mixers where the mixture can be diluted with Gas 2 again, or remixed to modify/lower the water content. A last bubbler is used, and the mix then enters the measurement cell or thermal balance.

## 4.3. Errors and uncertainty

There are a number of sources of error in these experiments. Characterization tools such as XRD, SEM and ToF-SIMS are well documented and not particularly unique to this study. In contrast, the TGA and GPA setups are made in house and require further discussion. The temperature for both systems is measured by placing a thermocouple as close as possible to, without touching, the sample (or reaction tube). It follows that there will be a temperature gradient in the tube furnace, adding a level of uncertainty to the data. A flush period in the furnaces follows every time a gas is switched. The data processing relies on gas step changes at the time of measurements so the delays in gas equilibration may impact the results. The GPA setup has an extra possible source of error in measurements. The leak valve sampling gas to the MS will slowly deplete the gas in the reaction tube, which in turn may decrease the pressure in the MS. Finally,

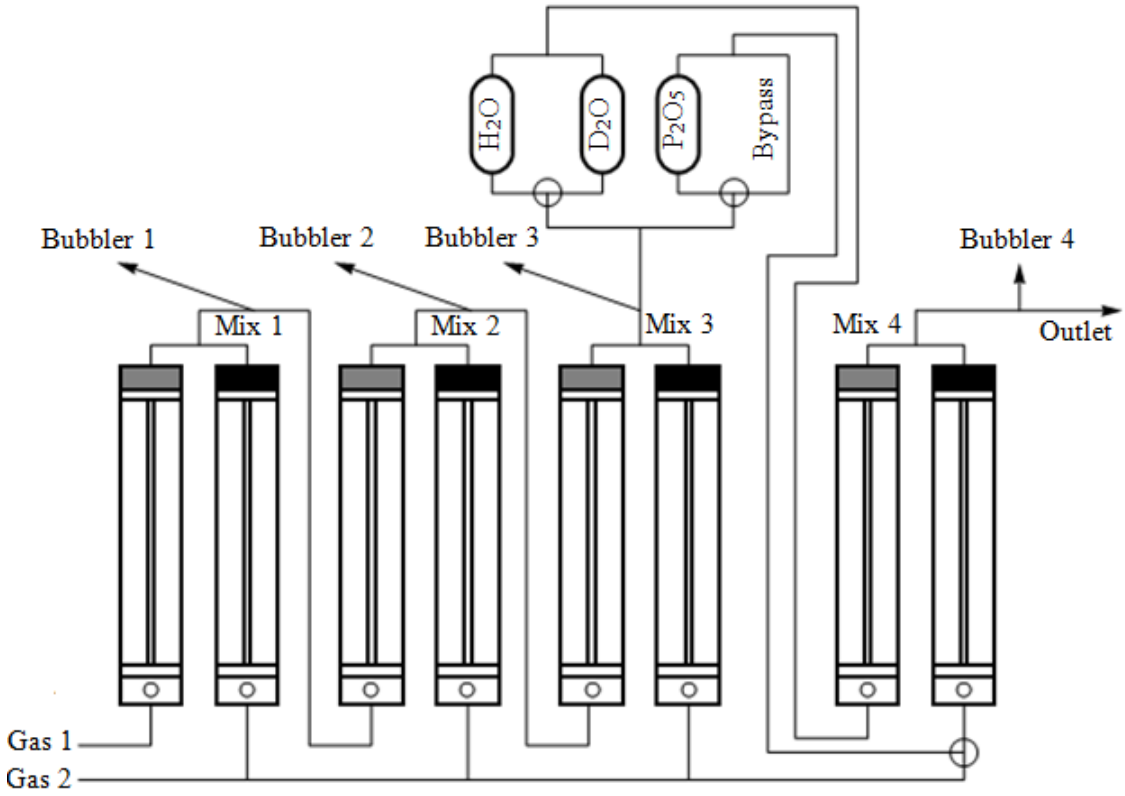


Figure 4.4.: Gas mixer diagram.

in the annealing of samples for SIMS measurements it is assumed that at the time of quenching the sample is not able to exchange anymore oxygen. Cooling times may modify the isotopic profile if it is not fast enough. Experiments are planned in a way to minimize all these uncertainties, but they must always be considered.

# 5. Results

## 5.1. Synthesis and structural characterization

The BGLC compositions, as described in table 5.1 (redrawn from table 2.1 for ease of reading), were synthesized using the same procedure, with similar results. From 10-8-2 to 5-8-7 the lanthanum doping on barium sites increases while keeping the gadolinium constant. All samples were initially synthesized at 1100 ºC. The temperature was reduced until 900 ºC in order to make a more active green body for sintering. When sintering these samples, 1180 ºC temperature was used, higher densities were achieved. After reducing the synthesis temperatures, the density of the sintered bodies was increased from 70-80 % on average to ~93%. Density measurements were made using micrometers (thickness and diameter) and an Archimedes setup.

Table 5.1.: Description of composition of BGLC.

| Composition | Sample name |
|---|---|
| $BaGd_{0.8}La_{0.2}Co_2O_{6-\delta}$ | 10-8-2 |
| $Ba_{0.9}Gd_{0.8}La_{0.3}Co_2O_{6-\delta}$ | 9-8-3 |
| $Ba_{0.8}Gd_{0.8}La_{0.4}Co_2O_{6-\delta}$ | 8-8-4 |
| $Ba_{0.7}Gd_{0.8}La_{0.5}Co_2O_{6-\delta}$ | 7-8-5 |
| $Ba_{0.6}Gd_{0.8}La_{0.6}Co_2O_{6-\delta}$ | 6-8-6 |
| $Ba_{0.5}Gd_{0.8}La_{0.7}Co_2O_{6-\delta}$ | 5-8-7 |

Following the described procedure, the initial composition of BGLC (10-8-2) was achieved. After synthesizing at 1100 ˚C, the difractogram shown in figure 5.1 was obtained. No secondary phases are observed, signaling a phase-pure product. The difractogram (taken at 25 ˚C), points to a tetragonal system with a p4/mmm symmetry group; a similar structure to other double perovskites.

Such a difractogram was obtained from powder, yet the same pattern results from sintered pellets. Reagent phases are seen when the firing time is insufficient. Single phase

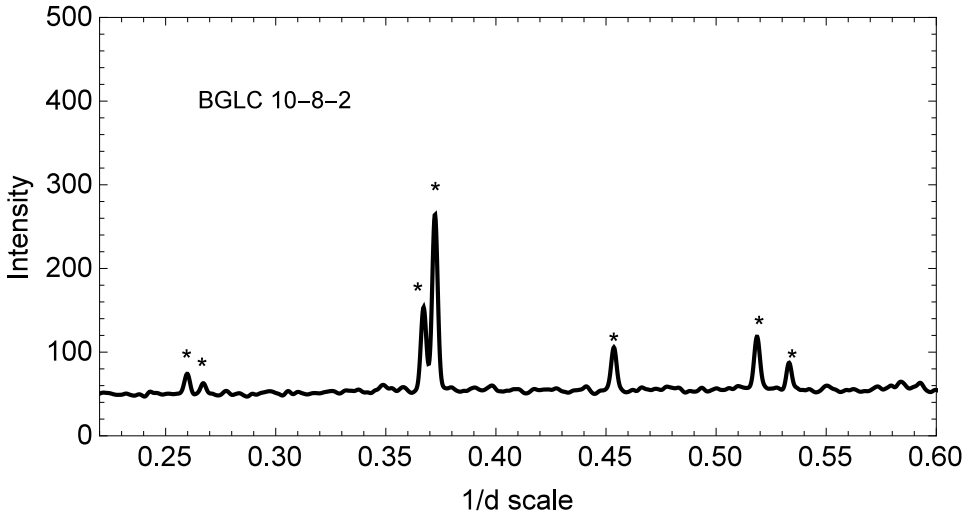


Figure 5.1.: Diffractogram of a BGLC 10-8-2 sample taken at 25 ºC. * = peaks from Strandbakke et al.[44]

BGLC 10-8-2 samples were achieved with synthesis temperatures as low as 950 ºC followed by sintering at 1180 ºC. With increasing lanthanum doping it became more and more difficult to synthesize single phase powders at lower tmeperatures. Most samples of non 10-8-2 BGLC were synthesized at above 1000 ºC.

In order to test the stability of the material across a wide range of temperatures, in-situ xrd measurements were employed. BGLC was fired in air and argon (separetely) from room temperature to 800 ºC and back down with periodic measurements. The results for a sample composition of BGLC, 5-8-7, is shown below. No phase transitions are observed for any sample, in either atmosphere. Stability is preserved and only lattice size changes proportional to increasing temperature appear as expected. All changes in the difractograms are reversible, as they are retraced on the ramp down.

To further characterize and study the material, SEM was employed. The micrographs below help us understand the microstructure of the samples. No detailed analysis from SEM is performed, but qualititative information can still be gained.

Figure 5.3 presents a micrograph of a sintered BGLC 10-8-2 pellet. From the image it can be seen that these are dense samples, of a single phase. Grain sizes can also be obtained from such a micrograph as shown in the histogram. In this case, an average grain size of 3.41 μm is seen.

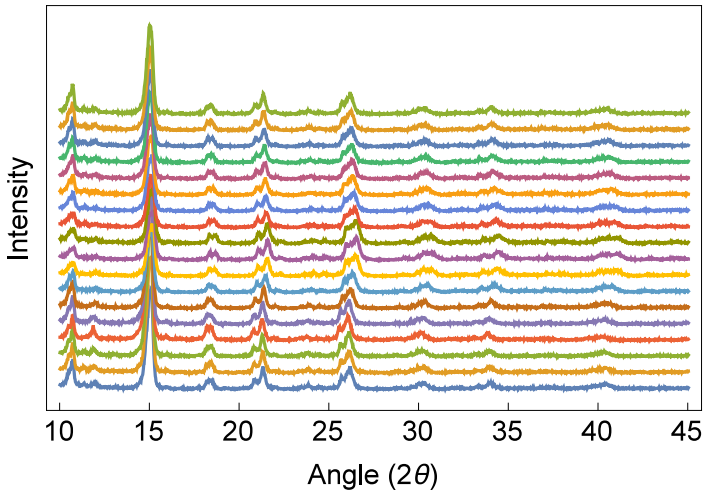


Figure 5.2.: BGLC 5-8-7 in-situ XRD at temperatures ranging from 25 to 800 ºC.

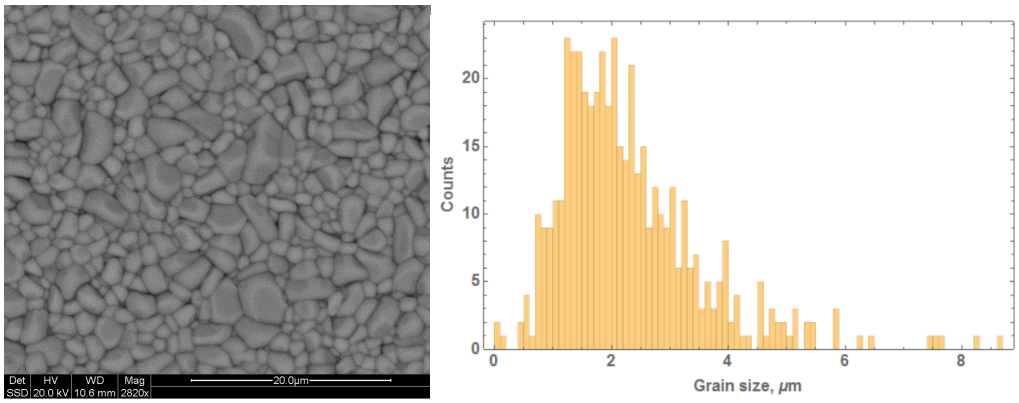


Figure 5.3.: Left: Micrograph of a BGLC 10-8-2 pellet. Right: Grain size analysis.

EDX was also performed on the samples. Such an analysis provides a qualitative elemental composition, and thus, stoichiometry. This way, the samples can be checked for deficiencies in certain metals. An example spectrum, and tabulated results, follows in figure 5.4.

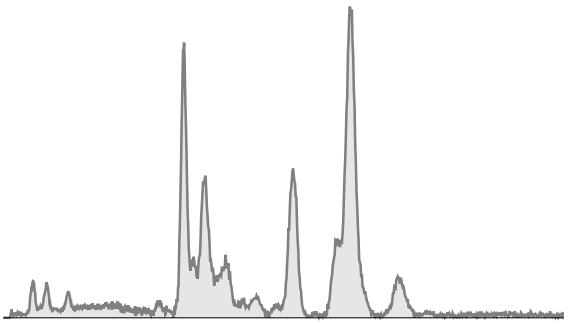

| Element | Experimental mol% | Theoretical mol% |
|---|---|---|
| Ba | 19.02 | 25 |
| Gd | 20.67 | 20 |
| La | 4.83 | 5 |
| Co | 55.47 | 50 |

Figure 5.4.: Semi-quantitative EDX analysis of the micrograph shown.

The spectrum shows a barium deficiency, possibly due to barium evaporation at high temperatures, compensated by cobalt. As mentioned before, these results are qualitative, a guideline to the material's stoichiometry. For the GPA experiments, powders were used. A larger surface area is needed to achieve fast gas exchange results. The powders were characterized the same way as the pellets, and the micrographs of two such samples is shown in figure 5.5.

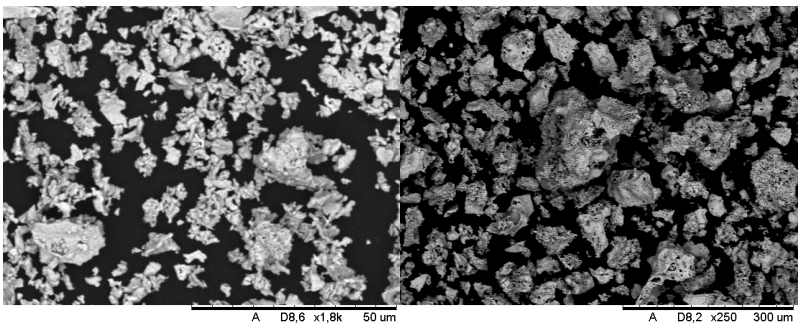


Figure 5.5.: Micrographs of 2 BGLC samples to be used in the GPA.

Synchotron analysis provided by Dr. David Wragg details the atmoic positions and site occupancy of the three oxygen sites (each around a different cation) in 3 different BGLC compositions. Samples of BGLC 10-8-2, 8-8-4 and 7-8-5 were sent for analysis. The results are shown in figure 5.6.

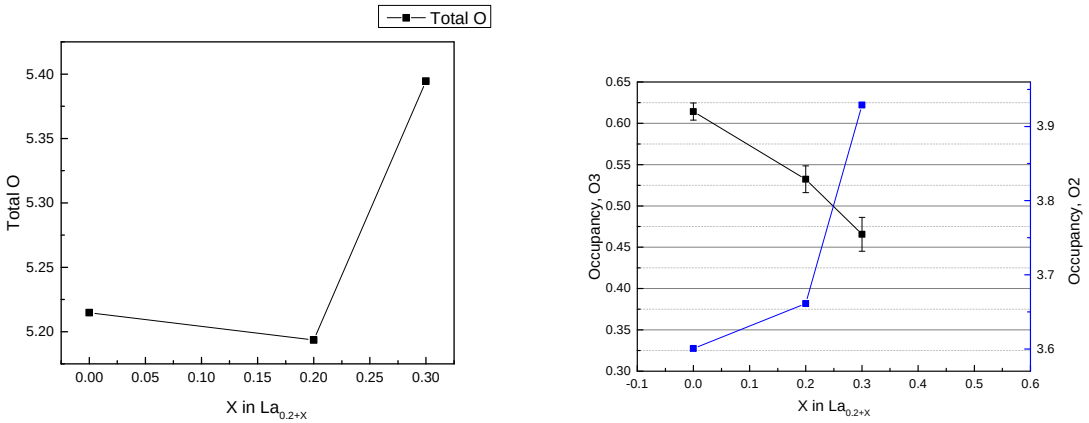


Figure 5.6.: Synchotron data on the oxygen occupancy of BGLC for three different compositions. Left: total oxygen content. Right: oxygen content on the Gd layer (black) and the Co layer (blue).

The oxygen sites shown in the figure 5.6 are defined follows: $Ba-O1_1$, $Co-O2_{4-x}$ and $Gd-O3_{1-y}$. These are the oxygen concentrations at each site at room temperature, and thus will serve as a basis for non-stoichiometry measurements.

For the three compositions the oxygen around the barium layer remains full at room temperature. The oxygen aroun gadolinium (the most vacant site) decreases with increasing lanthanum content. This effect is countered by an increase in oxygen content around the cobalt with increasing lanthanum. The two competing effects result in a minimum of total oxygen content at 20% lanthanum doping among the three compositions sampled. The trends suggest that doping above 30% will decrease the total oxygen content again, given that the cobalt-oxygen is almost ful (~3.94 / 4.0) and the gadolinium-oxygen change seems monotonic.

## 5.2. Gas Phase Analysis

Surface exchange coefficients were obtained from the gas phase analysis setup as described in section 4.2.4. Figure 5.7 shows some of the concentration profiles of the 3 oxygen molecules ($O_2^{32}$, $O_2^{36}$, $O_2^{34}$) at 5 different temperatures, from 350 to 550 ºC at 50 ºC intervals. The relative rates increase from 350 to 400 ºC, after which the rates remain roughly constant with increasing temperature. All the profiles are well described by the model.

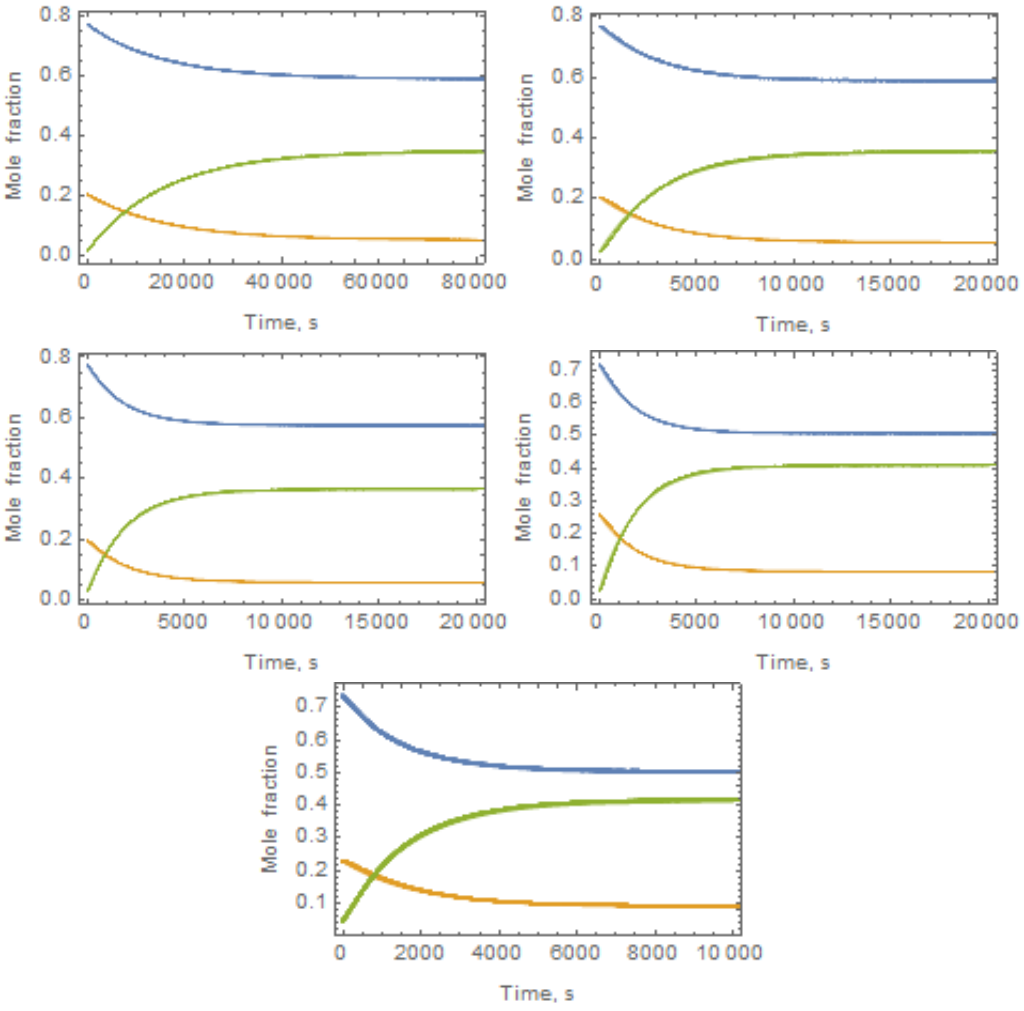


Figure 5.7.: Homomolecular exchange for a BGLC 10-8-2 sample at temperatures: a) 350 b) 400 c) 450 d) 500 e) 550. The blue and orange lines are $O^{16}{}_2$ and $O^{18}{}_2$, while the green line is the evolution of $O^{16}O^{18}$. The data is overlapped by the fitted curves.

Equation 2.25, describing homomolecular gas exchange rate based on the statistical probabilities of forming the gas molecules, models the data closely and generates repeatable surface exchange coefficients. To better view the constant exchange rate throughout the experiment the data can be linearized through equation 5.1. The slope quantifies the rate.

$$\log\left(\frac{c(t)-c_{eq}}{c_0-c_{eq}}\right) = -\frac{RS}{n}t \tag{5.1}$$

Where R is the exchange rate, S is the surface area, n is the number of moles of gas in the chamber, c is the concentration of a species at the respective times, and t is the time.

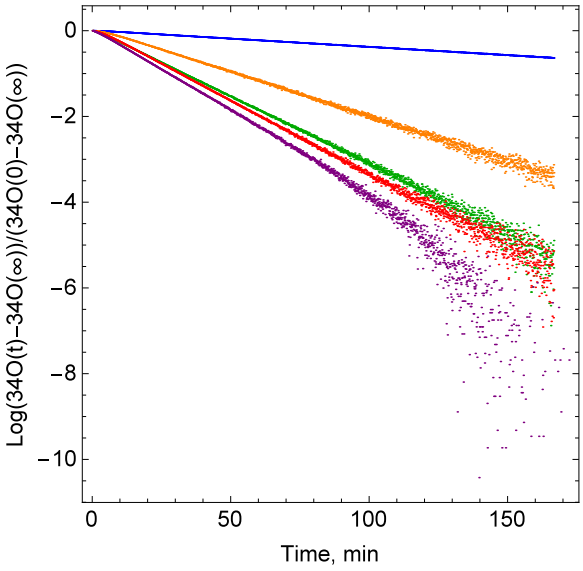


Figure 5.8.: Linearized concentration profiles of 34O2 from homomolecular gas exchange in BGLC 10-8-2 at different temperatures versus time.

The extracted values for RS are used in an Arrhenius plot to extract a temperature in dependency in figure 5.9. It can be seen that the exchange rate quickly reaches a maximum and is unaffected by temperature above 500 ºC (depending on the amount of sample). The region at low temperatures was used to calculate activation energies for the process, 106 kJ/mol. At high temperatures, the rates stop increasing at $\sim 1*10^{-7} mol/s$ of gas exchanged.

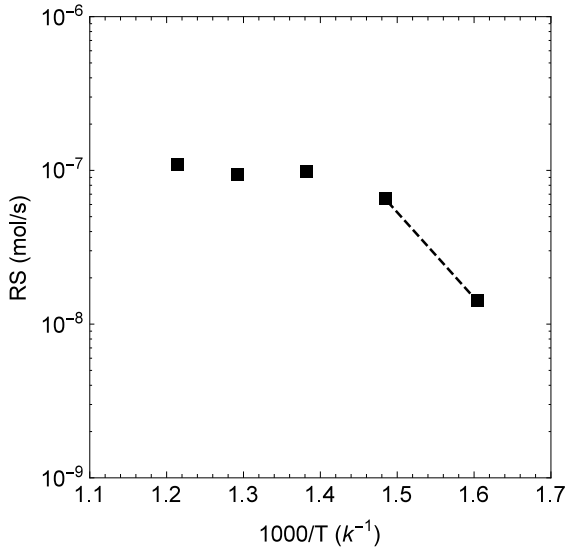


Figure 5.9.: Arrhenius plot of RS for BGLC 10-8-2. Only the first 2 points are used to extract an activation energy.

Figure 5.10 shows the similar resutls with BGLC 8-8-4 and a different powder size and mass. With an activation energy of 101 kJ/mol, slightly lower than for BGLC 10-8-2, yet within the same order. The same limitation is reached at approximately $1 * 10^{-7} mol/s$ of gas exchanged.

In an attempt to gain further insight into the gas exchange process, different pressures were used. The exchange rates of gas at the surface of the sample depend not only on temperature and sample composition/morphology, but also in pressure. The oxygen pressure (which makes up the entire system as no other gases are used) was varied from 50 to 200 mbar in different intervals. This was repeated at a series of temperatures in order to probe possible changes in $pO_2$ dependencies with changing temperature. The slopes for the two temperatures shown below 400 and 450 ºC) are 0.82 and 0.86 respectively. See figure 5.11.

Past homomolecular exchange experiments, a series of other measurements were performed. During the annealing process to prepare samples for the homomolecular experiments, heteromolecular exchange is observed. The procedure is as follows. The fresh BGLC 10-8-2 powders synthesized under atmospheric conditions are placed in the GPA chamber. The samples are annealed to the target temperature in $O_2^{16}$. The gas is vacuumed out and the chamber is refilled with $O_2^{18}$to the same pressure as before. During this last step, the sample will exchange oxygen with the gas until the isotopic composition

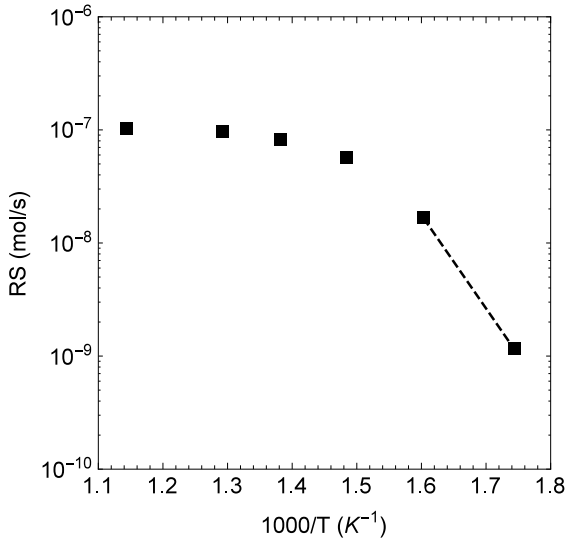


Figure 5.10.: Arrhenius plot of the rates, R, times the surface area, S, versus inverse temperature for BGLC 8-8-4.

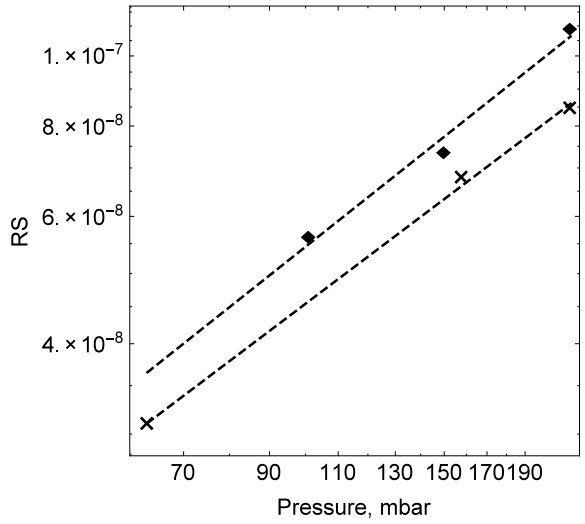


Figure 5.11.: Logarithm plot of the rates, R, times the surface area, S, versus oxygen pressure. The yellow points were taken at 450 ºC, while the blue ones at 400 ºC. The solid lines are linear fits.

of the bulk reaches equilibrium with the gas phase. The masses of the gas molecules, as well as the single atoms $O^{16}$and $O^{18}$are recorded to model the process. See figure 5.12.

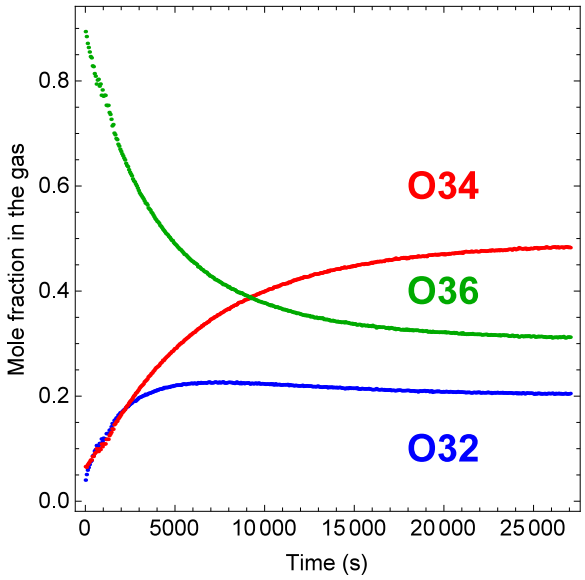


Figure 5.12.: Gas concentration profiles after exposing a BGLC 10-8-2 to $O^{18}{}_2$ at 350 ºC.

When compared to the homomolecular exchange profiles a number of differences immeditely arise. The profile for $O_2^{32}$peaks early in the reaction and decreases to an equilibrium value. The profiles for $O_2^{36}$ and $O_2^{34}$follow a monotonic decrease and increase respectively. Ultimately, these profiles cannot be modeled with the same equation used for homomolecular exchange due to the changing isotopic composition in the gas. The changing isotope profiles in the gas are shown in figure 5.13.

The isotope profiles in figure 5.13 can be manipulated to reflect the concentrations inside the sample. Figure 5.14 shows the sample's isotope concentration profiles. Note the starting points with pure $O^{16}{}_2$, progressing all the way to the equilibrium set by the new gas phase composition.

These isotope profiles can be modeled with equation 2.49 as described in section 2.5.2. The model described adjusts to the current geometry and experimental setup, needing only the particle size for the sample. The isotope diffusion is normalized for a relative change and fitted. The results are shown in figure 5.15. It can be seen that the model is in good agreement with the data. From this curve values for $D^*$and $k$ can be obtained.

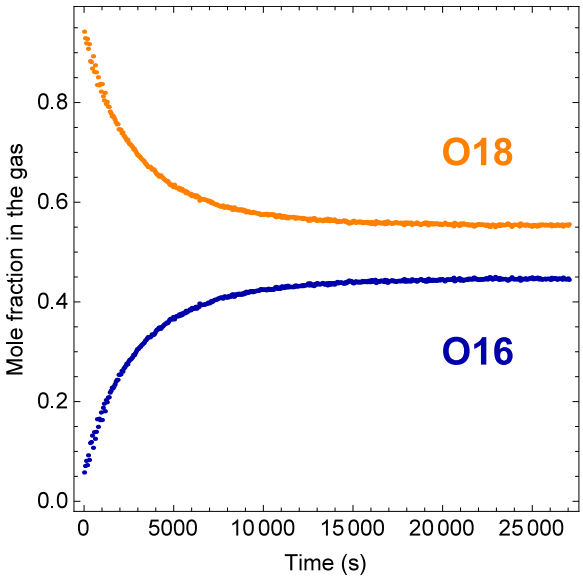


Figure 5.13.: Isotope concentration profiles in the gas after exposing a BGLC 10-8-2 to $O^{18}{}_2$ at 350 ºC.

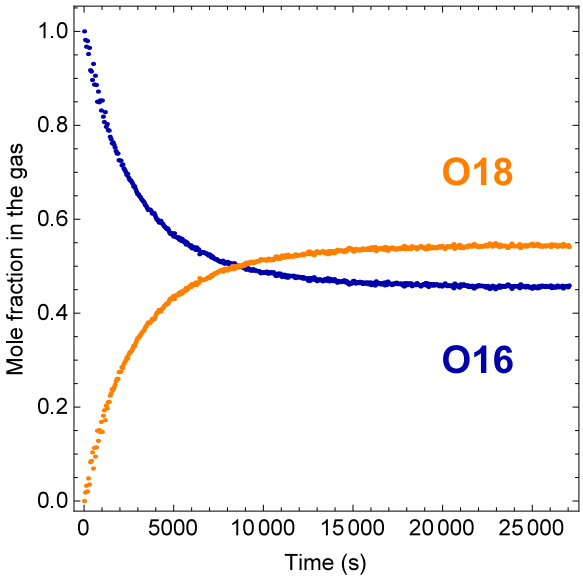


Figure 5.14.: Isotope concentration profiles in the sample after exposing a BGLC 10-8-2 to $O^{18}{}_2$ at 350 ºC.

SEM images were taken to obatin the particle size as shown in figure 5.16. The average particle radius, fitting a spehre, was found to be 26.2 μm.

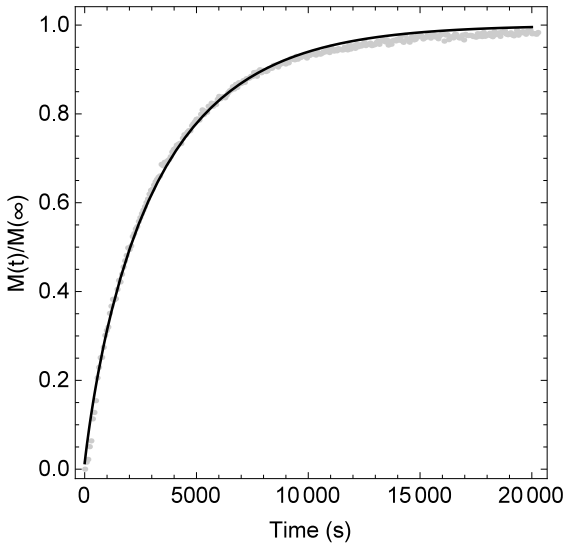


Figure 5.15.: Normalized $O^{18}$ profile in a BGLC 10-8-2 sample after being exposed to $O_2^{36}$ in the GPA setup. The solid line is the fit from the diffusion model.

Towards higher temperatures the exchange process becomes quicker and quicker. The timescale at 450 ºC is short enough that the initial delay observed at the beggining of the exchange curves becomes significant. See figure 5.17. This makes higher temperature runs uncertain, as the delay in the exchange rate will begin to interfere with the data. This small disturbance below 400 seconds is nominally attributed to the time required for adsorption on the sample's surface to trigger the exchange the reaction. For fitting purposes, this segement was excluded from the data at the moment of extracting $D^*$and $k$.

Following the procedure described, the experiment was repeated over 3 temperatures from 350 to 450ºC. The Arrhenius plot for both $D^*$and $k$ is shown in figure 5.18. Both properties follow a linear relationship in the temperature range with little scatter. Equations 2.36 and 5.2 describe the fit.

$$k = k^0 \exp\left(\frac{E_a}{RT}\right) \tag{5.2}$$

With the fitting parameters outlined in table 5.2. It can be seen that $k$ is around 3 orders of magnitude higher than $D$ at lower temperatures. The gap is reduced with

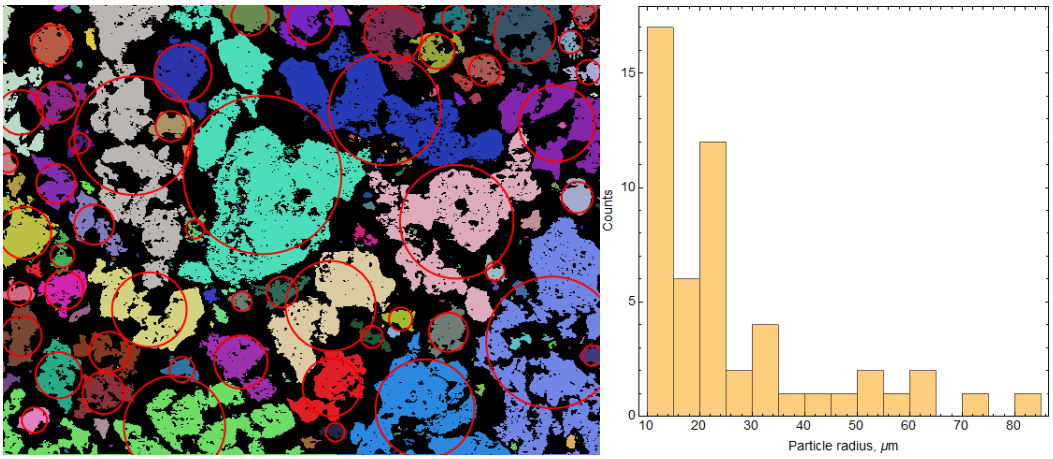


Figure 5.16.: a) sample SEM image of the BGLC 10-8-2 powder used for the previous experiments. The red cricles are the disks fitted to the individual componenets to determine their radius. b) Histogram of the radii extracted from the SEM image above.

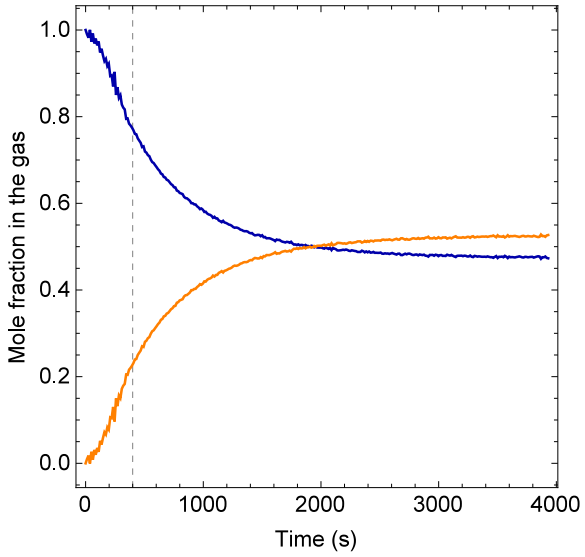


Figure 5.17.: Isotope concentration profiles in the sample after exposing a BGLC 10-8-2 to $O^{18}{}_2$ at 450 ºC. $O^{18}$ and $O^{16}$ are orange and blue respectively.

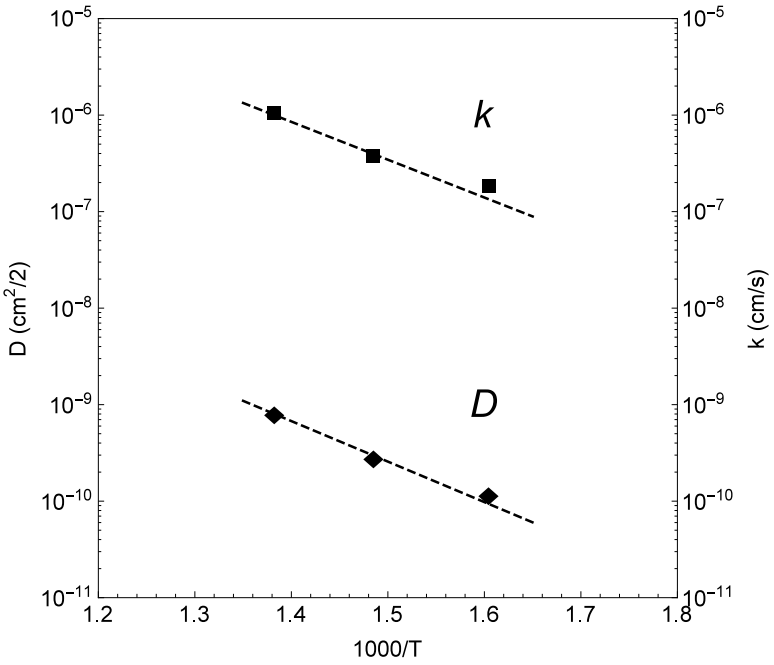


Figure 5.18.: Arrhenius plot of the diffusion and surface coefficient over 3 temperatures.

increasing temperature as the activation energy for the surface coefficient is lower than for diffusion.

Table 5.2.: Fitting parameters for the diffusion and surface processes from GPA experiments.

| | Activation energy (eV) | pre-exponential factor |
|---|---|---|
| $D$ | 0.74 | $1.19 * 10^{-4}$ |
| $k$ | 0.66 | $4.08 * 10^{-2}$ |

## 5.3. Thermogravimetric Analysis

The initial TGA experiments are the isobaric temperature runs from room temperature to 800 ºC for dehydration and resetting of the oxygen stoichiometry. After a short dwell time, the termperature is ramped down to 200 ºC in intervals of 50 or 100 ºC. At each step equilibrium is achieved by holding the constant temperature and allowing the sample to relax. The equilibrium points provide the mass at those temperatures and allowed plotting of the changing oxygen content with tempreature. The sample used was BGLC 7-8-5. Results for this experiment are shown figure 5.19. The stoichiometry of BGLC 10-8-2 versus temperature was already measured previously by Strandbakke et al.[44]

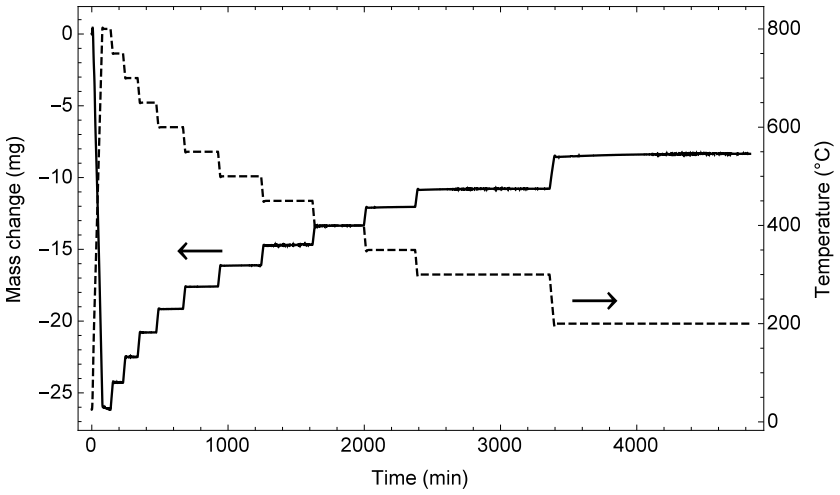


Figure 5.19.: Mass change for a BGLC 7-8-5 sample of 2520 mg across a temperature range in a dry oxygen in argon mixture ( $pO_2 = 0.2$bar). The solid line is the mass change, the dotted line is the temperature change. The reference state is at room temperature in air.

A similar measurement was repeated with a wet mix using 3% water. The oxygen pressure is constant. The TGA ramp showing the mass change due to simultaneus oxydation and hydration is shown in figure 5.20.

The equilibrium stages were designed so longer dwell times were used for lower temperatures to account for the slower kinetics. At high temperatures the mass relaxation

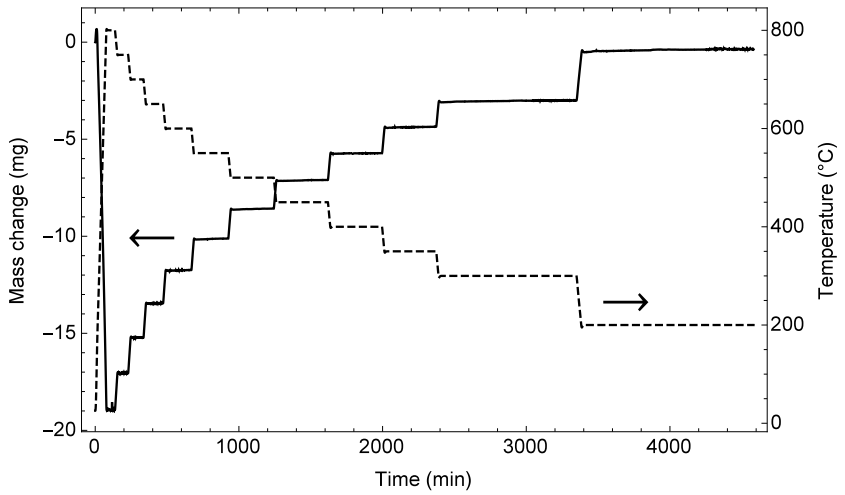


Figure 5.20.: Mass change for a BGLC 7-8-5 sample of 2520 mg across a temperature range in wet oxygen (3% water) in argon mixture ( $pO_2 = 0.2$bar). The solid line is the mass change, the dotted line is the temperature change. The reference state is at 200 $^{o}$C in dry oxygen conditions.

profiles mirror the temperature ramp rates, suggesting fast kinetics. Yet at lower temperatures a slow equilibration process is seen after the initial, fast, mass change. Figure 5.21 shows a side-by-side comparison of two sample mass change profiles for dry and wet conditions.

It can be seen that the mass closely follows the temperature change including the peak from the temperature overshoot due to the quick ramp rates. At 600 $^{o}$C (and similar temperatures) oxygen diffuses in as fast the temperature permits. At 300 $^{o}$C a slower weight increase can be seen extending for orders of magnitude longer than the initial jump. In relative terms, the mass change of the slow process accounts for only a small fraction of total oxygen uptake. Less then 0.1 mg versus the 1.2 mg of the overall oxidation. A similar behavior is seen for the hydration experiment. The magnitudes are greater due to hydration of the material, but the 2 time-scales are conserved. The plateau's in the TG curves can then be taken as the equilibrium mass for the respective temperature and stoichimetry plots can be made for the dry and wet cases.

The curves in figure 5.22 were made under the assumption that at high temperatures BGLC is fully dehydrated and the masses from both curves are equal. It can be seen

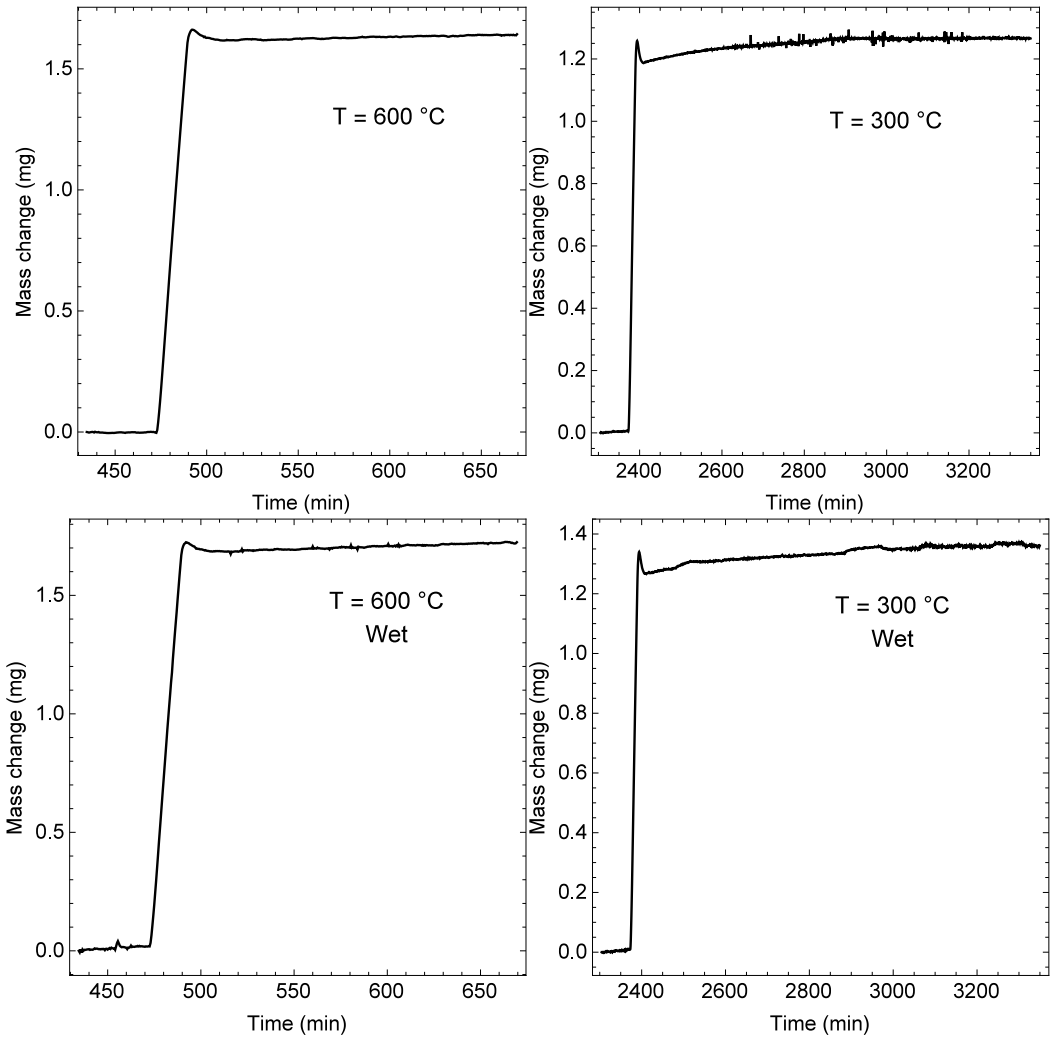


Figure 5.21.: Close up of the mass change after a 50 ºC temperature decrease for different final temperatures.

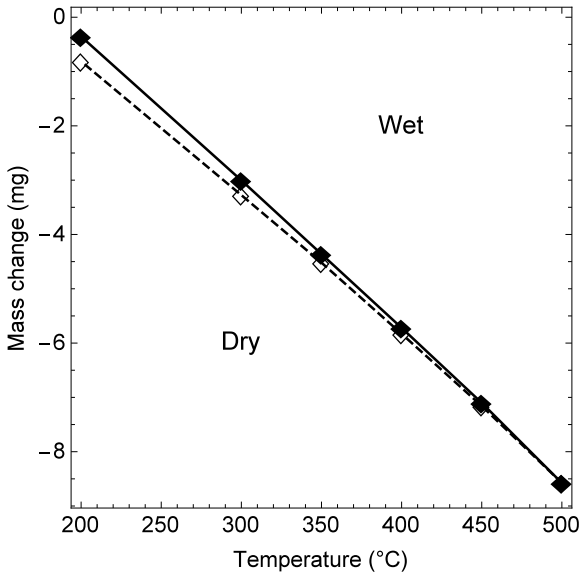


Figure 5.22.: Equilibrium mass change versus temperature for wet and dry conditions from TGA for BGLC 7-8-5.

that from 600 to 800 ºC very little water is incorporated. After this, the curves deviate from each other with increasing water content up to 200 ºC. The difference between the experiments is quantified in figure 5.23. While roughly linear, the scatter in the data can be attributed to the lack of equilibrium at certain points. At 200 and 300 ºC the temperature was held for longer times and equilibrium was fully achieved. For intemediate temperatures (350 to 500 ºC) the time might have been insufficient. Higher temperatures react significantly faster, so shorter times were used.

The same experiment was repeated for BGLC 5-8-7. In this case the temperature was ramped to room temperature at the end, as opposed to the 200 ºC end point for BGLC 10-8-2. The results were similar for the most part; but the magnitude of oxygen stoichiometry change, and hydration, both decreased sharply.

The sample's behavior at low temperatures approaching 25 ºC is difficult to interpret. In figure 5.25 the mass increases sharply below 100 ºC, this is attributed to surface water and is excluded from protonation calculations as the bulk vs surface water cannot be decoupled. Otherwise the mass profile for the sample in wet oxygen follows the dry profile and only changes in magnitude.

Transient TGA experiments were performed by annealing at the target temperature, then introducing a step change in the pO2 (with hellium as the carrier gas) and recording

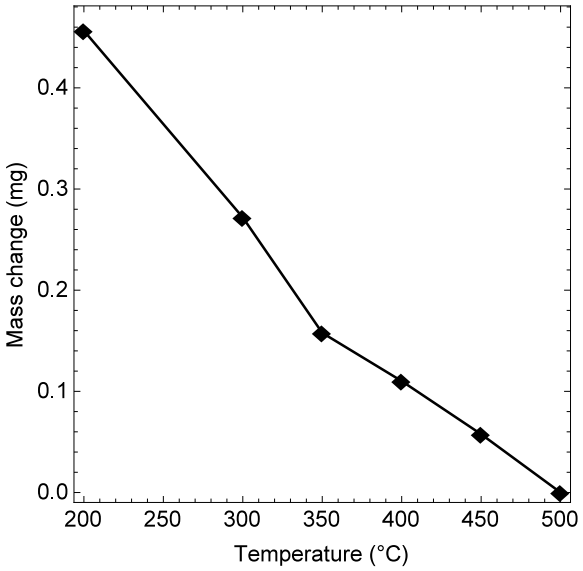


Figure 5.23.: Mass change difference between hydrated and dry BGLC 7-8-5 versus temperature for wet and dry conditions from TGA across a temperature range.

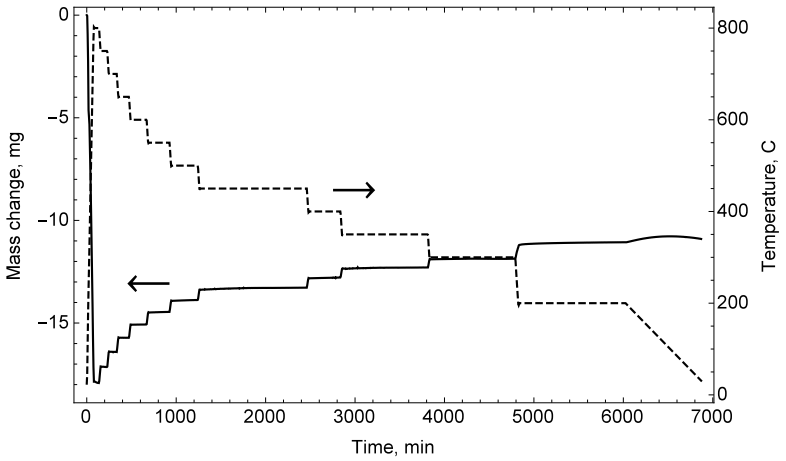


Figure 5.24.: Mass change for a BGLC 5-8-7 sample of 1497 mg across a temperature range in a dry oxygen in argon mixture ( $pO_2 = 0.2$bar). The solid line is the mass change, the dotted line is the temperature change. The reference state is at room temperature in air.

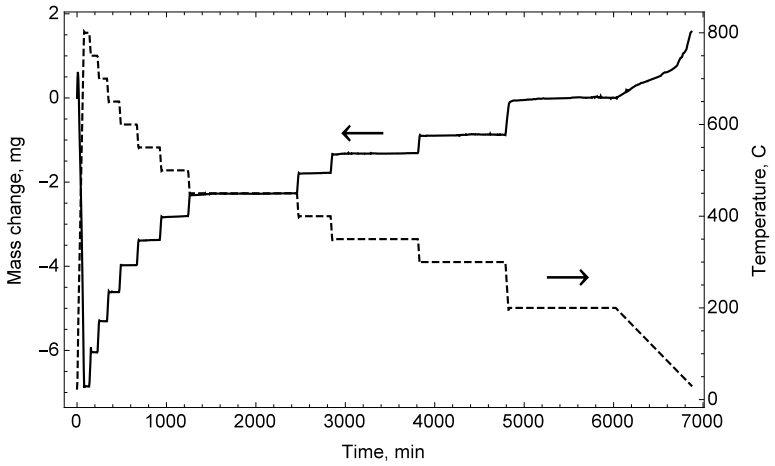


Figure 5.25.: Mass change for a BGLC 5-8-7 sample of 1497 mg across a temperature range in wet oxygen (3% water) in argon mixture ( $pO_2 = 0.2$bar). The solid line is the mass change, the dotted line is the temperature change. The reference state is at room temperature in a dry $O_2/Ar$ mix of the same $pO_2$.

the mass relaxtion curve. In every experiment, the steps were taken in both directions, oxidation and reduction, in order to test any changes, and prove the reversibility of the process. Examples of such curves are shown in figure 5.26. The sample used for these was BGLC 10-8-2 .

The data can then be fitted by equation 2.45 as discussed in section 2.5.1, the normalized mass changes give rise to the material's parameters $D_{chem}$ and $k$. Depending on the sample thickness either one of these paramteres can be excluded form the model. A thick slab will be limited by diffusion with surface exchange playing a negligible role. The sample thickness in this case was chosen to delay the diffusion process. The experimental setup is such that when there is a pressure change introduced, the TG chamber takes around 10-20 minutes to flush the new gas. To keep the data true, the measurements must be done away from this regime. Thick slabs and high gas flow were the preferred method to obtain accurate relaxation curves at high temperatures.

Figure 5.27 shows the diffusion equation fit. The model for diffusion controlled transport correctly describes the curve. Values for $D_{chem}$ are extracted from the data and collected for a range of temperatures and gas flowrates. From the equation used (2.48) and the

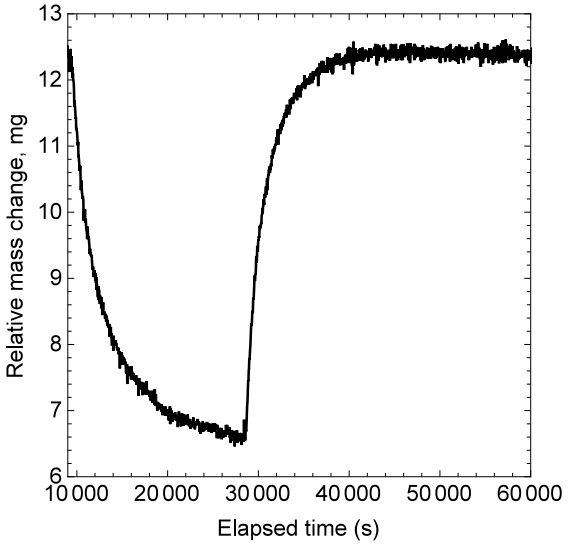


Figure 5.26.: Transient TGA raw data for BGLC 10-8-2 at 650 ºC showing reduction and oxidation steps between oxygen partial pressures of 0.21 bar and 0.01 bar.

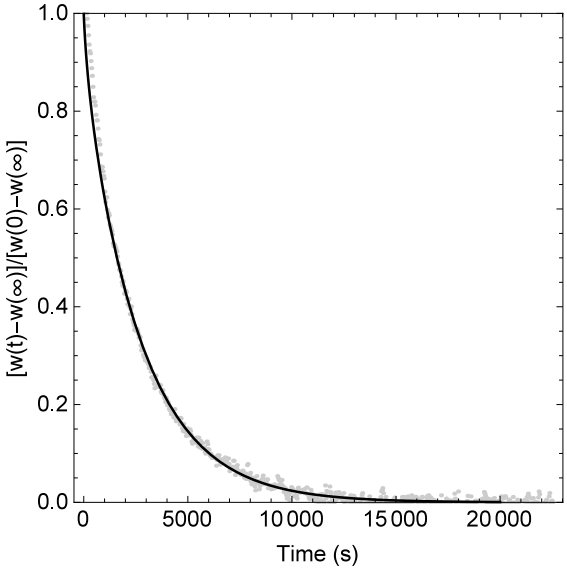


Figure 5.27.: Sample TGA curve of normalized mass change vs time fitted to the model discussed in equation 2.45 after a $pO_2$ step change is introduced.

sample thickness chosen, $k$ cannot be extracted. Thus, only $D_{chem}$ is reported from these experiments.

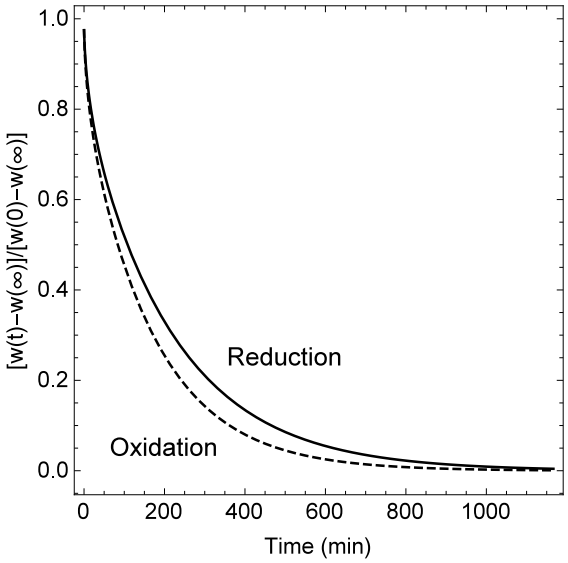


Figure 5.28.: Normalized mass change vs time for the reduction and oxidation steps for the same temperature and pressure change.

It is shown that there is a slight difference in the rates of reduction and oxidatin in these experiments. The same effect is seen literature but seldom discussed. The oxidation step is faster for all the measurements of $D_{chem}$, suggesting that the pressure dependence of the coefficient ($D_{chem} \propto pO_2^n$) is determined by the final pressure.[45] More experiments with different pressure step changes are needed to quantify the dependence.

Arrhenius equations descirbe the diffusion process. A regular fit of $\log(D)$ vs $\frac{1}{T}$ as per equation 2.36 will yield the activation energy and pre-exponential factors of the processes.

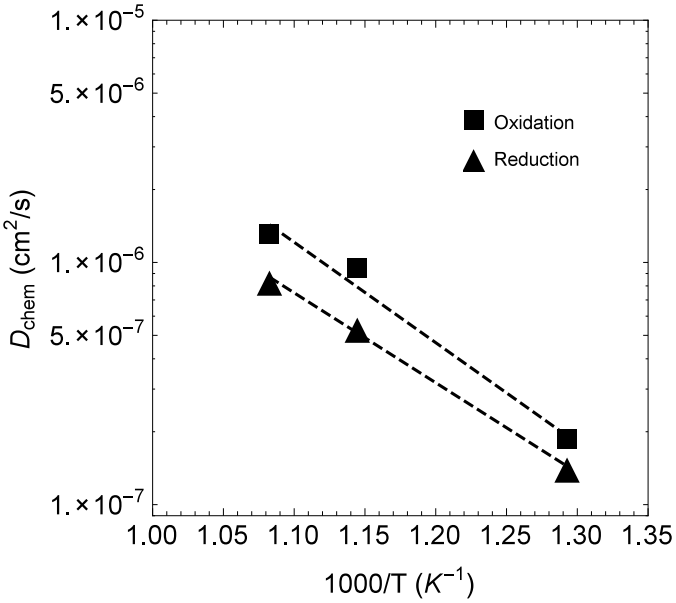


Figure 5.29.: Arrhenius behavior of $D_{chem}$over the specified temperature range. Oxidation and reduction measurements are shown.

In figure 5.29 the linear relationship between $D_{chem}$ and 1/T is confirmed. For high temperatures the kinetics increased to the point were the chamber flush time became a concern. Max gas flow (as the setup allowed) was used to reduce the chamber flushing time and keep it from interfering with the data to a significant degree. The results show that minor increases arise from the high flow, particularly in the reduction step. Suggesting that slow desorption could indeed be responsible for the differences in rates between oxidation and reduction. Regardless of the flow, the values of $D_{chem}$ at 650 ºC remain around $2*10^{-6}cm^2/s$ for oxidation and $1*10^{-6}cm^2/s$ for reduction with reasonable consistency. The activation energy extracted from the linear regression according to equation 2.36 is 0.71 eV. The same experiment was repeated for BGLC 7-8-5, the resulting coefficients (shown in table 5.3) are the same as for BGLC 10-8-2 within the uncertainty of the measurement.

Table 5.3.: Activation for the oxidation diffusion process through reduction and oxidation from TGA.

| | BGLC 10-8-2 | BGLC 7-8-5 |
|---|---|---|
| $E_a$(eV) | 0.71 | 0.66 |
| $D^0_{chem}(cm^2/s)$ | $9.1*10^{-3}$ | $4.5*10^{-3}$ |

## 5.4. SIMS

As described in section 4.2.5, SIMS experiments are performed by first annealing in the GPA setup to the proper stoichiometry, and then having a quick exchange in isotopically enriched gas. The sample is then quenched to room temperature where no exchange is assumed and taken to the SIMS. A depth profile of $O^{18}$ concentration in the sample is obtained and shown in figure 5.30.

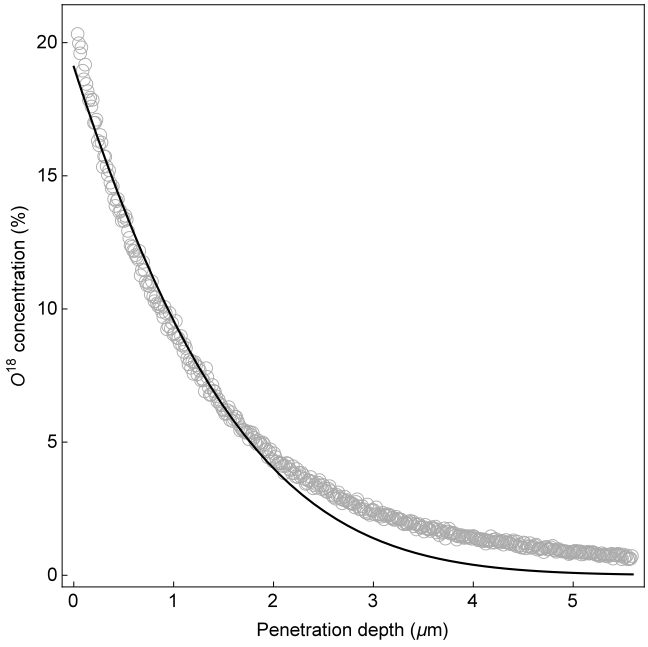


Figure 5.30.: $O^{18}$ concentration depth profile of a BGLC 10-8-2 pellet from SIMS. The solid line is themodel fit.

It can be seen that the diffusion profile is not precisely described by equation 2.56. The extended tail deeper into the sample has been known to relate to grain boundary diffusion[46], thus the bulk values for $D$ and $k$ are taken from the first part of the profile.

# 6. Discussion

The aim of this section is to explain the results presented, address the questions posed, and discuss the implications of this thesis.

## 6.1. Structural insights

The synthesis of BGLC proved successful and resulted in single phase powders at calcination temperatures from 1000 to 1100 ºC. Even powders calcined at 900 ºC that still showed reactants' phases transitioned into single phase BGLC after sintering. The density of the sintered pellets was an always present concern. It ranged from ~88% of the theoretical density to ~98%, depending on the powder and sintering conditions. Compositions with increasing lanthanum content required higher synthesis temperatures to achieve a single-phase material, resulting in lowering densities (on average). XRD and SEM confirmed the phase purity and structure of the material. Compositions were found to be uniform through the samples. Refinements led to a p4/mmm tetragonal symmetry with a doubled c-axis. The layered double perovskite unit cell encountered is expected from literature on similar materials ($LnBaCo_2O_{6-\delta}$). Unlike GBCO, no phase transitions were seen for BGLC. It showed a stable phase throughout the measured temperature range. Keeping the $1a_px1b_px2c_p$ cell that GBCO irreversibly transitions into at high temperatures.

One of the main structural features affecting the results of this thesis is the arrangement of the oxygen atoms. In section 3.2 it was shown that these double perovskites achieve fast oxygen diffusion due to oxygen vacancy aggregation around the lanthanide. The high values and low activation energy of $D$ for BGLC shown here suggest the same, but it is too indirect a measure to acertain the oxygen arrangement. The data from figure 5.6 gives the room temperature oxygen site occupancies and confirms this hypothesis. A

large number of vacancies are seen in the lanthanide layer for all compositions. Meanwhile, the barium oxide layer retains full occupancy and the cobalt oxide layer exhibits composition-dependent flexibility. See figure 6.1

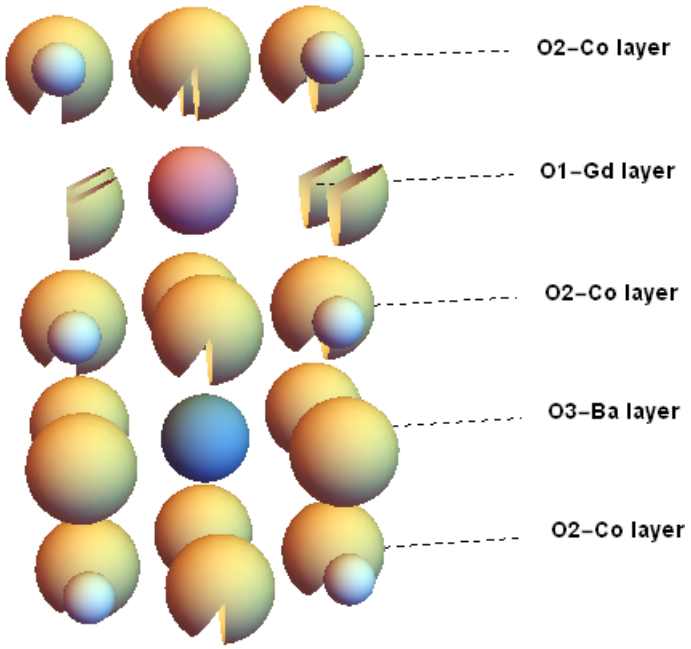


Figure 6.1.: Diagram of a BGLC 10-8-2 unit cell at room temperature. Each oxygen layer posseses a different degree of occupancy represented by the fractions missing in the spheres. Blue is barium, red is gadolinium/lanthanum, grey is cobalt and orange is oxygen.

Only BGLC 10-8-2 contains completely separate lanthanide and barium sites. Every composition thereon has Lanthanum doping barium sites. This has a number of consequences. Lanthanum functions as a donor dopant compensated by electrons (localized in cobalt) and a decreased number of vacancies in all layers. Finally, the lower barium concentration also reduces the basicity of the material, reducing protonation.

BGLC 10-8-2 and 7-8-5 were shown in section 5.3 to have essentially the same oxygen

diffusion coefficient. This suggests that the diffusion path is indeed the same and that only the quantity of vacancies changes. Since the barium sites are significantly different between these compositions (0 to 30% doped) it reinforces the idea that diffusion is occuring almost entirely through the $Gd{-}O_{1-\delta}$ layer and the rest of the oxygen/vacancies sites are relatively immobile.

## 6.2. Defects of BGLC and similar double perovskites

With this information a defect model can take shape. As shown in section 3.3, previous attempts at describing the behavior of double pervoskites in literature have had mixed results. GBCO and PBCO have been modeled by Tsvetkov et al. to a relative degree of success. Their data is modeled closely, but certain compromises are made in terms of structural consideration.

Given that these double perovskites (GBCO, PBCO, BGLC) rely on highly vacant oxygen channels for ionic transport, the defect structure used should at least attempt to conserve this feature. The model presented here can be generalized to any of the mentioned lanthanides, not just gadolinium. The reference state chosen is $BaLnCo_2O_6$. A full lattice at [O] = 6 then places +3.5 as the ideal charge on cobalt sites (assuming that the lanthanide is always +3). This leads to all the cobalt species ($Co^{2+}$, $Co^{3+}$and $Co^{4+}$) having an effective charge in the structure, as per Norby defect notation for inherently defective structures. Furthermore, it has been thoroughly discussed that the oxygen site around $Ln$ (here named O1) is more mobile, the reference state can then be described more precisely as $BaLnCo_2(O1)_1(O2)_5$.

The list of pertinent defects is shown in table 6.1

Table 6.1.: Defect list for the double perovskite model.

| Defects | | | | | | |
|---|---|---|---|---|---|---|
| $Co_{Co}^{1/2'}$ | $Co_{Co}^{1/2\cdot}$ | $Co_{Co}^{3/2'}$ | $O_{O1}^{X}$ | $O_{O2}^{X}$ | $V_{O1}^{\cdot\cdot}$ | $V_{O2}^{\cdot\cdot}$ |

The first reaction to consider is cobalt disproportionation.

$$Co_{Co}^{1/2'} \rightleftharpoons Co_{Co}^{1/2\,\cdot} + Co_{Co}^{3/2'} \tag{6.1}$$

To include the pO2 dependency in oxygen composition there is the reduction reaction. Note that the holes are localized in the cobalt.

$$O_{O1}^{X} + 2Co_{Co}^{1/2\cdot} \rightleftharpoons 2Co_{Co}^{1/2'} + \frac{1}{2}O_{2,(g)} + V_{O1}^{\cdot\cdot} \tag{6.2}$$

Given how difficult it is to extract oxygen from the second site, only the site O1 is included in the reduction. To account for the second site and extend the oxygen stoichiometry past [O] = 5, an inter-site oxygen vacancy reaction is drawn:

$$O_{O2}^{X} + V_{O1}^{\cdot\cdot} \rightleftharpoons O_{O1}^{X} + V_{O2}^{\cdot\cdot} \tag{6.3}$$

With these three reactions, 4 balances must be included: Cobalt site, O1 site, O2 site, Electroneutrality and an extra one to include the nonstoichiometry measure δ. The full list of equations that describe the structure is shown in table 6.2:

Table 6.2.: Defect model for double perovskites.

| Defect structure | |
|---|---|
| $K_1 = \frac{pO_2^{1/2}\left[V_{O1}^{\cdot\cdot}\right]\left[Co_{Co}^{1/2'}\right]^2}{\left[O_{O1}^{X}\right]\left[Co_{Co}^{1/2\cdot}\right]^2} = K_1^0 exp\left(-\frac{\Delta H_1^0}{RT}\right)$ | Reduction |
| $K_2 = \frac{\left[Co_{Co}^{3/2'}\right]\left[Co_{Co}^{1/2\cdot}\right]}{\left[Co_{Co}^{1/2'}\right]^2} = K_2^0 exp\left(-\frac{\Delta H_2^0}{RT}\right)$ | Cobalt disproportionation |
| $K_3 = \frac{\left[O_{O1}^{X}\right]\left[V_{O2}^{\cdot\cdot}\right]}{\left[O_{O2}^{X}\right]\left[V_{O1}^{\cdot\cdot}\right]} = K_3^0 exp\left(-\frac{\Delta H_3^0}{RT}\right)$ | Oxygen site interaction |
| $\left[Co_{Co}^{1/2'}\right] + \left[Co_{Co}^{3/2'}\right] + \left[Co_{Co}^{1/2\cdot}\right] = 2$ | Cobalt site balance |
| $\left[O_{O1}^{X}\right] + \left[V_{O1}^{\cdot\cdot}\right] = 1$ | O1 site balance |
| $\left[O_{O2}^{X}\right] + \left[V_{O2}^{\cdot\cdot}\right] = 5$ | O2 site balance |
| $\left[V_{O1}^{\cdot\cdot}\right] + \left[V_{O2}^{\cdot\cdot}\right] = \delta$ | Non-stoichiometry |
| $\frac{1}{2}\left[Co_{Co}^{1/2\cdot}\right] + 2\delta = \frac{3}{2}\left[Co_{Co}^{3/2'}\right] + \frac{1}{2}\left[Co_{Co}^{1/2'}\right]$ | Electroneutrality |

The oxygen sites balances are fixed to 1 and 5 for alternating layers of $[BaCo_2O_5]-[GdO]$. The non-stoichiometry measure δ is introduced for convenience as the sum of all the oxygen vacancies. The cobalt site balance and the electroneutrality condition follow naturally.

The complexity of the model makes it difficult to solve for δ, pO2 comes out naturally from the equations. The solution is as follows.

$$pO_2 = \left( -\frac{\left[Co_{Co}^{1/2\cdot}\right]^2 K_1 \left[O_{O1}^X\right]}{\left[Co_{Co}^{1/2'}\right]\left([O_{O1}^X] - 1\right)} \right)^2 \tag{6.4}$$

With:

$$\left[Co_{Co}^{1/2\,\cdot}\right] = \frac{-1 + 2\delta + 12K_1 - 8\delta K_1 - \sqrt{1 - 4\delta + 4\delta^2 + 12K_1 + 16\delta K_1 - 16\delta^2 K_1}}{2(4K_1 - 1)} \tag{6.5}$$

$$\left[Co_{Co}^{1/2'}\right] = \frac{-4 + \sqrt{16 - 4(-3 - 4\delta + 4\delta^2)(4K_1 - 1)}}{2(4K_1 - 1)} \tag{6.6}$$

$$\left[O_{O1}^X\right] = \frac{1 - \delta - 7K_3 + \delta K_3 + \sqrt{(-1 + \delta + 7K_3 - \delta K_3)^2 - 4(1 - K_3)(-6K_3 + \delta K_3)}}{2(1 - K_3)} \tag{6.7}$$

The solutions depend on the three equilibrium constants, and δ. In reality, the inputs to the system are temperature (implicit in the equilibrium constants) and $pO_2$, so it has to be fitted as an implicit function (see Appendix I).

GBCO and PBCO can be successfully described with this defect structure. BGLC 10-8-2 is modeled as well. For further compositions of BGLC, an extra defect has to be introduced to the electroneutrality expression, Lanthanum in Barium sites.

$$[\dot{La_{Ba}}] + \frac{1}{2}\left[Co_{Co}^{1/2\,\cdot}\right] + 2\delta = \frac{3}{2}\left[Co_{Co}^{3/2'}\right] + \frac{1}{2}\left[Co_{Co}^{1/2'}\right] \tag{6.8}$$

When $[\dot{La_{Ba}}] = 0$ the previous model is returned. This extension can be used as long as the dopant concentration doesn't alter the layered perovskite structure. The final addition for a general defect model is the inclusion of protonic defects. If the protonation

mechanism is due to hydration then reaction 2.4 applies and the equilibrium expression is:

$$K_4 = \frac{[OH_O^{\cdot}]^2}{pH_2O\,[O_O^X]\,[V_O^{\cdot\cdot}]} \tag{6.9}$$

With the introduction of the protonic defects, the electroneutrality condition becomes:

$$[OH_O^{\cdot}] + [La_{Ba}^{\cdot}] + \frac{1}{2}\left[Co_{Co}^{1/2\,\cdot}\right] + 2\delta = \frac{3}{2}\left[Co_{Co}^{3/2'}\right] + \frac{1}{2}\left[Co_{Co}^{1/2'}\right] \tag{6.10}$$

Note that the oxygen site definition for the hydration reaction has been omitted. O2 has been used as a notation to envelop the oxygen around both cobalt and barium. This is an useful apporximation to calculate the defect concentrations for dry conditions, but it is too simplistic for hydration. All compositions of BGLC, GBCO and PBCO have significant oxygen vacancies around the lanthanide. Yet only BGLC hydrates to any significant degree. Furthermore, hydration sharply drops for lanthanum doping over 20%, pointing towards a more complex set of defects. The proton concentration in the materials shown in figure 6.2 does not mirror total oxygen concentrations but mirror the vacancy concentrations around the cobalt. The most basic, and fuller in terms of oxygen, layer in the structure is $Ba-O$. If these are the oxygen sites that predominantly protonate, then it follows that the adjacent oxygen vacancies are the most prone to being hydrated. Then the proton concentration would result from the stoichiometry in the $Co-O_{4-x}$ layer, leaving the more stable oxygen vacancies untouched in the lanthanide layer.

The data obtained for BGLC 7-8-5 and 5-8-7, plus the hydration data from Strandbakke et al. can be modeled with these principles. The terms in equation 6.9 are defined as follows:

$$\left[O_O^X\right] = \left[O_{O3}^X\right] - \frac{1}{2}\,[OH_O^{\cdot}] \tag{6.11}$$

$$[V_O^{\cdot\cdot}] = [V_{O2}^{\cdot\cdot}] - \frac{1}{2}\,[OH_O^{\cdot}] \tag{6.12}$$

The results are shown in figure 6.2. Once again, here O3 refers to the oxygen in the barium layer and O2 to the oxygen in the cobalt layer. This is treated in a such a way where the oxygen/oxygen-vacancies in the gadolinium layer do not participate in hydration to a significant degree.

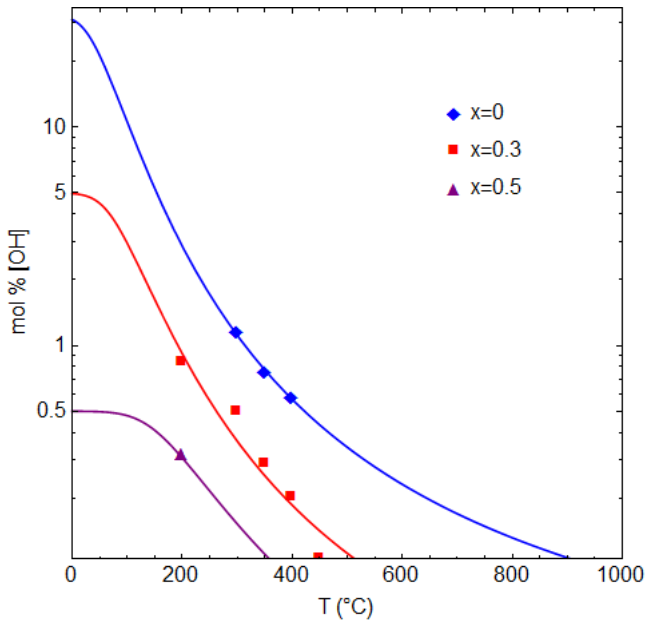


Figure 6.2.: Hydration of 2 compositions of BGLC fitted with the defect model discussed.

Both curves result in almost identical fitting parameters for $\triangle S_{hydr}$ (-121 and -128 J/molK) and $\triangle H_{hydra}$ (-44 kJ/K and -44 kJ/molK) respectively for BGLC 10-8-2 and 7-8-5. More data is needed to confirm these values for the entropy and enthalpy of hydration, but the agreement so far strengthens the idea of discrete oxygen sites with different basicity enabling hydration of the material. The fitting was performed with constant values for oxygen occupancy in the cobalt layer in the whole temperature range; thus it is under the assumption that the change in total oxygen stoichiometry is mostly due to oxygen in the lanthanide layer being exchanged, which was shown to be the more mobile species. The curve for 5-8-7 was made by fixing the entropy and enthalpy of hydration to -120 J/K and -44.0 kJ/K respectively since there was only one data point available.

With this defect model the rest of the defect concentrations can then be calculated. A large range of data is necessary to obtain all the the thermodynamic coefficients involved. The features relating to equation 6.3 occur at low oxygen pressures and high

temperatures. On the other hand, hydration is unlikely to occur at these conditions. For the sake of obtaining practical solutions, one of the 2 regimes can be excluded from the modelling of the respective effects.

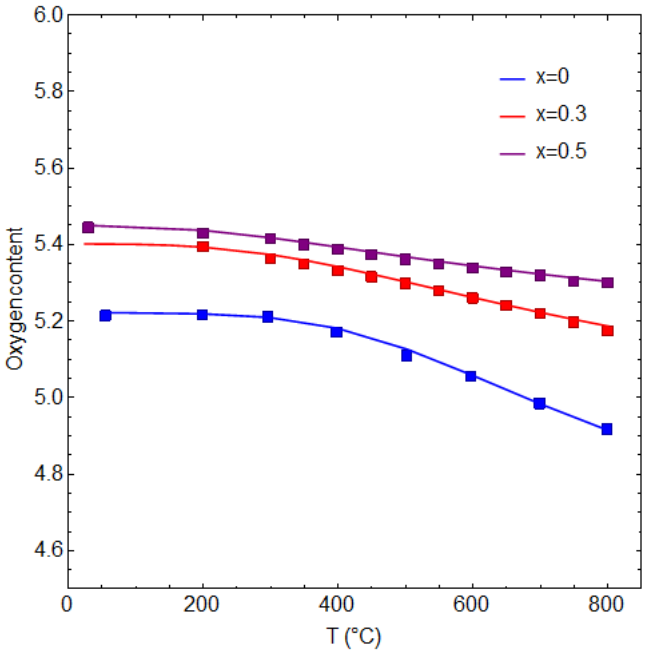


Figure 6.3.: Oxygen stoichiometry for different compositions of BGLC. The starting value for BGLC 5-8-7 is chosen as an educated guess as no data is available.

The oxygen stoichiometry for BGLC 5-8-7, 7-8-5 and 10-8-2 is shown in figure 6.3. Note that the room temperature value for BGLC 5-8-7 is an educated guess, only data for 10-8-5 and 7-8-5 is available. It can be seen that the more Lanthanum that is added, the smaller the range of non-stoichiometry and the lower the amount of vacancies (as described by the electroneutrality condition). The fitting parameters are shown in table 6.3. Note that the values of these enthalpies and pre-exponential factors may change with a wider range of data and isothermal measurements, particularly those for BGLC 5-8-7 as stoichiometry starting point was set arbitrarily. This set of parameters correctly describes the current measurements, but there is likely more than one combination of parameters that fit this range of temperatures and pressure. In the case of BGLC 5-8-7 It serves as a proof-of-concept for the model.

Table 6.3.: Defect model fitting parameters.

| | $K_1$ | | $K_2$ | | $K_3$ | |
|---|---|---|---|---|---|---|
| | ${K_1}^0$ | $\triangle H_1\ (kJ/mol)$ | ${K_2}^0$ | $\triangle H_2\ (kJ/mol)$ | ${K_3}^0$ | $\triangle H_3\ (kJ/mol)$ |
| 10-8-2 | 0.16 | 290 | 18 | -290 | 8.1 | 44 |
| 7-8-5 | 0.20 | -0.42 | 8.8 | 0.36 | 1.9 | 27 |
| 5-8-7 | 2.1 | 0.18 | 0.91 | -0.38 | 0.81 | 19 |

A number of features come out of the model that follow the observations on the double perovskites. The thermodynamic parameter for $K_3$ may create a two-fold reduction that leads to a different behavior before, and after, the first oxygen site is completely vacant. An increase in the concentration of holes (localized in $Co^{4+}$) with temperature leads to a peak in conductivity for p-type materials. Conductivity measurements showing this behavior were performed in a paralel study and are pending publication.

In figure 6.4 the changing defect concentrations can be seen for $Ba_{0.7}Gd_{0.8}La_{0.5}Co_2O_{6-\delta}$ at different conditions. At low $pO_2$ the dominant valence of cobalt is 2+ during the entire temperature range. Meanwhile, there are always more vacancies in O1 than there are in O2, although the values are closer at high temperatures and low pressures.

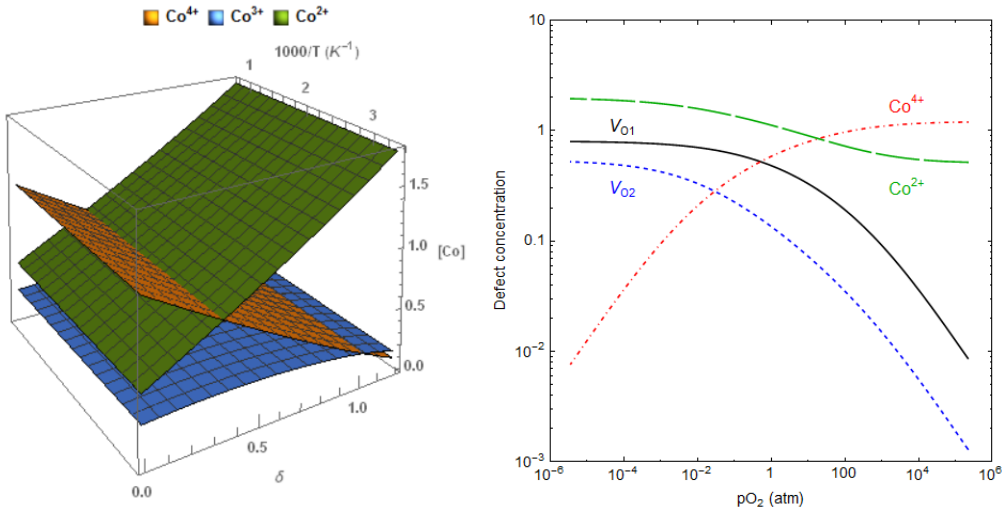


Figure 6.4.: Left: Cobalt valence concentrations at all combinations of δ and temperature for 30% $La$ doped BGLC. Right: Brouwer diagram of 30% $La$ doped BGLC 7-8-5 at 500 °C showing the concentrations of the two types of oxygen vacancies and $Co^{4+}$.

## 6.3. Measuring the diffusion process

One of the main subjects of this work is the measurement of the diffusion process and the calculation of the coefficients and their implications. The first step towards understanding the thread followed in this section is the complexity of the material at hand. BGLC exhibits an almost unprecedented ease for ionic diffusion amongst related perovskites. On top of this, the electronic conductivity is above 1000 $S/cm$ for most of the examined temperatures, again, a significant property in such an oxide. The high electronic conductivity masks most pO2 dependencies on the total conductivity. For perovskites as cathode materials in SOFC's, the ionic conductivity must generally be above 0.01 $S/cm$ at operating conditions. If BGLC reaches this threshold, the transport number for the ionic conductivity would still be in the order of $10^{-5}$. Thus, fluctuations in the signal measured to determine the total conductivity could very well extend past pressure dependencies in the ionic conductivity. This makes it difficult to examine ionic conductivity, and oxygen diffusion, by the commonly used conductivity relaxation technique. Similar to transient TG measurements, conductivity relaxation works by introducing a step change in $pO_2$ and analyzing the relaxation curve of the conductivity; a curve the cannot be clearly see.

To get around these limitations 3 techniques (SIMS, GPA, TGA) were used. Perhaps the more standard of the three, SIMS offers precise measurements of tracer diffusion and surface exchange for certain conditions. The technique has been utilized in depth and the appropriate solutions to Fick's laws are detailed in literature. As described in previous sections, proper use of SIMS imposes a few requirements. First and foremost the samples must be dense, as close to 100% of the theoretical density as possible. The results from the synthesis routes outlined in sections 5.1 show that this isn't always a straightforward process. Nevertheless dense samples were achieved and the measurements were performed resulting in figure 5.30.

Past the density, there is the issue of the exchange process. After the sample is annealed in the GPA reaction chamber, the $^{18}O$ gas is flushed in. The depth profile of the heavy isotope cannot exceed certain dimensions. Deep profiles past about 10-20 $\mu m$ cannot be analyzed to the same precision due to interference from the "walls" in the well created. For BGLC this poses a challenge. It can be seen from Strandbakke et al.[44] that significant stoichiometry changes in the material don't occur below 300 $^{\circ}$C. At this temperature the exchange time to get a complete profile was ~10 minutes.

With increasing temperature the time required to recreate the depth profile decreases exponentially and quickly approaches 0, figure 6.5. The operation of numerous valves at the time of vacuuming the gas and flushing in the new mix adds a level of uncertainty to quick experiments. All in all, this makes SIMS measurements, at least in this form, unsuitable for high temperatures with fast kinetics.

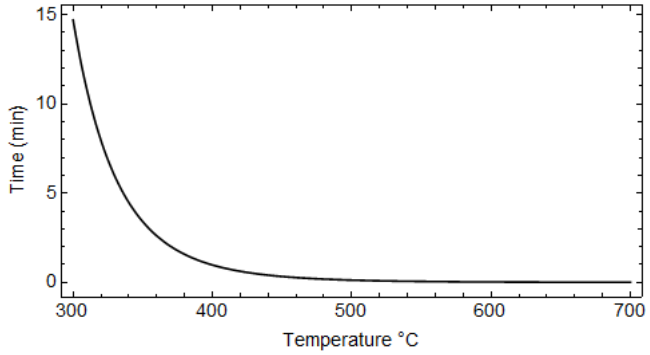


Figure 6.5.: Example isotope exchange timescales for SIMS measurements in BGLC.

At the other of the line are transient TG experiments. TGA relies on similar pellets as SIMS. Density has to be maximized in order to ensure that diffusion doesn't occur through the pores, but through the material itself. Other than that, the experiment is well characterized and little input from the operator is needed as the measurement is done in-situ. The lag time when flushing the gas through the TG chamber was discussed in section 5.3. This resulted in thicker samples and an exclusion of high temperatures (above 700 $^\circ C$) from the measurements. Such a problem can be fixed with a smaller TG apparatus and higher flow from the gas mixers. Still, it is not the high temperatures that are a concern, but the intermediate range. TGA requires that equilibrium is reached in dense pellets of considerable size after the $pO_2$ step change. Around 700 $^\circ C$ the relaxation curve is resolved in a matter of hours. As $D_{chem}$ decreases exponentially with temperature, so does the time to reach equilibrium increase. Temperatures below 500 $^\circ C$ put experiments in larger time scales needing several days to equilibrate. While entirely possible, experiments like these are inconvenient when 3 ramps have to be performed for each measurement: temperature anneal, reduction step, and oxidation step. See figure 6.6.

To tackle the intermediate temperature range a somewhat unconventional technique is employed. The GPA setup offers in-situ measurements with a different geometry. Powders are used instead of pellets, circumventing the high density constraints. The

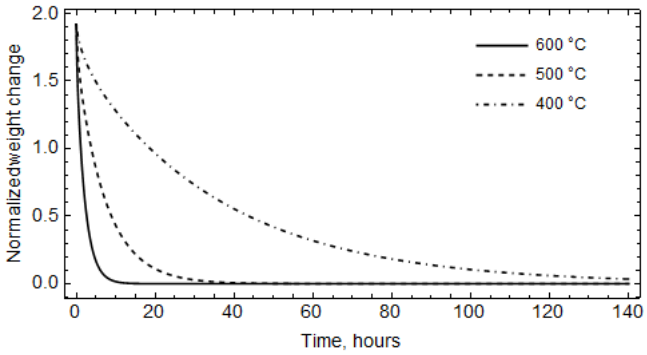


Figure 6.6.: Sample timescales of transient TG experiments for BGLC at sample temperatures.

reduced diffusion lengths in the powder accelerate the process and open the door for lower temperature when compared to TGA. Since the diffusion profiles for GPA are taken versus time and up to equilibrium, the upper boundary of SIMS measurements does not apply. But much like every technique explored here, GPA has upper and lower boundaries were the accuracy is compromised, or the timescales become prohibiting.

The lowest measurable temperature for BGLC 10-8-2 (300 $^{\circ}C$) is accessible through GPA. Yet SIMS is preferred as a reference point when possible. As expected, the time to reach equilibrium decreases exponentially with temperature (described by the models in section 2.5.3) and quick measurements are possible. It was discussed in the results section that starting at 450 $^{\circ}C$ the relaxation curves start to show interference from an initial delay in the exchange rate. This establishes the upper limit for the GPA diffusion measurements in an attempt to maintain the integrity of the data.

Equation 2.49 is the solution of Fick's law that governs GPA experiments. One of the input parameters is the particle radius. While the geometry of dense pellets used in TGA is easy to accurately characterize, powders are less straightforward. SEM images were used to quantify the radius of the particles taken as spheres. Special care has to be taken here as the values for the coefficients extracted are highly sensitive to the radius used. On this point, mathematical considerations described in section 2.5.2 explain how the equation falls apart for fine powders ($r < 1\mu m$).

In this manner, simultaneous use of these three techniques is needed to elucidate transport properties for materials such as BGLC. The full temperature range of interest for SOFCs can be successfully explored even with high kinetics; it is particularly useful when

conductivity relaxation experiments are not possible due to the relatively high electronic conductivity.

## 6.4. The diffusion coefficient

The source of the measurement and the nature of the experiment can have an impact on the calculated parameters, and may lead to different physical quantities. A number of coefficients appear throughout previous sections, self, tracer, and chemical diffusion. With the results from each experiment at hand, the source and nature of each coefficient have to be considered to reconcile the differences.

SIMS and GPA experiments were done with an oxygen isotope exchange to introduce a tracer for tracking the diffusion process. Both of these output $D^*$, the tracer diffusivity, and are directly comparable. The mass changes in TGA of course come from a change in the chemical potential by changing the $pO_2$. This yields $D_{chem}$, the chemical diffusivity. The effect of the chemical potential gradient can be accounted for by the thermodynamic factor $\gamma$ with equation 6.13, giving the self-diffusion coefficient $\tilde{D}$:[47]

$$\frac{\tilde{D}}{D_{chem}} = \gamma \tag{6.13}$$

$$\gamma = \frac{1}{2}\frac{\partial \ln pO_2}{\partial \ln c_0} \tag{6.14}$$

Where $c_0$ is the total concentration of oxygen in the material. Examples of the thermodynamic factor calculated from TGA at 3 different temperatures are given in table 6.4.

Table 6.4.: Thermodynamic factor of BGLC 10-8-2 at different temperatures.

| Temperature (ºC) | $pO_2$low (bar) | $pO_2$high (bar) | $\gamma$ |
|---|---|---|---|
| 500 | 0.01 | 0.2 | 116 |
| 600 | 0.01 | 0.2 | 135 |
| 650 | 0.01 | 0.2 | 135 |

Maier et. al. studied the relation between the different quantities and came to the conclusion that self-diffusion and tracer-diffusion are related by the difference in activity of the two isotopes, $^{16}O$ vs $^{18}O$. Expressed by:[48]

$$\frac{\tilde{D}}{D^*} = \frac{\partial \ln a_0}{\partial \ln c_0} \tag{6.15}$$

If the activity between the isotopes is taken as constant, the coefficients measured can be directly compared. Figure 6.7 compiles results from the three techniques showing the self (or tracer) diffusion coefficient across the entire temperature range. A good agreement across 400 $^\circ$C through 4 orders of magnitude for the diffusivity is observed. This suggests that the different coefficients can indeed be compared in this way, and emphasizing the usefulness of the techniques for such a wide range of values.

Table 6.5.: Fitting parameters for the oxygen self-diffusion coefficient in BGLC 10-8-2 across different techniques.

| | SIMS+GPA | GPA | TGA | SIMS+GPA+TGA |
|---|---|---|---|---|
| $E_a$(eV) | 0.68 | 0.74 | 0.71 | 0.72 |
| $D_0(cm^2/s)$ | $4.28 * 10^{-5}$ | $1.19 * 10^{-4}$ | $6.65 * 10^{-4}$ | $1.28 * 10^{-4}$ |

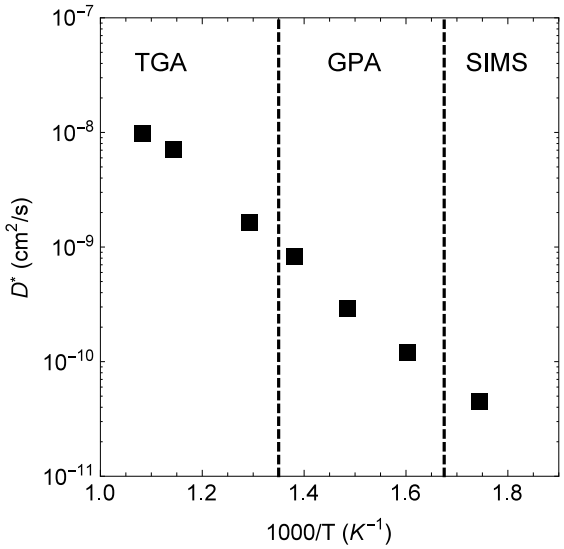


Figure 6.7.: Self-/tracer-oxygen diffusion coefficient in BGLC 10-8-2 across different temperatures from different techniques.

## 6.5. The surface coefficient

Previously, it was discussed how the TG experiments were done solely for the measurement of the diffusion coefficient. This section will address more details on the results from GPA and SIMS. Figure 6.8 shows the surface coefficients measured from these techniques at different temperatures. Just as with diffusion, the linear trend indicates coherence between the techniques. The activation energy and pre-exponential factor obtained from the combined data is very similar to the GPA-only parameters.

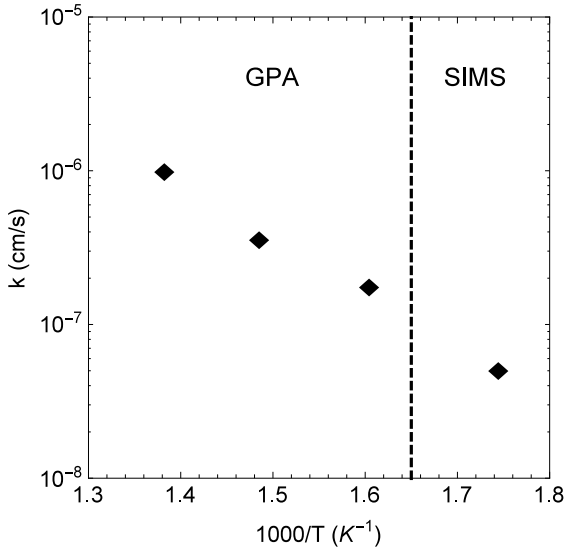


Figure 6.8.: Surface coefficient, $k$, in BGLC 10-8-2 across different temperatures from different techniques.

Table 6.6.: Fitting parameters for the surface coefficient of BGLC 10-8-2 across different techniques.

| | GPA | GPA + SIMS |
|---|---|---|
| $E_a(eV)$ | 0.66 | 0.69 |
| $k_0(cm/s)$ | $4.08 * 10^{-2}$ | $5.98 * 10^{-2}$ |

For the GPA coefficients, the values were extracted from equation 2.25 in the tracer diffusion experiments. To be able to include the rates calculated from homomolecular exchange a number of measurements and mathematical manipulations must be performed. Bouwmeester et. al. proposed a mathematical relation by setting the exchange rate ($R$) equal to the flux of oxygen though the sample surface ($j_{ex}$).[49] See equation 6.16 below:

$$R = j_e x = \frac{1}{4} k_s c_O \tag{6.16}$$

Where $k_s$ is the surface coefficient and $c_0$ is the concentration of oxygen in the material ($mol/cm^3$). Hancke et. al. explored this relationship with $H_2/D_2$ exchange in lanthanum tungsates with mixed results. Certain materials deviated from the predicted values.[50] To apply this to BGLC values for the oxygen concentration are needed. Strandbakke et. al. reported the oxygen stoichiometry across the whole temperature range at a $pO_2$ of 0.2 bar. With these values, and the thermodynamic factor, $c_O$ can be calculated. It should be noted that the values for the exchange rate reported throughout this thesis are expressed as $RS$. That is the exchange rate, $R$, multiplied the specific surface area, $S$, in $cm^2/g$. To obtain an accurate of value of $S$, and subsequently $R$, surface area measurements must be performed. BET is suggested as a technique for this purpose. However, to obtain an estimate for these parameters and test the validity of equation 6.16, SEM micrographs can be used.

By fitting the particles as spheres and calculating the resulting surface area (see figure 5.16) $S$, and $R$, can be calculated. These can in turn be compared to the $R$ values obtained from homomolecular GPA experiments. Figure 6.9 shows the comparison between the measured rates from the GPA homomolecular exchange ($R$), and the calculated rates from $k_s$ ($R_k$).

The approximate nature of this comparison makes it difficult to draw quantitative conclusions from the absolute values. Direct measurement of surface area is needed for more definitive statements. Still, it can be seen that in order-of-magnitude the techniques show somewhat similar results. Thus suggesting that equation 6.16 may indeed describe the relation between the rate and the coefficient, and that the exchange rate may be thought of as the flux through the sample's surface in a manner analogous to oxygen membranes.

## 6.6. The surface reaction

In order to probe the mechanism of the surface reaction between the sample and oxygen past the calculation of the exchange rate, we look to heteromolecular gas exchange. In

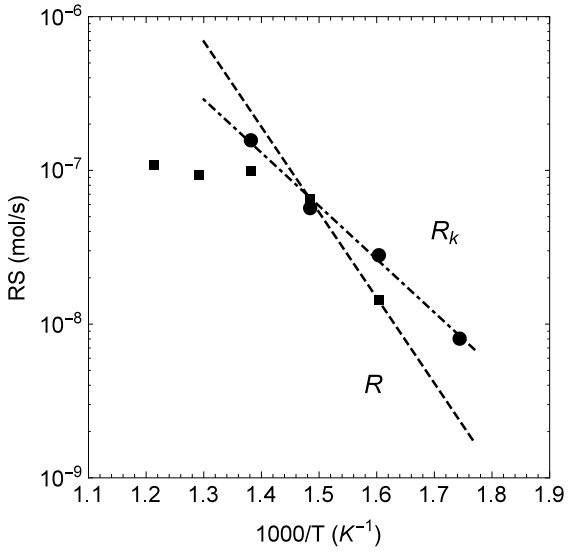


Figure 6.9.: Comparison of surface exchange rates measured directly by GPA ($R$) and calculated from the TGA coefficients ($R_k$).

section 2.3.5 the possible reactions for oxygen exchange are outlined. Generally speaking, they are categorized by the source of the desorbing oxygen molecules. When no oxygen atoms from the sample are involved the reaction is deemed homomolecular. In reality, 1 or 2 atoms from the solid state are expected to take part in the exchange. In this case, gas-to-surface exchange is more complex. To recall the possible reactions from section 2.3.5:

Only oxygen from the gas is exchanged.

$$^{18}O_{2,(g)} + ^{16}O_{2,(g)} \rightleftharpoons 2\,^{18}O^{16}O_{(g)} \tag{6.17}$$

1 oxygen atom from the solid is exchanged.

$$^{18}O_{2,(g)} + ^{16}O^{X}_{O,(s)} \rightleftharpoons {}^{18}O^{16}O_{(g)} + ^{18}O^{X}_{O,(s)} \tag{6.18}$$

$$^{16}O_{2,(g)} + ^{18}O^{X}_{O,(s)} \rightleftharpoons {}^{18}O^{16}O_{(g)} + ^{16}O^{X}_{O,(s)} \tag{6.19}$$

2 oxygen atoms from the solid are exchanged.

$$^{18}O_{2,(g)} + 2^{16}O^{X}_{O,(s)} \rightleftharpoons^{16} O_{2,(g)} + 2^{18}O^{X}_{O,(s)} \tag{6.20}$$

As the isotopic ratio in the gas phase changes with time, the concentration profiles do not follow the exponential behavior described by equation 2.25. In this situation, the overall process consists of two steps: the gas exchange (adsorption-dissociation-recombination-desorption) and the diffusion (chemical- or self-) inside the sample. Amongst these, the case with chemical-diffusion is easiest to examine.

The exchange rates extracted from the experiments with chemical-diffusion (but not tracer-) are the same as the purely homomolecular exchange. Thus suggesting that the surface reaction proceeds unchanged regardless of a net flow of oxygen atoms into, or out of, the sample. If the processes are indeed separate steps, then the model for heteromolecular exchange introduced in section 2.3.4 applies.

Onto the case where net tracer-diffusion exists. If surface exchange is the much faster process, the isotopic concentration in the surface mirrors that of the gas. This means that the gas phase concentration depends on the ability of the material to diffuse oxygen. On the other hand, if diffusion is faster, the concentration at the surface mirrors the concentration in the sample's bulk. And the gas phase concentration profiles are dictated by the exchange process.

In either case, the behavior may be modelled by equations 2.26 to 2.28 from the heteromolecular exchange model.

**CASE 1**

For the first case, where the surface mirrors the gas concentration, the probability of forming a certain molecule will arise from the isotopic composition of the gas phase.

$$P^{32,g} = \left(\frac{n^g_{16}}{n^g_{16} + n^g_{18}}\right)^2 \quad P^{36,g} = \left(\frac{n^g_{18}}{n^g_{16} + n^g_{18}}\right)^2 \quad P^{34,g} = \frac{2n^g_{16}n^g_{18}}{\left(n^g_{16} + n^g_{18}\right)^2} \tag{6.21}$$

The superscript $g$ denotes the gas phase.

To test the model, a sample of BGLC 10-8-2 was annealed at 350 ° C in regular oxygen to the equilibrium stoichiometry. Following equilibrium, the gas was vacuumed out and the reaction was filled to the same pressure (100 $mbar$) with $^{18}O$. The relaxation curves are then recorded. See figure 6.10.

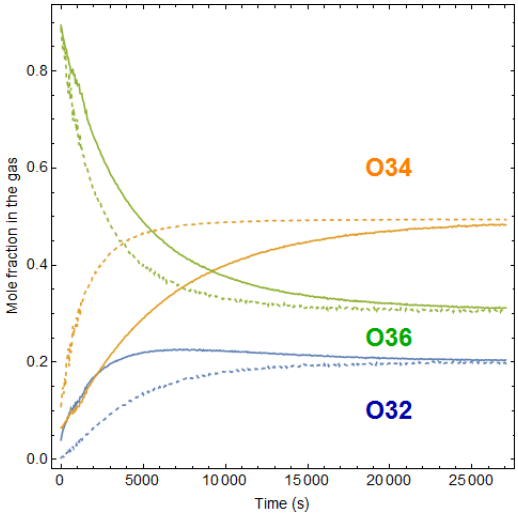


Figure 6.10.: Oxygen gas species concentration profile for a heterogenous GPA experiment on BGLC 10-8-2. Green, orange and blue are $O_2^{36}$, $O_2^{34}$ and $O_2^{32}$ respectively. The solid lines is the data. The dashed lines are the instantaneous equilibrium points as modeled by case 1.

The dashed lines are the time-dependent equilibrium mole fractions of each gas, calculated from the instantaneous probability of forming said gas with the isotope concentrations present in the gas phase. The solid lines are the actual gas concentrations measured by the MS.

At first glance, he concentration profiles of $O_2^{36}$ and $O_2^{34}$ proceed as expected. With gas concentrations changing towards the time-dependent equilibrium values and finally reaching it. On the other hand, $O_2^{32}$ behaves differently. The $O_2^{32}$ molecule rises away from the time-dependent equilibrium initially, before finally decreasing back to the expected levels. This behavior clashes with the expected profiles and cannot be modelled with the proposed equations. Gas concentrations must always change towards the statistical probability of formation.

The deviation in $O_2^{32}$ may arise due to the lack of equilibrium between the surface and the gas phase. Given that the sample is initially rich in $O^{16}$ it seems that the desorbed molecules mirror the sample itself, and not the gas.

**CASE 2**

For the second case, where the surface mirrors the sample's concentration, the probability of forming a certain molecule will arise from the isotopic composition of the sample.

$$P^{32,s} = \left(\frac{n_{16}^s}{n_{16}^s + n_{18}^s}\right)^2 \quad P^{36,s} = \left(\frac{n_{18}^s}{n_{16}^s + n_{18}^s}\right)^2 \quad P^{34,s} = \frac{2n_{16}^s n_{18}^s}{(n_{16}^s + n_{18}^s)^2} \tag{6.22}$$

The superscript $s$ denotes the solid phase.

The same data from the previous case is now modelled to these equations.

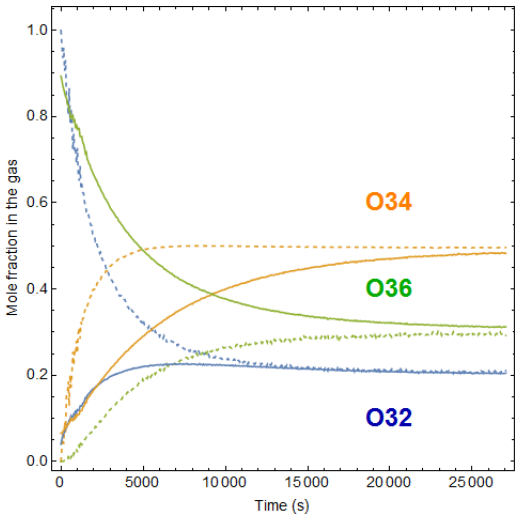


Figure 6.11.: Oxygen gas species concentration profile for a heterogenous GPA experiment on BGLC 10-8-2. Green, orange and blue are $O_2^{36}$, $O_2^{34}$ and $O_2^{32}$ respectively. The solid lines is the data. The dashed lines are the instantaneous equilibrium points as modeled by case 2.

Again, the dashed lines are the time-dependent equilibrium mole fractions of each gas, calculated from the instantaneous probability of forming said gas with the isotope concentrations present in the sample. The solid lines are the actual gas concentrations measured by the MS.

The gas phase isotope composition measured by the MS were shown previously in figure 5.14. These profiles are then used to calculate the isotope fractions inside the sample. The figure above (6.11) shows the result.

This time, all the gas molecules adhere to the expected profiles. The rise in $O_2^{32}$ that caused a discrepancy in the first model is now accounted for, the gas concentration always moves towards the statistical equilibrium (maximum) value. $O_2^{36}$ and $O_2^{34}$ follow similar profiles and reach equilibrium as expected. To move past qualitative results, the profiles were fitted to equation 2.26. Where again, the equilibrium concentrations were obtained from the instantaneous probabilities just shown.

The three fitted profiles for the oxygen molecules are shown in figure 6.12.

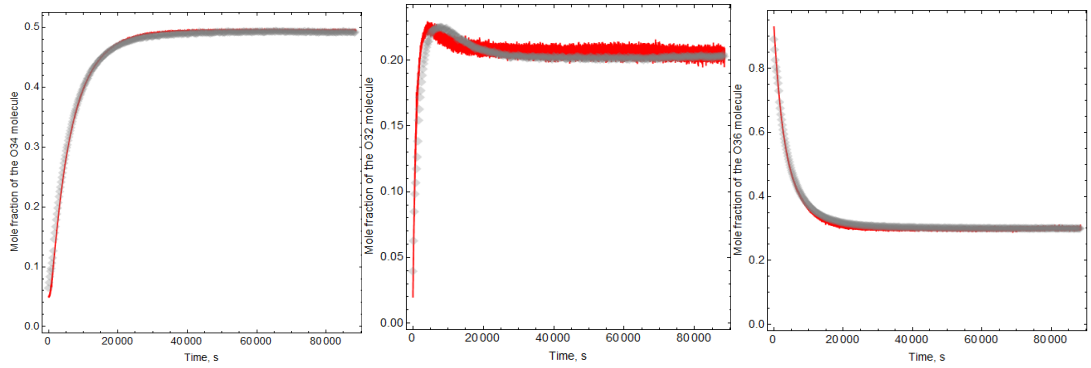


Figure 6.12.: Case 2 model fitted to the gas concentration profiles from a GPA experiment. Left: $O_2^{34}$, center: $O_2^{32}$ and left:$O_2^{36}$.

The red line is the fitted model, the gray diamonds is the measured data. This model closely describes the data, but it works under a limiting assumption: that the measured isotopic profiles are those of the surface. For this to be true, the diffusion through the sample must be significantly faster than the surface exchange. It can only be applied for short diffusion paths (fine powders). In the general case, the surface composition will be somewhere between the gas composition and the bulk.

When heteromolecular exchange can be described with this model, the surface reaction must be equation 6.20. The cases when both atoms come from the sample. The fitted rates (RS) of $1*10^{-4}$, $1.3*10^{-4}$, $1.5*10^{-4}$ for $O_2^{34}$, $O_2^{32}$ and $O_2^{36}$ respectively are also in reasonable agreement with the measured rate of homomolecular exchange in standard experiments ($6.5*10^{-5}$). Suggesting the notion that even in the absence of a net tracer-diffusion gradient, in principle it may be the same process. Furthermore, given that the bulk and the surface are at quasi-equilibrium, the rate limiting step for the exchange process is confirmed to be adsorption/desorption (and not oxidation/reduction). Equation 2.19 then describes the rate dependences but one change must be made. It has been

established in the defect structure that electron holes are localized in cobalt ions so the overall equilibrium rate expression becomes:

$$R_0 = \sqrt{r^+_{ads} r^-_{ads}} = \sqrt{\frac{k_{1,ads} k_{-1,ads}}{K_{ox}}} pO_2^{1/2} \left[ Co_{Co}^{1/2\,\cdot} \right]^2 \left[ O_O^X \right] [V_O^{\cdot\,\cdot}]^{-1} \tag{6.23}$$

The pressure dependence for the rate was found to be around 0.82 and 0.86 for 2 different temperatures from figure 5.11. If the defect concentrations were constant, then the $pO_2$ dependence would equal 0.5, as we have seen, they are not constant. The concentration of all the defects in equation 6.23 is pressure dependent.

Then the question is on the ratio of the $pO_2$ dependences of the squared cobalt term and the oxygen vacancy. The concentration of cobalt 4+ will increase with pressure. Oxygen vacancies on the other hand will be filled at high $pO_2$ an inverse relation to some exponential term.

$$R_0 \propto pO_2^n \tag{6.24}$$

where

$$n = 0.5 + 2x - y + z \tag{6.25}$$

$$\left[ Co_{Co}^{1/2\,\cdot} \right] \propto pO_2^x \tag{6.26}$$

$$[V_O^{\cdot\,\cdot}] \propto pO_2^y \tag{6.27}$$

$$\left[ O_O^X \right] \propto pO_2^z \tag{6.28}$$

$x$ and $z$ are positive and $y$ is negative. Then the total $pO_2$ dependence must be higher than 0.5 for all temperatures as all terms are possitive. The calculation can be made from the defect model using the fitting parameters in table 6.3 for BGLC 10-8-2 at the

measurement temperatures. For $T = 400$ ºC the pressure dependences for the $pO_2$ range examined are:

$$\left[Co_{Co}^{1/2\,\cdot}\right] \propto pO_2^{0.11} \tag{6.29}$$

$$[V_O^{\cdot\,\cdot}] \propto pO_2^{-0.091} \tag{6.30}$$

$$\left[O_O^X\right] \propto pO_2^{0.014} \tag{6.31}$$

Which leads to a total $pO_2$ dependece for the rate of:

$$R_0 \propto pO_2^{0.5+2*0.11-(-0.091)+0.014} = pO_2^{0.82} \tag{6.32}$$

For $T = 450$ ºC, $n = 0.86$. Both of these values are in complete agreement with the measured pressure dependence. Equation 6.23 and the defect structure proposed in section 6.2 correctly model the oxygen surface exchange rate. The full derivation of these equations and values are given in appendix B. This confirms the hypothesis that the adsorption/desoprtion step is rate limiting in this case.

## 6.7. BGLC and state-of-the-art materials

From section 3.2, reviews show us that BGLC's diffusion and surface coefficients, measured by any of the techniques here, are larger in magnitude than most material's in the field (figures 3.4 and 3.5). Furthermore, the activation energies reported in tables 6.5 and 6.6 are lower than most as well. It has been established in literature that layered double perovskites, as is the case here, show faster ionic transport than regular perovskites. Recent work on double perovskites with similar transport coefficients as BGLC has focused on the optimization of these parameters, and the viability of their use in SOFCs.

In figure 6.13 the diffusion and surface coefficients of BGLC are shown against common perovskites. As it has been discussed, the coefficients are characterized by equations

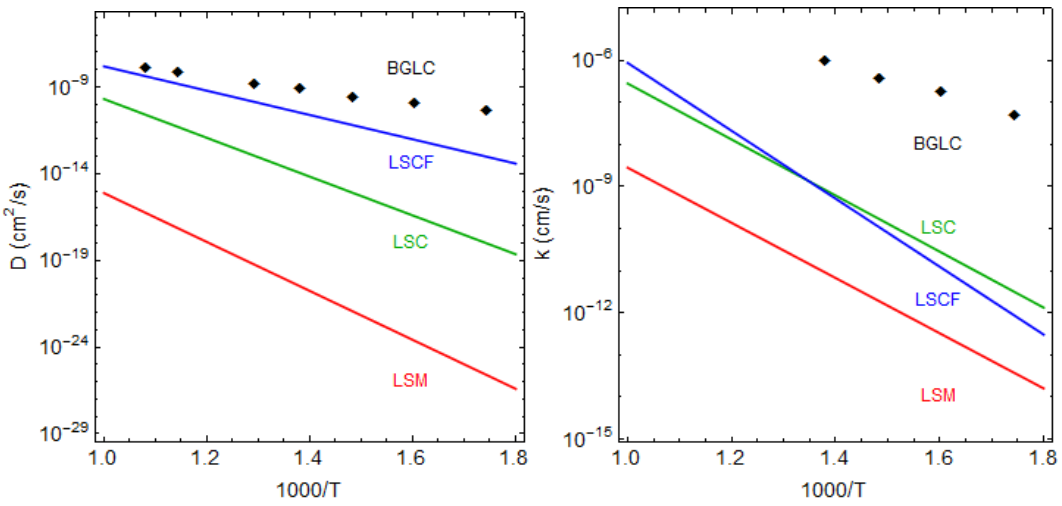


Figure 6.13.: On the left, the Arrhenius plot of the diffusion coefficient of common perovskites and BGLC. On the right, the Arrhenius plot of surface coefficients for the same materials. The BGLC data is from this work, the solid lines for LSM, LSC and LSCF are taken from references [51], [47], and [52] respectively.

2.36 and 5.2. Thus, the pre-exponential values ($D_0$ and $k_0$) and the activation energies are of utmost interest here. It can be seen that BGLC has significantly lower activation energies, and higher pre-exponential factors, than this selection of disordered perovskites. These improvements in potential are mostly attributed to the A-site cation ordering discussed in section 3.2; as well as the oxygen vacancy association in the lanthanide layer. The high vacancy concentration (at least half of an oxygen site is vacant in the perfect structure) around the lanthanide plane creates a channel with reduced energy barriers for oxygen transport.

Amongst other promising layered perovskites, BGLC performs at least on par with GBCO and has slightly lower coefficients than PBCO. The sheer magnitude of $D$ and $k$ are not the only benchmark for their potential as electrodes in terms of ionic conduction. The objective is lowering the operating temperature to the intermediate range (<700 $^\circ$C). To this end, a number of metrics exist to evaluate the potential of MIECs as cathode materials. Traditionally, in terms of ionic transport, the cutoff for optimal operation of FCs has been set at an ionic conductivity in the order 0.01 S/cm. More recently, Maier et. al. have discussed a ratio of the surface kinetics to the ionic conductivity as the better measure of the expansion of the electrochemical active zone (past the TPB).[53] In this case, a small ratio of $k/D$ yields larger reaction areas. Adler et. al. discusses how high

values of the product of the coefficients, $k * D$, are required for lower resistances.[54] Figure 6.14 shows the criteria values for BGLC versus similar double perovskites as compiled by Tarancon et. al.[55]

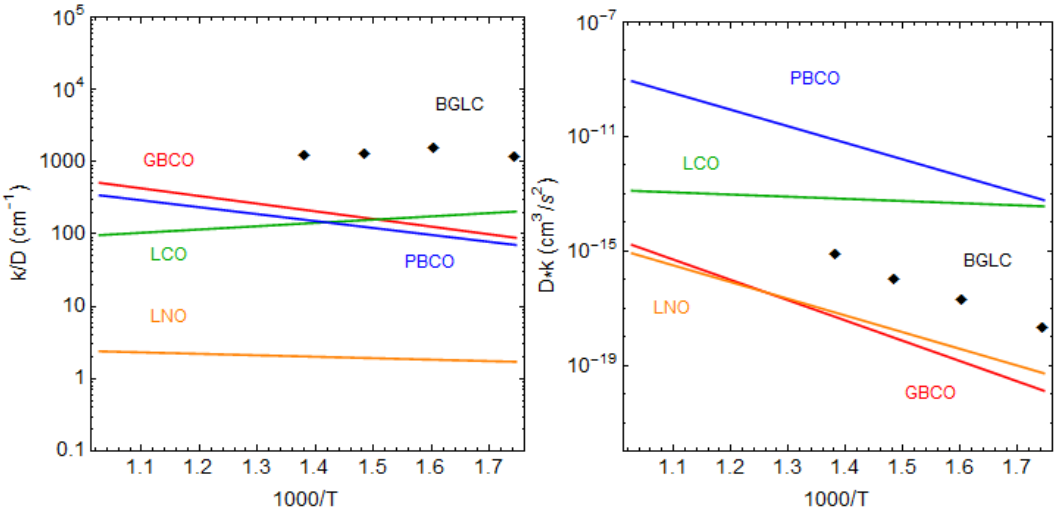


Figure 6.14.: On the left, the surface to diffusion coefficient ratio of common layered perovskites and BGLC. On the right, the product of the transport coefficients for the same materials. The BGLC data is from this work, the solid lines for GBCO, PBCO, LCO and LNO are taken from references [55], [37] and [56] respectively.

For the product factor, values around $10^{-14} cm^3/s^2$ are desired. BGLC reaches this limit around 500 $^\circ$C, faster than LNO or PBCO. For the surface to diffusion ratio, ~$10^3$ $cm^{-1}$ is a commonly mentioned threshold. In this case, BGLC has a higher ratio than the other layered perovskites shown in figure 6.14. Yet it is still sufficiently low. By all metrics regarding ionic transport, BGLC fulfills the criteria. Values for $k/D$, $kD$ or $\sigma_O$ are at least competitive with state-of-the-art layered perovskites, and better than most disordered perovskites.

## 6.8. Protonation experiments

The performance of an electrode material for SOFCs or steam electrolyzers is closely related to its hydration properties. TGA is the main technique used to measure the total hydration of these oxides. Mass changes in the presence of wet gas can give information on the equilibrium amounts of water incorporated into the material. The hydration

of BGLC 10-8-2 was previously characterized by Strandbakke et. al. and shown to be significantly higher than similar perovskites. In an ongoing effort to characterize the family of BGLC compositions, hydration curves were obtained for BGLC 7-8-5 and 5-8-7.

Results such as the ones shown here, or in literature, give only part of the story. Maier et. al. have recently proposed alternative reactions for protonation in oxides. Section 2.2.3 describes the two mechanisms, hydration vs hydrogenation. In a setup like the one used for TGA experiments the only measured quantity is mass change. The resulting concentration of $[OH]_O^\bullet$ depends on which reaction is taken as the dominant one. If the material undergoes hydrogenation, then the concentration of protons from a given mass change will be about 10 times higher than if it undergoes hydration. GPA was employed to experimentally determine the extent of these reactions and complement the TGA results.

The experiments were ultimately insufficient to determine the protonation mechanism. The introduction of water to the GPA reaction chamber presented a series of issues that muddled the accuracy of the results. The gas switches are done as fast as possible in an effort to minimize changes to the sample stoichiometry. When water is introduced, an extra step has to be taken, increasing the time at which the sample is exposed to a different $pO_2$. Furthermore, water diffuses more slowly than the rest of the gases. This causes a gradual increase (instead of a step change) in the water signal as it reaches the leak valve to the MS. Coupled with the delay in pressure increase due to heating the fresh gas, the initial water pressure changes become somewhat inaccurate. What can be dubbed "stabilization period" for the water signal becomes a problem as the protonation kinetics are extremely fast. This makes it hard to deconvolute the data and obtain a clear picture of BGLC's protonation.

While the water is incorporated into BGLC, the total pressure in the reaction chamber decreases. Increasing the relative intensity of the other signals in the MS and affecting the internal pressure of the MS (which affects the total current). Coupled with the "stabilization period", this makes proper resolution of fast experiments difficult. Accurate measurements would require protonation curves in slower timescales. Further work in refining the setup is needed.

## 6.9. Further work

The work on BGLC is ongoing and far from complete. For the sake of completeness, extra measurements of low temperature TGA, high temperature GPA, and intermidiate temperature SIMS can be done to show the actual overlap in the data. More importantly though, is the full characterization of the dopant effects on the defect structure of BGLC. Isobaric and isothermal TG experiments are needed for more values of $x$ (the dopant concentration).

Finally, the most work to be done with regards to this thesis are further protonation experiments as it will further elucidate the potential of the material. Isobaric TG runs with the wet $O_2/Ar$ mix are necessary for more compositions of BGLC. And, as was mentioned, much more work is required on the GPA setup to discern between protonation mechanisms and attribute the correct proton concentration values to the data from TGA.

# 7. Conclusions

From the experimental results and analysis it can be concluded that BGLC forms a tetragonal p4/mmm crystal with a doubled c-axis. The materials are ordered in layers of $[CoO_2]-[BaO]-[CoO_2]-[GdO_\delta]$ where the oxygen sites in each of these layers exhibit different behavior. For practical purposes oxygen in the material can be discretized as three effective oxygen sites $O1$, $O2$ and $O3$, around $Gd$, $Co$ and $Ba$ respectively. The oxygen vacancies gather around $Gd$ and diffuse through this layer preferntially. Oxygen vacancies are introduced to the $O2$ layer by $La$ doping on $Gd$. This allows for hydration of the material, measured up to 1.4 mol % of protons at 350 ºC. On the other hand, $La$ doping on the $Ba$ sites greatly reduces the vacancies in $O2$, and thus the protonation is sharply reduced. The total amount of vacancies and the variation of oxygen content with temperature is also reduced with increasing $La$ content. For all values of $x$ $O3$ is fully occupied at the conditions studied.

The defect model was written to follow the structural characterization closely. The reference state for the material was chosen to be $Ba_{1-x}Gd_{0.8}La_{0.2+x}Co_2(O1)O_5$, an oxygen filled cell with a separate oxygen site around $Gd$. The model was solved and proved succesful at describing the experimental data. To fit the hydration data, the oxygen sites around $Ba$ and $Co$ had to be considered seprately, as it is the cobalt-oxygen vacancies that are hydrated. This defect structure goes beyond BGLC, it is able to model layered double perovskites of the general form $Ba_{1-x}Ln_{1+x}Co_2O_{6-\delta}$.

Similar to materials such as GBCO and PBCO, BGLC shows outstanding oxygen transport properties. The diffusion and surface coefficients exceed $10^{-9}cm^2/s$ and $10^{-7}cm/s$ respectively at temperatures as low as 350 $^oC$. By any metric employed, BGLC's ability to dissociate and transport oxygen places it amongst the very best in literature. High ionic conductivity ($>0.01S/cm$) at intermediate temperatures should expand the active interphase in a SOFC with a BGLC cathode. As it has been discussed, the high oxygen diffusivity is attributed to the accumulation of oxygen vacancies in a single layer, providing fast diffusion channels through the lattice. Although it was not initially considered,

the combination of high $k$ and $D$ values makes BGLC a candidate material for oxygen permeation membranes.

Isotope exchange experiments by Gas Phase Analysis were succesfully employed to measure transport coefficients and exchange rates. The results were consistent across experimental techniques. This highlights the importance of the technique as a convenient way of characterizing materials and elucidating exchange processes. Oxygen kinetics and exchange mechanisms are explored satisfactorily. The adsorption/desorption step was identified as the rate limiting step of the oxygen exchange process; still, protonation mechanisms remain unknown. In situ measurement of $D$ and $k$ at low temperatures can be performed quickly and accurately.

# Bibliography

[1] Chonghea Li, Xionggang Lu, Weizhong Ding, Liming Feng, Yonghui Gao, and Ziming Guo. Formability of abx3 (x= f, cl, br, i) halide perovskites. *Acta Crystallographica Section B: Structural Science*, 64(6):702–707, 2008.

[2] Helen D Megaw. Crystal structure of double oxides of the perovskite type. *Proceedings of the Physical Society*, 58(2):133, 1946.

[3] VM Goldschmidt. Construction of crystals. *Zeitschrift für Technische Physik*, 8:251–264, 1927.

[4] Harlan U Anderson. Review of p-type doped perovskite materials for sofc and other applications. *Solid State Ionics*, 52(1):33–41, 1992.

[5] Luís G Tejuca and JLG Fierro. *Properties and applications of perovskite-type oxides*. CRC Press, 2000.

[6] Mark T Anderson, Kevin B Greenwood, Gregg A Taylor, and Kenneth R Poeppelmeier. B-cation arrangements in double perovskites. *Progress in solid state chemistry*, 22(3):197–233, 1993.

[7] Truls Norby. Solid-state protonic conductors: principles, properties, progress and prospects. *Solid State Ionics*, 125(1):1–11, 1999.

[8] Truls Norby. A kr öger-vink compatible notation for defects in inherently defective sublattices. *Journal of the Korean Ceramic Society*, 47(1):19–25, 2010.

[9] Daniel Poetzsch, Rotraut Merkle, and Joachim Maier. Proton conductivity in mixed-conducting bsfz perovskite from thermogravimetric relaxation. *Physical Chemistry Chemical Physics*, 16(31):16446–16453, 2014.

[10] Joachim Maier. *Physical chemistry of ionic materials: ions and electrons in solids.* John Wiley & Sons, 2004.

[11] Torbjfirn N Akermark, Gunnar B Hultquist, and L Grasjö. Probabilities for oxygen exchange in o2 in contact with a solid surface. *Journal of trace and microprobe techniques*, 14(2):377–388, 1996.

[12] Erik Hörnlund. Studies of dissociation of diatomic molecules with isotope spectroscopy. *Applied surface science*, 199(1):195–210, 2002.

[13] H He, HX Dai, and CT Au. Defective structure, oxygen mobility, oxygen storage capacity, and redox properties of re-based (re= ce, pr) solid solutions. *Catalysis today*, 90(3):245–254, 2004.

[14] M Che and AJ Tench. Characterization and reactivity of molecular oxygen species. *Advances in catalysis*, 32:1, 1983.

[15] Joseph Cunningham, Edward L Goold, and Jose LG Fierro. Reactions involving electron transfer at semiconductor surfaces. part 11.-oxygen isotope exchange via photoinitiated r 1, r 0 and place exchange processes on zno and tio 2. *Journal of the Chemical Society, Faraday Transactions 1: Physical Chemistry in Condensed Phases*, 78(3):785–801, 1982.

[16] Takamasa Ishigaki, Shigeru Yamauchi, Kohji Kishio, Junichiro Mizusaki, and Kazuo Fueki. Diffusion of oxide ion vacancies in perovskite-type oxides. *Journal of Solid State Chemistry*, 73(1):179–187, 1988.

[17] K Compaan and Y Haven. Correlation factors for diffusion in solids. part 2.-indirect interstitial mechanism. *Transactions of the Faraday Society*, 54:1498–1508, 1958.

[18] John Crank. *The mathematics of diffusion.* Oxford university press, 1979.

[19] B Serin and RT Ellickson. Determination of diffusion coefficients. *The Journal of Chemical Physics*, 9(10):742–747, 1941.

[20] Jens Bragdo Smith. *Mixed oxygen ion/electron conductors for oxygen separation processes: Surface kinetics and cation diffusion.* Unipub AS, 2005.

[21] HS Edwards, AF Rosenberg, and JT Bittel. Thorium oxide-diffusion of oxygen, compatibility with borides, and feasibility of coating borides by pyrohydrolysis of metal halides. Technical report, DTIC Document, 1963.

[22] Zuoan Li. Numerical evaluations of transcendental equations for transient experiments. *international journal of hydrogen energy*, 37(9):8118–8122, 2012.

[23] Roger A De Souza, Martha J Pietrowski, Umberto Anselmi-Tamburini, Sangtae Kim, Zuhair A Munir, and Manfred Martin. Oxygen diffusion in nanocrystalline yttria-stabilized zirconia: the effect of grain boundaries. *Physical Chemistry Chemical Physics*, 10(15):2067–2072, 2008.

[24] San Ping Jiang. Development of lanthanum strontium manganite perovskite cathode materials of solid oxide fuel cells: a review. *Journal of Materials Science*, 43(21):6799–6833, 2008.

[25] Jörg Richter, Peter Holtappels, Thomas Graule, Tetsuro Nakamura, and Ludwig J. Gauckler. Materials design for perovskite sofc cathodes. *Monatshefte für Chemie - Chemical Monthly*, 140(9):985–999, 2009.

[26] Stephen J Skinner. Recent advances in perovskite-type materials for solid oxide fuel cell cathodes. *International Journal of Inorganic Materials*, 3(2):113–121, 2001.

[27] San Ping Jiang. Development of lanthanum strontium manganite perovskite cathode materials of solid oxide fuel cells: a review. *Journal of Materials Science*, 43(21):6799–6833, 2008.

[28] Junichiro Mizusaki, Yuki Yonemura, Hiroyuki Kamata, Kouji Ohyama, Naoya Mori, Hiroshi Takai, Hiroaki Tagawa, Masayuki Dokiya, Kazunori Naraya, Tadashi Sasamoto, et al. Electronic conductivity, seebeck coefficient, defect and electronic structure of nonstoichiometric la 1- x sr x mno 3. *Solid state ionics*, 132(3):167–180, 2000.

[29] G Ch Kostogloudis, N Vasilakos, and Ch Ftikos. Preparation and characterization of pr 1-x sr x mno 3$\pm\delta$ (x= 0, 0.15, 0.3, 0.4, 0.5) as a potential sofc cathode material operating at intermediate temperatures (500–700Â° c). *Journal of the European Ceramic Society*, 17(12):1513–1521, 1997.

[30] G Ch Kostogloudis and Ch Ftikos. Characterization of nd 1-x sr x mno 3$\pm\delta$ sofc cathode materials. *Journal of the European Ceramic Society*, 19(4):497–505, 1999.

[31] Hee Sung Yoon, Seung Woo Choi, Dokyol Lee, and Byong Ho Kim. Synthesis and characterization of gd 1- x sr x mno 3 cathode for solid oxide fuel cells. *Journal of power sources*, 93(1):1–7, 2001.

[32] MB Phillipps, NM Sammes, and O Yamamoto. Gd 1- x a x co 1- y mn y o 3 (a= sr, ca) as a cathode for the sofc. *Solid State Ionics*, 123(1):131–138, 1999.

[33] S Kuharuangrong, T Dechakupt, and P Aungkavattana. Effects of co and fe addition on the properties of lanthanum strontium manganite. *Materials Letters*, 58(12):1964–1970, 2004.

[34] AA Taskin, AN Lavrov, and Yoichi Ando. Fast oxygen diffusion in a-site ordered perovskites. *Progress in Solid State Chemistry*, 35(2):481–490, 2007.

[35] AA Taskin, AN Lavrov, and Yoichi Ando. Achieving fast oxygen diffusion in perovskites by cation ordering. *arXiv preprint cond-mat/0501127*, 2005.

[36] A. Maignan, C. Martin, D. Pelloquin, N. Nguyen, and B. Raveau. Structural and magnetic studies of ordered oxygen-deficient perovskites lnbaco2o5+d, closely related to the 112 structure. *Journal of Solid State Chemistry*, 142(2):247 – 260, 1999.

[37] G. Kim, S. Wang, A. J. Jacobson, L. Reimus, P. Brodersen, and C. A. Mims. Rapid oxygen ion diffusion and surface exchange kinetics in prbaco2o5+x with a perovskite related structure and ordered a cations. *J. Mater. Chem.*, 17:2500–2505, 2007.

[38] Monica Burriel, Juan Pena-Martinez, Richard J. Chater, Sarah Fearn, Andrey V. Berenov, Stephen J. Skinner, and John A. Kilner. Anisotropic oxygen ion diffusion in layered prbaco2o5+ÎŽ. *Chemistry of Materials*, 24(3):613–621, 2012.

[39] Nobuo Ishizawa, Toru Asaka, Tatsunari Kudo, Koichiro Fukuda, Akira Yasuhara, Nobuyuki Abe, and Taka hisa Arima. Structural evolution of gdbaco2o5+ÎŽ (ÎŽ = 7/18) at elevated temperatures. *Chemistry of Materials*, 26(22):6503–6517, 2014.

[40] A Tarancón, D Marrero-López, J Peña-Martínez, JC Ruiz-Morales, and P Núñez. Effect of phase transition on high-temperature electrical properties of gdbaco 2 o 5+ x layered perovskite. *Solid State Ionics*, 179(17):611–618, 2008.

[41] DS Tsvetkov, VV Sereda, and A Yu Zuev. Oxygen nonstoichiometry and defect structure of the double perovskite gdbaco 2 o 6- $\delta$. *Solid State Ionics*, 180(40):1620–1625, 2010.

[42] DS Tsvetkov, IL Ivanov, DA Malyshkin, and A Yu Zuev. Oxygen content, cobalt oxide exsolution and defect structure of the double perovskite prbaco 2 o 6- $\delta$. *Journal of Materials Chemistry A*, 2016.

[43] David Ávila-Brande, Graham King, Esteban Urones-Garrote, Anna Llobet, and Susana García-Martín. Structural determination and imaging of charge ordering and oxygen vacancies of the multifunctional oxides rebamn2o6-$\chi$ (re= gd, tb). *Advanced Functional Materials*, 24(17):2510–2517, 2014.

[44] Ragnar Strandbakke, Vladimir A. Cherepanov, Andrey Yu. Zuev, Dmitry S. Tsvetkov, Christos Argirusis, Georgia Sourkouni, Stephan PrÃŒnte, and Truls Norby. Gd- and pr-based double perovskite cobaltites as oxygen electrodes for proton ceramic fuel cells and electrolyser cells. *Solid State Ionics*, 278:120 – 132, 2015.

[45] Edith Bucher, Andreas Egger, Peter Ried, Werner Sitte, and Peter Holtappels. Oxygen nonstoichiometry and exchange kinetics of ba 0.5 sr 0.5 co 0.8 fe 0.2 o 3- $\delta$. *Solid State Ionics*, 179(21):1032–1035, 2008.

[46] RA De Souza, JA Kilner, and JF Walker. A sims study of oxygen tracer diffusion and surface exchange in la 0.8 sr 0.2 mno 3+ $\delta$. *Materials Letters*, 43(1):43–52, 2000.

[47] Fabrice Mauvy, Jean-Marc Bassat, Emmanuelle Boehm, Patrice Dordor, Jean-Claude Grenier, and JP Loup. Chemical oxygen diffusion coefficient measurement by conductivity relaxation-correlation between tracer diffusion coefficient and chemical diffusion coefficient. *Journal of the European Ceramic Society*, 24(6):1265–1269, 2004.

[48] Joachim Maier. On the correlation of macroscopic and microscopic rate constants in solid state chemistry. *Solid State Ionics*, 112(3):197–228, 1998.

[49] Henny JM Bouwmeester and Anthonie J Burggraaf. Dense ceramic membranes for oxygen separation. *The CRC handbook of solid state electrochemistry*, page 481, 1997.

[50] Ragnhild Hancke, Zuoan Li, and Reidar Haugsrud. Hydrogen surface exchange on proton conducting oxides studied by gas phase analysis with mass spectrometry. *Journal of Membrane Science*, 439:68–77, 2013.

[51] Anthonie Jan Burggraaf and Louis Cot. *Fundamentals of inorganic membrane science and technology*, volume 4. Elsevier, 1996.

[52] JA Lane, SJ Benson, D Waller, and JA Kilner. Oxygen transport in la 0.6 sr 0.4 co 0.2 fe 0.8 o 3- $\delta$. *Solid State Ionics*, 121(1):201–208, 1999.

[53] J Fleig and J Maier. The polarization of mixed conducting sofc cathodes: Effects of surface reaction coefficient, ionic conductivity and geometry. *Journal of the European Ceramic Society*, 24(6):1343–1347, 2004.

[54] Stuart B Adler, JA Lane, and BCH Steele. Electrode kinetics of porous mixed-conducting oxygen electrodes. *Journal of the Electrochemical Society*, 143(11):3554–3564, 1996.

[55] Tarancon Albert, JS Stephen, JC Richard, F Hernandez-Ramirez, and AK John. Layered perovskites as promising cathodes for intermediate temperature solid oxide fuel cells. *J. Mater. Chem*, 17(30):3175–81, 2007.

[56] Emmanuelle Boehm, J-M Bassat, MC Steil, Patrice Dordor, Fabrice Mauvy, and J-C Grenier. Oxygen transport properties of la 2 ni 1- x cu x o 4+ $\delta$ mixed conducting oxides. *Solid State Sciences*, 5(7):973–981, 2003.

# A. Defect model solution

This appendix details the solution and fitting to the defect model. Table 6.2 is re-inserted here for ease of reading:

| Defect structure | |
|---|---|
| $K_1 = \frac{pO_2^{1/2}[V_{O1}^{\cdot\cdot}]\left[Co_{Co}^{1/2'}\right]^2}{[O_{O1}^X]\left[Co_{Co}^{1/2\cdot}\right]^2} = K_1^0 exp\left(-\frac{\Delta H_1^0}{RT}\right)$ | Reduction |
| $K_2 = \frac{\left[Co_{Co}^{3/2'}\right]\left[Co_{Co}^{1/2\,\cdot}\right]}{\left[Co_{Co}^{1/2'}\right]^2} = K_2^0 exp\left(-\frac{\Delta H_2^0}{RT}\right)$ | Cobalt disproportionation |
| $K_3 = \frac{[O_{O1}^X][V_{O2}^{\cdot\cdot}]}{[O_{O2}^X][V_{O1}^{\cdot\cdot}]} = K_3^0 exp\left(-\frac{\Delta H_2^0}{RT}\right)$ | Oxygen site interaction |
| $\left[Co_{Co}^{1/2'}\right] + \left[Co_{Co}^{3/2'}\right] + \left[Co_{Co}^{1/2\,\cdot}\right] = 2$ | Cobalt site balance |
| $\left[O_{O1}^X\right] + [V_{O1}^{\cdot\cdot}] = 1$ | O1 site balance |
| $\left[O_{O2}^X\right] + [V_{O2}^{\cdot\cdot}] = 5$ | O2 site balance |
| $[V_{O1}^{\cdot\cdot}] + [V_{O2}^{\cdot\cdot}] = \delta$ | Non-stoichiometry |
| $\frac{1}{2}\left[Co_{Co}^{1/2\,\cdot}\right] + 2\delta = \frac{3}{2}\left[Co_{Co}^{3/2'}\right] + \frac{1}{2}\left[Co_{Co}^{1/2'}\right]$ | Electroneutrality |

The objective when solving the defect model is to obtain expressions for the different defect concentrations that depend on the input variables ($pO_2$ and $T$). In this case, the complexity of the set of equations makes it more convenient to solve for $pO_2$ and use $\delta$ as an input instead. The first step is then solve for $pO_2$ in the reduction reaction:

$$pO_2 = \left(\frac{K_1\left[O_{O1}^X\right]\left[Co_{Co}^{1/2\cdot}\right]^2}{[V_{O1}^{\cdot\cdot}]\left[Co_{Co}^{1/2'}\right]^2}\right)^2 \tag{A.1}$$

Since $\delta$ is an input and it depends on the two oxygen vacancy concentrations, it is better to express $[V_{O1}^{\cdot\cdot}]$ in terms of $\left[O_{O1}^X\right]$.

$$pO_2 = \left( -\frac{K_1 \left[O_{O1}^X\right] \left[Co_{Co}^{1/2\cdot}\right]^2}{\left(\left[O_{O1}^X\right] - 1\right) \left[Co_{Co}^{1/2'}\right]^2} \right)^2 \tag{A.2}$$

All the equilibrium constants are functions of temperature only. The challenge lies in obtaining expressions for the three defects in A.2 that depend only on $T$ and $\delta$. The two cobalt species appear only in 3 equations: Cobalt disproportionation, Cobalt site balance, Non-stoichiometry, and Electroneutrality. This system can be solved for and results in:

$$\left[Co_{Co}^{1/2\cdot}\right] = \frac{-1 + 2\delta + 12K_1 - 8\delta K_1 - \sqrt{1 - 4\delta + 4\delta^2 + 12K_1 + 16\delta K_1 - 16\delta^2 K_1}}{2(4K_1 - 1)} \tag{A.3}$$

$$\left[Co_{Co}^{1/2'}\right] = \frac{-4 + \sqrt{16 - 4(-3 - 4\delta + 4\delta^2)(4K_1 - 1)}}{2(4K_1 - 1)} \tag{A.4}$$

The last step is solving for $\left[O_{O1}^X\right]$. Using equations: Oxygen site interactions, O1 site balance, O2 site balance, Non-stoichiometry, Electroneutrality the solution is found.

$$\left[O_{O1}^X\right] = \frac{1 - \delta - 7K_3 + \delta K_3 + \sqrt{(-1 + \delta + 7K_3 - \delta K_3)^2 - 4(1 - K_3)(-6K_3 + \delta K_3)}}{2(1 - K_3)} \tag{A.5}$$

With the last 4 equations presented, plus the expressions for each equilibrium constant from table 6.2, $pO_2$ can be calculated from a temperature ($T$) and oxygen non-stoichiometry ($\delta$) pair. The fitting process for the isobaric data used in this thesis is an iterative process:

1. A set of pre-exponential values and enthalpies are chosen for the 3 equilibrium constants.
2. $pO_2$ is calculated from this constants and the values of $\delta$ used in the data.
3. The calculated $pO_2$ for each $T$ and $\delta$ couple is compared to the experimental values of 0.21.

4. A new set of pre-exponential values and enthalpies are chosen to reduce the error in $pO_2$ values.

5. Once the error goes below the precision chosen, the values for the pre-exponentials and enthalpies of $K_1$, $K_2$ and $K_3$ are obtained.

The presence of dopants or protons will affect the electroneutrality condition as described in section 6.2 but the solution algorithm is the same.

# B. $pO_2$ dependence calculations

In this appendix, the derivation and calculation of the $pO_2$ dependence on $R_0$ is shown. From section 6.6, the equilibrium oxygen exchange rate is:

$$R_0 = \sqrt{r^+_{ads} r^-_{ads}} = \sqrt{\frac{k_{1,ads} k_{-1,ads}}{K_{ox}}} pO_2^{1/2} \left[ Co^{1/2\,\cdot}_{Co} \right]^2 \left[ O^X_O \right] [V_O^{\cdot\,\cdot}]^{-1} \tag{B.1}$$

To obtain the overall $pO_2$ dependence each defect must be examined. If the defects can be described with an exponential relation to pressure, the three equations are:

$$\left[ Co^{1/2\,\cdot}_{Co} \right] = k_{Co} pO_2^x \tag{B.2}$$

$$[V_O^{\cdot\,\cdot}] = k_v pO_2^y \tag{B.3}$$

$$\left[ O^X_O \right] = k_O pO_2^z \tag{B.4}$$

where $k_i$ are the terms encapsulating every $pO_2$-independent quantity. The equilibrium rate equation then becomes:

$$R_0 = \sqrt{r^+_{ads} r^-_{ads}} = \sqrt{\frac{k_{1,ads} k_{-1,ads}}{K_{ox}}} pO_2^{1/2} k_{Co} pO_2^{x^2} k_O pO_2^z k_v pO_2^{y^{-1}} \tag{B.5}$$

and can be expressed as

$$\ln R_0 = \ln\left(\sqrt{\frac{k_{1,ads}k_{-1,ads}}{K_{ox}}}k_{Co}k_O k_v\right) + \frac{1}{2}\ln pO_2 + 2x\ln pO_2 + z\ln pO_2 - y\ln pO_2 \quad \text{(B.6)}$$

$$\ln R_0 = \ln\left(\sqrt{\frac{k_{1,ads}k_{-1,ads}}{K_{ox}}}k_{Co}k_O k_v\right) + (\frac{1}{2} + 2x + z - y)\ln pO_2 \quad \text{(B.7)}$$

$$\ln R_0 = K' + (\frac{1}{2} + 2x + z - y)\ln pO_2 \quad \text{(B.8)}$$

here $K'$ is just a pseudo-constant that envelops all the pressure-independent terms used for convenience. From equation B.8 it can be seen that the slope of a log/log plot of $R_0$ vs $pO_2$ results in the overall pressure dependence expressed by the exponents of the individual defect concentrations as:

$$R_0 \propto pO_2^{\frac{1}{2}+2x+z-y} \quad \text{(B.9)}$$

The values for $x$,$y$, and $z$ can be obtained from the defect model by plotting each defect concentration vs $pO_2$ and solving for the slopes. The results are tabulated below.

Table B.1.: Calculated $pO_2$ dependence of the defect concentrations.

| | Temperature (ºC) | |
|---|---|---|
| Parameter | 400 | 450 |
| x | 0.11 | 0.12 |
| y | -0.091 | -0.10 |
| z | 0.014 | 0.016 |